ISSN 0914−9244
CODEN JSTEEW

Journal of Photopolymer Science and Technology

Volume 36 Number 1

2023

JOURNAL OF PHOTOPOLYMER SCIENCE AND TECHNOLOGY
Home Page https://www.spst-photopolymer.org
https://www.jstage.jst.go.jp/browse/photopolymer

Journal of Photopolymer Science and Technology publishes papers on the scientific progress and the technical development of photopolymers.

Editorial Board

International Advisory Board

The Editorial Office
Assoc. Prof. Hiroyuki MAYAMA
Department of Chemistry, Asahikawa Medical University, 2-1-1-1 Midorigaoka-Higashi, Asahikawa, Hokkaido 078-8510, Japan.
FAX: +81-166-68-2782, e-mail: mayama@asahikawa-med.ac.jp

Information for Contributors

Submit Manuscripts to the SPST Homepage (Journal --> Submission of Papers --> Editorial Manager). Submission is a representation that the manuscript has not been published previously elsewhere. The manuscript should be accompanied by a statement transferring copyright from the authors (or their employers-whoever holds the copyright) to the Society of Photopolymer Science and Technology. A suitable form for copyright transfer is available from the SPST Homepage. This written transfer of copyright, which previously was assumed to be implicit in the act of submitting a manuscript, is necessary under the Japan copyright law. Further information may be obtained from the "Manual for Manuscript Writing" at the SPST Homepage.

Proofs and All Correspondence: Concerning papers in the process of publication should be addressed to the Editorial Office.

Manuscript Preparation: All the papers submitted are reproduced electronically as they were. For this reason, the manuscripts should be prepared according to the Manual for Manuscript Writings shown at the SPST Homepage.

Subscription Price (Airmail Postage included):
¥12,000 (in Japan), US$ 150.00 (for Foreign)

Subscriptions, renewals, and address changes should be addressed to the Editorial Office. For the address changes, please send both old and new addresses and, if possible, include a mailing label from the wrapper of recent issue. Requests from subscribers for missing journal issues will be honored without charge only if received within six months of the issue's actual date of publication; otherwise, the issue may be purchased at the single-copy price.

Publication Charge (Reprint Order): To support a part of the cost of publication of journal pages, the author's institution is requested to pay a page charge of ¥3,000 per page (with a one-page minimum) and an article charge of ¥12,000 per article. The page charge (if honored) entitles the author to 50 free reprints. For Errata the minimum page charge is ¥3,000, with no articles charge and no free reprints.

The cover designed by M. Tsuda and M. Morishita

JOURNAL OF PHOTOPOLYMER SCIENCE AND TECHNOLOGY

Volume 36 Number 1

2023

Published by

THE SOCIETY OF PHOTOPOLYMER SCIENCE AND TECHNOLOGY

Editorial

Journal of Photopolymer Science and Technology (JPST), which has been published by The Society of Photopolymer Science and Technology (SPST), celebrated its 30th anniversary in 2017. The editors would like to express their sincere thanks to all authors as well as the readers for warm and sustained supports for this long term of the publication of this Journal.

Advances in technologies of 'the Internet of things' (IoT) and 'information technology' (IT) are due to major advances in semiconductor technology, enabling semiconductor integration by advanced lithographic technologies. The advancement of lithography has been supported by the resist material processing technology, which improves the electronic performance of semiconductor devices such as high speed, low power consumption, integration of ultra large scaled circuits, and reduction of manufacturing cost.

The International Conference of Photopolymer Science and Technology (ICPST) organized by SPST for these 40 years has played an important role as a forum for the discussion and information exchange on the resist material process technology used in various lithographic technologies such as g-line, i-line, KrF, ArF, electron beam, and X-ray. ArF immersion lithography has been used for 22-nm-generation semiconductor manufacturing technology. From 2019 EUV lithography started to use for high volume manufacturing of 7 nm+ node logic devices. The IRDS 2022 roadmap reported that high NA EUV lithography will be used for the mass production of logic semiconductor devices around 2025 or 2026. Furthermore, nanoimprint lithography, and DSA technology are still promising candidates for semiconductor nano-fabrication technologies for the advanced semiconductor devices.

For supporting the future IoT technology, the advanced techniques of the lithography are required increasingly, where material technologies such as photo-functional groups, photo-acid generators, and photo-curable resins, etc. are the driving force for the progress of semiconductor technology with quantum scale and quantum effect. Basic research on photopolymer is more significant in developing new technologies such as quantum device technology with lower power consumption and lower manufacturing cost by combining with life science and quantum device technology.

All the science and technology related to photopolymer must be focused for further progress of ICPST. New Symposia will continue to be provided in place of conventional ones. The international symposium of Organic and Hybrid Materials for Photovoltaic and Optoelectronic Devices was added in 2017. In addition, the international symposium of Fundamentals and Applications of Biomimetics Materials and Processes was added in 2018. And in 2021, the plenary session is added to introduce the promising and significant technology in the future related on photopolymer science and technology. In this year, Dr. Tetsuya Wadaki, Senior Analyst, Industry Research Dept., Investment Research Division, Mitsubishi UFJ Morgan Stanley Securities will present on the plenary talk of **“Semiconductor Industry Exceeds $1 Trillion as Third Super Cycle Arrives”**.

Constructive opinions from researchers and scientists are welcomed for future progress of ICPST.

Editors

The Photopolymer Science and Technology Award

1. The Photopolymer Science and Technology Award is established to prepare the distinguished contributions of scientists who have made significant achievements in photopolymer science and technology.

2. The achievement must meet the following requirements, of which (A) is essential.
   (A) be excellent original work which greatly contributes to the progress and improvement of photopolymer science and technology
   (B) be creative work suggesting the future evolutions in photopolymer science and technology
   (C) be reviewed or invited papers which contain enlightening and educative contents, and are essential to photopolymer scientists and engineers

3. Receiving this award is subject to the author(s) having been established in "Journal of Photopolymer Science and Technology" in principle.

4. The commendation will be given for up to three works annually.

5. The award ceremony will be held as a part of the International Conference of Photopolymer Science and Technology organized by the Society of Photopolymer Science and Technology.

6. A testimonial sheet will be presented to each of the prize winners. A testimonial plate and a medal are given to commend an achievement.

7. Commendation is authorized in the names of the Representatives of the Society of Photopolymer Science and Technology (SPST), Journal of Photopolymer Science and Technology (JPST), and the International Conference of Photopolymer Science and Technology (ICPST).

8. The Commended works will be chosen on the recommendation of the organizing Committee Members of the International Conference of Photopolymer Science and Technology.

9. The General Meeting of the Society of Photopolymer Science and Technology will select up to three works for this award annually.

10. President of the Society of Photopolymer Science and Technology will immediately inform all the prize winners of the year and makes the names public in Journal of Photopolymer Science and Technology.

11. These rules may be revised through the approval of the General Meeting of the Society of Photopolymer Science and Technology.

Additional clause: The above rules are valid from July 1, 1996.
Revised on April 26, 2002.
Revised on December 3, 2012.

Journal of Photopolymer Science and Technology
Volume 36, Number 1 (2023) 3 − 4 ©2023SPST

The Photopolymer Science and Technology Award

The Photopolymer Science and Technology Award No. 212100, the Best Paper Award 2021, was presented to Tomotaka Tsuchimura (FUJIFILM Corporation) for his outstanding contribution published in Journal of Photopolymer Science and Technology, **33**, (2020) 15–26, entitled “Recent Progress in Photo-Acid Generators for Advanced Photopolymer Materials”.

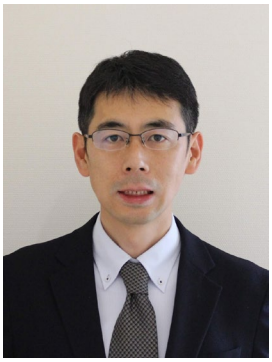

Tomotaka Tsuchimura

Tomotaka Tsuchimura is a Research Manager of Synthetic Organic Chemistry Laboratories at FUJIFILM Corporation. He received M.S. degree in Synthetic Organic Chemistry from Tokyo Institute of Technology in 2000 under the supervision of Prof. Takeshi Nakai and Prof. Katsuhiko Tomooka. In addition, he received Ph. D. in Synthetic Organic Chemistry from Nara Institute of Science and Technology (NAIST) in 2019 under the supervision of Prof. Kiyomi Kakiuchi. Since he joined FUJIFILM in 2000 and has developed photopolymer materials for graphic printing plates (CTP), UV inks, color filters (LCD, image sensor) and photoresists (KrF, ArF, EB, EUV lithography). He has applied over 250 patents in these fields. He has received the Photopolymer Science and Technology Award, the Best Paper Award 2008. His research interests are the development of new photopolymer materials and their applications.

Photopolymer materials have been widely used in industries owing to their practicability, low-cost, and ecological advantage [1,2]. One of the key components of these photopolymer materials is photo-acid generators (PAGs) [3-7]. The photopolymer materials using PAGs enables reactions to strictly control in view of time, space compared to materials using a thermal process. PAGs are recognized as an important tool in materials science and micro-/nanoelectronics. Various PAGs have been developed corresponding to many industrial demands such as photoresists, stereo-lithography, coatings, inks, and adhesives. However, in recent years, PAGs with more sophisticated and diverse functions are required in order to respond to the emergence of various exposure light sources (*e.g.* light-emitting diodes (LEDs)), novel applications such as computer-to-plate (CTP) imaging, 3D printing, and extreme ultraviolet (EUV) lithography.

This review article is intended to highlight the recent developments and trends in the chemistry of PAGs. It describes recent advances in the molecular design and function of PAGs, which are required to respond to the increasing applications of the photopolymer materials in advanced industries.

In addition, this review summarizes the design of photo-acid generation system corresponding to long-wavelength light source in terms of 1) the shift to long-wavelength in light absorption of PAGs, 2) the utilization of photo-sensitizers [8], and 3) other approaches. Besides, it covers an application of the photoelectron transfer sensitization system using near-infrared light.

Recent advances of highly functionalized PAGs focusing on acid species, the efficiency and the photochemical process of acid generation are also described in detail based on photochemistry reaction mechanism.

Furthermore, this review discusses recent progress of PAGs in advanced EUV resist to improve the trade-off relation among line edge roughness (LER), resolution, and sensitivity. It shows the design of PAGs to effectively utilize a few photons in EUV exposure and to precisely control the deprotection reaction [9,10]. Acid amplifiers and photo-sensitizer precursors to improve the sensitivity of resists are also included.

This review article offers important insights into the better design of PAGs of photopolymer systems for desired applications, and hence deserves the Photopolymer Science and Technology Award.

References

1. J. V. Crivello and E. Reichmanis, *Chem. Mater.*, **26** (2014) 533.

2. N. Corrigan, J. Yeow, P. Judzewitsch, J. Xu, and C. Boyer, *Angew. Chem. Int. Ed.* **58** (2019) 5170.
3. J. V. Crivello, *J. Polym. Sci. Part A: Polm. Chem.*, **37** (1999) 4241.
4. M. Shirai and M. Tsunooka, *Bull. Chem. Soc. Jpn.*, **71** (1998) 2483.
5. C. J. Martin, G. Rapenne, T. Nakashima, and T. Kawai, *J. Photochem. Photobiol. C*, **34** (2018) 41.
6. N. Zivic, P. K. Kuroishi, F. Dumur, D. Gigmes, A. P. Dove, and H. Sardon, *Angew. Chem. Int. Ed.*, **58** (2019) 2.
7. H. Kimura, M. Itou, and J. Yamamoto, *J. Network Polymer*, **28** (2007) 101.
8. T. Tsuchimura, K. Shimada, Y. Ishiji, T. Matsushita, and T. Aoai, *J. Photopolym. Sci. Technol.*, **20** (2007) 621.
9. H. Tsubaki, T. Tsuchihashi, and T. Tsuchimura, *J. Photopolym. Sci. Technol.*, **22** (2009) 77.
10. T. Tsuchimura and T. Kawabata, *J. Photopolym. Sci. Technol.*, **30** (2017) 645.

Seiji Nagahara, Tokyo Electron Ltd.

Journal of Photopolymer Science and Technology
Volume 36, Number 1 (2023) 5 − 6 ©2023SPST

The Photopolymer Science and Technology Award

The Photopolymer Science and Technology Award No. 222100, the Best Paper Award 2021, was presented to Seihou Jinnai and Yutaka Ie (The Institute of Scientific and Industrial Research (SANKEN), Osaka University) for their outstanding contribution published in Journal of Photopolymer Science and Technology, **34**, (2021) 285–290, entitled "Synthesis, Properties, and Photovoltaic Characteristics of Arch- and S-shaped Naphthobisthiadiazole-based Acceptors".

Seihou Jinnai

Seihou Jinnai is an assistant professor of Prof. Ie group in SANKEN, Osaka University, Japan. He received his Ph.D from Osaka University in 2017 under the supervision of Professor Yoshio Aso. After he engaged in research on functional organic dyes as a corporate researcher at Orient Chemical Industries Co., Ltd. from 2016 to 2019, he joined the present research group. His research focuses on development of new π-conjugated systems for organic electronics and photo-functional applications.

Yutaka Ie

Yutaka Ie received his Ph.D in 2000 at Osaka University, Japan under the supervision of Prof. Shinji Murai. After working in Sumitomo Pharmaceuticals Co., Ltd. as a research scientist for three years, he joined Prof. Yoshio Aso group as an assistant professor in the Institute of Scientific and Industrial Research (SANKEN), Osaka University, and was promoted to an associate professor in 2009. He was also a PRESTO researcher at JST between 2010-2014. Since 2019, he has been a full professor at SANEKN, Osaka University. His current research focuses on the development of novel organic molecules for organic electronics and single-molecule electronics.

π-Conjugated compounds have been intensively developed as organic semiconducting materials for organic solar cells (OSCs) [1,2]. The active layer of OSCs is composed of a blend of donor and acceptor materials, which form a bulk-heterojunction structure [3]. Low band-gap polymers have been extensively utilized as donor materials to acquire broad absorption [4]. However, poly(3-hexylthiophene) (P3HT) is still considered one of the most promising practical donors due to the advantages of cost-effectiveness and bulk availability [5,6]. Focusing on the acceptor materials, nonfullerene acceptors (NFAs), which comprise planar π-conjugated backbones and electron-accepting units, have attracted significant attention due to their tunable electronic properties, synthetic accessibilities, and structural diversities [7,8]. Several C_{2v}-symmetric (arch-shaped) NFAs, such as ZY-4Cl [9] and Y6 [10], have reportedly shown photovoltaic characteristics due to their high carrier mobilities and crystallinities, as well as the optimal phase separations of their blend films [11–13]. However, investigations into the influence of structural symmetry on acceptor performance are limited.

We have developed electron-accepting π-conjugated materials including a C_{2h} symmetric naphtho[1,2-*c*:5,6-*c*′]bis[1,2,5]thiadiazole (NTz)

unit [14], and found that NTz derivatives are promising constituents for NFAs [15–17]. The corresponding structural C_{2v} isomer of NTz, naphtho[1,2-*c*:7,8-*c'*]bis([1,2,5]thiadiazole (vNTz), was first synthesized by Mataka *et al.* in 1991 [18]. However, acceptor materials comprising extend π-conjugated systems bearing vNTz units have not yet been investigated in detail [19]. In this Communication, we designed and synthesized new electron-accepting compounds containing vNTz or NTz groups as electron-accepting units; these units are structural isomers. The vNTz-based compounds have an arch-shaped molecular backbone with C_{2v} symmetry, whereas the NTz-based compound forms an S-shaped molecular backbone with C_{2h} symmetry. Upon comparing vNTz to NTz derivative, it was evident that the low-symmetry unit (vNTz) of the former material provided it with a higher solubility than that of the latter. Photophysical and electrochemical measurements showed unique behavior originating from the vNTz core. An organic solar cell comprising the vNTz-based compound and P3HT showed a power conversion efficiency (PCE) of 2.06%, and the thin films containing vNTz-based compound has a favorable surface for photo-carrier generation.

These results were also presented at the Annual Conference of Photopolymer Science and Technology in 2021. In addition, more recently, a follow-up paper investigating the novel application of OSCs based on NTz-containing NFAs were published by the same group [20,21]. The results presented in this Communication will provide new important insights into the molecular design of NFAs based on NTz core for the improvement of PCEs, and hence deserves the Photopolymer Science and Technology Award.

References

1. G. Li and Y. Yang, *Nat. Photon.*, **6** (2012) 1531.
2. O. Inganäs, *Adv. Mater.*, **30** (2018) 1800388.
3. G. Yu, J. Gao, J. C. Hummelen, F. Wudl, and A. J. Heeger, *Science*, **270** (1995) 1796.
4. Y. Li, *Acc. Chem. Res.*, **45** (2012) 723.
5. A. Wadsworth, Z. Hamid, M. Bidwell, R. S. Ashraf, J. I. Khan, D. H. Anjum, C. Cendra, J. Yan, E. Rezasoltani, A. A. Y. Guilbert, M. Azzouzi, N. Gasparini, J. H. Bannock, D. Baran, H. Wu, J. C. d. Mello, C. J. Brabec, A. Salleo, J. Nelson, F. Laquai, and I. McCulloch, *Adv. Energy Mater.*, **8** (2018) 1801001.
6. S. Chatterjee, S. Jinnai, and Y. Ie, *J. Mater. Chem. A*, **9** (2021) 18857.
7. C. Yan, S. Barlow, Z. Wang, H. Yan, A. K.-Y. Jen, S. R. Marder, and X. Zhan, *Nat. Rev. Mater.*, **3** (2018) 18003.
8. A. Wadsworth, M. Moser, A. Marks, M. S. Little, N. Gasparini, C. J. Brabec, D. Baran, and I. McCulloch, *Chem. Soc. Rev.*, **48** (2019) 1596.
9. C. Yang, S. Zhang, J. Ren, M. Gao, P. Bi, L. Ye, and J. Hou, *Energy Environ. Sci.*, **13** (2020) 2864.
10. Q. Liu, Y. Jiang, K. Jin, J. Qin, J. Xu, W. Li, J. Xiong, J. Liu, Z. Xiao, K. Sun, S. Yang, Z. Zhang, and L. Ding, *Sci. Bull.*, **65** (2020) 272.
11. W. Zhu, A. P. Spencer, S. Mukherjee, J. M. Alzola, V. K. Sangwan, S. H. Amsterdam, S. M. Swick, L. O. Jones, M. C. Heiber, A. A. Herzing, G. Li, C. L. Stern, D. M. DeLongchamp, K. L. Kohlstedt, M. C. Hersam, G. C. Schatz, M. R. Wasielewski, L. X. Chen, A. Facchetti, and T. J. Marks, *J. Am. Chem. Soc.*, **142** (2020) 14532.
12. C. Tang, D. Cai, and Q. Zheng, *J. Mater. Chem. A*, **7** (2019) 9609.
13. R. Hou, M. Li, X. Ma, H. Huang, H. Lu, Q. Jia, Y. Liu, X. Xu, H.-B. Li, and Z. Bo, *ACS Appl. Mater. Interfaces*, **12** (2020) 46220.
14. Y. Ie, S. Sasada, M. Karakawa, and Y. Aso, *Org. Lett.*, **17** (2015) 4580.
15. S. Chatterjee, Y. Ie, M. Karakawa, and Y. Aso, *Adv. Funct. Mater.*, **26** (2016) 1161.
16. S. Chatterjee, Y. Ie, and Y. Aso, *ACS Omega*, **3** (2018) 5814.
17. S. Chatterjee, Y. Ie, T. Seo, T. Moriyama, G.-J. A. H. Wetzelaer, P. W. M. Blom, and Y. Aso, *NPG Asia Mater.*, **10** (2018) 1016.
18. S. Mataka, K. Takahashi, Y. Ikezaki, T. Hatta, A. Tori-i, and M. Tashiro, *Bull. Chem. Soc. Jpn.*, **64** (1991) 68.
19. S. Jinnai, Y. Ie, Y. Kashimoto, H. Yoshida, M. Karakawa, and Y. Aso, *J. Mater. Chem. A*, **5** (2017) 3932.
20. S. Jinnai, A. Oi, T. Seo, T. Moriyama, M. Terashima, M. Suzuki, K.-i. Nakayama, Y. Watanabe, and Y. Ie, *ACS Sustain. Chem. Eng.*, **11** (2023) 1548.
21. S. Jinnai, A. Oi, T. Seo, T. Moriyama, R. Minami, S. Higashida, and Y. Ie, *Synthesis*, **53** (2021) 3390.

Hideo Ohkita, Kyoto University
Itaru Osaka, Hiroshima University

Journal of Photopolymer Science and Technology
Volume 36, Number 1 (2023) 7 − 10 ©2023SPST

The Photopolymer Science and Technology Award

The Photopolymer Science and Technology Award No. 232100, the Best Paper Award 2022, was presented to Atsunori Nakamoto, Shinji Yamakawa, Tetsuo Harada, and Takeo Watanabe (Center for EUV Lithography, Laboratory of Advanced Science and Technology for Industry, University of Hyogo) for their outstanding contribution published in Journal of Photopolymer Science and Technology, **35**, (2022) 61-65, entitled "Grazing-Incidence Soft-X-ray Scattering for the Chemical Structure Size Distribution Analysis in EUV Resist".

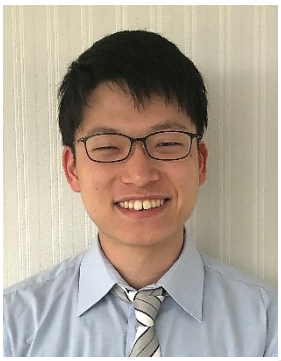

Atsunori Nakamoto

Atsunori Nakamoto is a graduate student in Department of Materials and Synchrotron Radiation Engineering at University of Hyogo, Japan. He received his B.S. degree from University of Hyogo, Japan, in 2022.

Shinji Yamakawa

Shinji Yamakawa is currently Assistant Professor of Center for EUV Lithography, Laboratory of Advanced Science and Technology for Industry, University of Hyogo, Japan. He received his B.S. and M.S. degrees in chemistry from Kansai University, Japan, in 2014 and 2016, and his Ph.D. (Eng.) degree from Tokyo Institute of Technology, Japan, in 2019. He was a specially appointed assistant professor at Tokyo Institute of Technology from 2019 to 2020. His current research interests are the synthesis for EUV resist material and the reaction mechanism analysis of EUV resist under EUV irradiation.

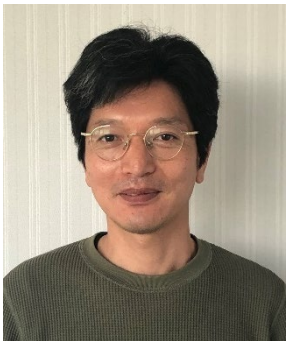

Tetsuo Harada

Tetsuo Harada received the Ph.D. degree in engineering from Tohoku University in 2007. He worked at Tohoku University as research assistant professor from 2007 to 2008. In 2008, He joined the Laboratory of Advanced Science and Technology for Industry of University of Hyogo as an assistant professor. Since 2019, He has been an associate professor. His areas of research interest are EUV and soft X-ray optical engineerings at the NewSUBARU of a synchrotron light facility such as EUV and soft X-ray reflectometry, soft X-ray scattering measurement, resonant soft X-ray absorption measurements, high-power EUV radiation tool, EUV interference lithography, EUV mask microscope, and coherent diffraction imaging for EUV mask pattern.

Takeo Watanabe

Takeo Watanabe is currently Executive Advisor to the President, Director of Center for EUV Lithography, Special Advisor to Director of the Laboratory of Advanced Science and Technology for Industry, and Full Professor, University of Hyogo, Japan. He is expert of extreme ultraviolet lithography (EUVL), advanced lithography, synchrotron science and technology including such as chemical and structure analyses, and imaging using synchrotron. Now he has high activities of fundamental R&D approach to develop the resist, mask, pellicle, and EUV optics for EUVL. And he constructs many equipment at EUVL beamlines of NewSUBARU synchrotron light facilities, such as EUV exposure tools, EUV resist evaluation tools, EUV mask inspection tools, and EUV reflectometer etc.

He received his Ph.D. degree in physics from Osaka City University, Japan, in 1990. From 1990 to 1995, he was a researcher at the Laboratory of Central Research and Development, Sharp Corporation in Japan. Then he joined in the Laboratory of Advanced Science and Technology for Industry, Himeji Institute of Technology (present University of Hyogo) in 1996.

The EUV lithography was proposed as an X-ray reduction exposure system in the late 1980s [1, 2]. After approximately 37 years of first EUVL research had started, it was introduced to the mass-production line of 7 nm+ node (N7+) semiconductor logic devices in 2019, and EUVL has been leading the semiconductor microfabrication to the present [3]. Furthermore, high-NA EUV lithography for the 2 nm node (N2) is scheduled to be launched around 2025 or 2026 and more advanced lithography is required to 0.7 nm node (A7) devices around 2034 in IRDS roadmap [4]. However, the development of EUV resist, which is a photosensitive material indispensable for the next-generation EUV lithography, is currently facing critical technical issues.

EUVL program started from 1996 at NewSUBARU synchrotron light facility [5, 6] of Himeji Institute of technology (present University of Hyogo, Japan). For the first time in the world, the research group achieved to replated 60 nm line and space pattern in the exposure area of 10x10 mm^2 using EUVL exposure tool with the three-aspherical -mirror-projection optics [7-13]. Furthermore, many R&D approaches have been done by this research group, such as EUV resist evaluation using flood exposure tool [14], resist out gassing [15], EUV interference lithography [16, 17] , and such as EUV mask evaluation using EUV reflectometer [18, 19], EUV microscope [20-22], coherent EUV scatterometry microscope (CSM) [23, 24] and μCSM [25], large reflectometer for the optics of collector mirror [26] for EUV LPP source, out-of-band light reflectometer [27], and hydrogen brittle evaluation under high power EUV irradiation [28] and so on.

Next-generation EUV resists are required to have the high resolution of less than 10 nm half pitch, sensitivity of higher than 10 mJ/cm^2 dose, low LWR within 10% of the pattern-line width, and low outgas performance to suppress contamination inside the exposure tool. In particular, if the LWR of resist pattern is large, and the electronic performance, such as the operating speed and power consumption etc., of the semiconductor cannot be improved. The origin of LWR is the stochastic phenomena such as 1) the effect of shot noise, 2) the blurring of secondary electrons and acid diffusion in resist thin film, and 3) the spatial distribution of functional materials in the resist coated on the substrate, such as base polymer, photo reactive compounds (PAG), additives and so on [29, 30]. Recently, the spatial distribution of the chemical components in the resist thin film has attracted attention because it is believed that the localization of the material causes the chemical reaction of the resist to be biased to affect with LWR, and the development of analytical methods are underway [31].

Watanabe *et al.* have published papers in the

Journal of Photopolymer Science and Technology (JPST) where they reported the novel evaluation method of material non-uniformity in resist thin films using resonant soft X-ray scattering (RSoXS) in transmission mode in 2019 and 2020 [32-35]. In these methods, soft X-rays with different incident energies were irradiated on resist thin films coated on Si_3N_4 membranes, and the scattered light intensities were compared. As a result, the scattering spectrum changed for each chemical composition in the resist, revealing the non-uniformity the resist thin film. In addition, it was found that the non-uniformity of the material varies depending on the base-resin, the size of the molecular weight, and the amount of additive such as Photoacid generator and amine.

In this paper [36], the reflection-mode RSoXS method is extended to the measurement of resist thin films coated on silicon wafers. As a result, it is possible to perform the special-distribution measurement of the chemical-contents measurements for the resist spin-coated on a silicon wafer. In particular, RSoXS in reflection mode is a powerful method to analyze to clarify the origin of LWR growth in the thinner resist film, which could not be measured by the conventional method. And it is found that the aggregation grain size increases as becoming the thinner film thickness. This measurement method has high ability to achieve the low LWR on high NA EUVL, which requires thin resist film less than 40 nm, and especially less than 20 nm on hyper NA EUVL such as 0.75 and 0.85.

The results presented in this paper provide a new useful analysis technique of the spatial distribution of chemical component in resist thin films, and hence deserves the Photopolymer Science and Technology Award.

References

1. H. Kinoshita, R. Kaneko, K. Takei, N. Takeuchi, and S. Ishihara, 47th Autumn Meeting of the Japan Society of Applied Physics, 28-ZF-15 (1986) 322.
2. H. Kinoshita, K. Kurihara, Y. Ishii, and Y. Torii, *J. Vac. Sci, Technol. B*, **7** (1989) 1648.
3. J. Miyazaki, and A. Yen, *J. Photopolym. Sci. Technol.*, **32** (2019) 195.
4. https://irds.ieee.org/editions/2022
5. A. Ando, S. Amano, S. Hashimoto, H. Kinoshita, S. Miyamoto, T. Mochizuki, M. Niibe, Y. Shoji, M. Terasawa, and T. Watanabe, *Proc. of the 1997 Particle Accelerator Conference*, (1998) 757.
6. S. Hashimoto, A. Ando, S. Amano, Y. Haruyama, T. Hattori, J. Kanda, H. Kinoshita, S. Matsui, H. Mekaru, S. Miyamoto, T. Mochizuki, M. Niibe, Y. Shoji, Y. Utsumi, T. Watanabe, and H. Tsubakino, *Trans. Materials Research Soc. Japan,* **26** (2001) 783.
7. T. Watanabe, K. Mashima, M. Niibe, and H. Kinoshita, *Jpn. J. Appl. Phys.,* **36** (1997) 7597.
8. T. Watanabe, H. Kinoshita, H. Nii, Y. Li, K. Hamamoto, T. Oshino, K. Sugisaki, K. Murakami, S. Irie, S. Shirayone, Y. Gomei, and S. Okazaki, *J. Vac. Sci. Technol. B*, **18** (2000) 2905.
9. H. Kinoshita, and T. Watanabe, *J. Photopolym. Sci. Technol.,* **13** (2000) 379.
10. H. Kinoshita, and T. Watanabe, *Jpn. J. Appl. Phys.,* **39** (2000) 6771.
11. H. Kinoshita, T. Watanabe, Y. Li, A Miyafuji, T. Oshino, K. Sugisaki, K. Murakami, S. Irie, S. Shirayone, and S. Okazaki, *Proc. SPIE,* **3997** (2000) 70.
12. T. Watanabe, H. Kinoshita, K. Hamamoto, M. Hosoya, T. Shoki, H. Hada, H. Komano, and S. Okazaki, *Jpn, J. Appl. Phys.,* **41** (2002) 4105.
13. K. Hamamoto, T. Watanabe, H. Tsubakino, H. Kinoshita, T. Shoki, and M. Hosoya, *J. Photopolym. Sci. Technol.,* **14** (2001) 567.
14. T. Watanabe, H. Hada, S. Y. Lee, H. Kinoshita, K. Hamamoto, and H. Komano, *Jpn. J. Appl. Phys.*, **44** (2005) 5866.
15. T. Watanabe, H. Kinoshita, H. Nii, K. Hamamoto, H. Tsubakino, H. Hada, H. Komano, and S. Irie, *J. Vac. Sci. Technol. B,* **19** (2001) 736.
16. Y. Fukushima, Y. Yamaguchi, T. Kimura, T. Iguchi, T. Harada, T. Watanabe, and H. Kinoshita, *J. Photopolym. Sci. Technol.*, **23** (2010) 673.
17. T. Urayama, T. Watanabe, Y. Yamaguchi, N. Matsuda, Y. Fukushima, T. Iguchi, T. Harada, and H. Kinoshita, *J. Photopolym. Sci. Technol*., **24** (2011) 153.
18. M. Hosoya, N. Sakaya, O. Nozawa, K. Hamamoto, O. Nagarekawa, T. Watanabe, and H. Kinoshita, *Jpn. J. Appl. Phys*., **47** (2008) 4898.
19. M. Kuki, T. Uemura, M. Yamaguchi, T. Harada, T. Watanabe, Y. Muramatsu and H. Kinoshita, *J. Photopolym. Sci. Technol*., **28** (2015) 531.
20. K. Hamamoto, Y. Tanaka, S. Y. Lee, N. Hosokawa, N. Sakaya, M Hosoya, T. Shoki, T. Watanabe, and H. Kinoshita, *J. Vac. Sci. Technol. B,* **23** (2005) 2852.
21. Y. Mizuta, M. Osugi, J. Kishimoto, N. Sakaya,

K. Hamamoto, T. Tetsuo Harada, T. Watanabe, and H. Kinoshita, *Proc. SPIE*, **6517** (2007) 651733.
22. K. Takase, Y. Kamaji, N. Sakagami, T. Iguchi, M. Tada, Y. Yamaguchi, Y. Fukushima, T. Harada, T. Watanabe, and H. Kinoshita, *Jpn. J. Appl. Phys*., **49** (2010) 06GD07.
23. T. Harada, M. Nakasuji, T. Kimura, T. Watanabe, and, H. Kinoshita, *J. Vac. Sci. Technol. B*, **29**, (2011) 06F503.
24. M. Nakasuji, A. Tokimasa, T. Harada, Y. Nagata, T. Watanabe, K. Midorikawa, and H. Kinoshita, *Jpn. J. Appl. Phys.*, **51** (2012) 06FB09.
25. T. Harada, H. Hashimoto, T. Amano, H. Kinoshita, and T. Watanabe, *Appl. Phys. Express*, **9** (2016) 035202.
26. H. Iguchi, H. Hashimoto, M. Kuki, T. Harada, T. Watanabe, and H. Kinoshita, *Proc. SPIE*, **9658** (2015) 965819.
27. K. Tsuda, T. Harada, and T. Watanabe, *Proc. SPIE*, **11148** (2019) 111481N.
28. T. Harada, A. Ohgata, S. Yamakawa, and T. Watanabe, *Proc. SPIE*, **11908** (2021) 119080U.
29. T. Kozawa, J. J. Santillan, and T. Itani, *J. Photopolym. Sci. Technol.* **31** (2018) 183.
30. H. J. Levinson, "*Extreme Ultraviolet Lithography*", SPIE Press Book, Bellingham, Washington (2020).
31. X. Hou, M. Li, M. J. Eller, S. V. Verkhoturov, E. A. Schweikert, and P. Trefonas, *J. Micro/Nanolith. MEMS MOEMS*, **18** (2019) 033502.
32. Takeo Watanabe, *the 35th International Conference of Photopolymer Science and Technology*, (2018) Panel symposium.
33. J. Tanaka, T. Ishiguro, T. Harada, and T. Watanabe, *J. Photopolym. Sci. Technol.*, **32** (2019) 327.
34. J. Tanaka, T. Ishiguro, T. Harada, and T. Watanabe, *J. Photopolym. Sci. Technol.*, **33** (2020) 491.
35. T. Watanabe, T. Harada, and S. Yamakawa, *J. Photopolym. Sci. Technol.*, **34** (2021) 49.
36. A. Nakamoto, S. Yamakawa, T. Harada, and T. Watanabe, *J. Photopolym. Sci. Technol.*, **35** (2022) 61.

Itaru Osaka, Hiroshima University

Journal of Photopolymer Science and Technology
Volume 36, Number 1 (2023) 11 − 13 ©2023SPST

Bright Outlook for High-tech Industry

Tetsuya Wadaki
Mitsubishi UFJ Morgan Stanley Securities Co., Ltd
Industry Research Dept.Investment Research Division
Otemachi Financial City Grand Cube, 1-9-2, Otemachi, Chiyoda-ku, Tokyo 100-8127,Japan
wadaki-tetsuya@sc.mufg.jp

We forecast that the semiconductor manufacturing equipment market in 2023 will shrink by 20% year-on-year, grow by 15% in 2024, and grow by 20% in 2025.
The semiconductor manufacturing equipment market is currently in an adjustment phase, and semiconductor manufacturers are putting the brakes on capital investment. Therefore, we believe that the medium- to long-term growth potential of semiconductors and manufacturing equipment will not be damaged, and that the manufacturing equipment industry will return to a growth trajectory after a temporary adjustment.
Keywords: ChatGPT, Trade war, Road map, Category Giant

1. Introduction – Expectation of Chat GPT

One of the things we expect to greatly boost demand for servers, which are the biggest driver of the semiconductor and semiconductor manufacturing equipment market, is pre-learning models used for automatic language generation and translation such as ChatGPT. GPT-n developed by Open AI and BERT developed by Google.
The number of parameters is 110 million for GPT-1 announced in 2018, 1.5 billion for GPT-2 announced in 2019, and 175 billion for GPT-3 announced in 2020[1]. GPT-3 is based on a model called Transformer, which is used in AI translation, and can infer "the word that comes after a certain word" with extremely high accuracy. It is characterized by the ability to automatically generate continuations according to various purposes by simply writing out a sentence or giving the minimum number of lines of programming code, which is also called Few Shot Learning.
OpenAI's ChatGPT, in which Microsoft has invested a large amount, is rapidly gaining recognition because it can be used intuitively (the number of searches for ChatGPT according to Google Trends has increased rapidly recently), and I do not think it will end as a temporary fad. hard.
In the near term, there is a high level of interest in services that utilize language models such as ChatGPT, and in the medium to long term, the spread of chatbot AI with a large number of parameters and high power consumption, such as ChatGPT, will stimulate related investment demand in Japan. View.
The performance of language models such as ChatGPT improves according to the power law of the number of parameters and data size, and the time and cost required for pre-training increase according to the power law of the number of parameters. demand for semiconductors will be stimulated.
The number of days and cost required for GPT-3 pre-training is estimated in "The Cost of Training NLP Models" by A21Labs in Israel. A day, the cost is about $ 45,000. GPT-3 is about 10 million dollars on the 30 days[2].
We estimate that each pre-training session of GPT-3 incurs $1.8 million in running costs such as electricity costs, boosting the semiconductor market by $4 million and the semiconductor manufacturing equipment market by $900,000.
GPUs support the evolution of AI. Since the chip area of GPU has reached the limit of the exposable area and the yield is low, it will be essential to make it chiplet in the future. Since GPUs will be implemented with HBMs, the demand for HBMs and related equipment will be greatly boosted.
In addition, according to the Electronic Times dated February 23, TSMC has seen a rapid increase in emergency orders for semiconductors for AI and data centers from NVIDIA, AMD, and Apple. It looks like it will be back to full capacity. It seems that orders for graphics and AI GPUs from NVIDIA for ChatGPT, CPUs and GPUs for data center servers from AMD, and AI semiconductors for servers from Apple are rapidly increasing.

Received May 2, 2023
Accepted May 10, 2023

The recent surge in interest in ChatGPT and massive orders from NVIDIA and AMD were not anticipated at the beginning of the year.
Despite the recent changes in the business environment surrounding TSMC, including cancellations of large orders and postponement of orders, we believe that overall the situation is positive for the semiconductor manufacturing equipment industry.
Also, it should be noted that ChatGPT is not a goal, but a waypoint. In the future, AI will become more and more sophisticated and will be implemented in various places in society and life. The evolution of ChatGPT will generate an increase in the number of parameters several times the speed of evolution, and an increase in man-hours for pre-learning and demand for semiconductors several times the number of parameters.
The semiconductor and equipment industry promises growth.

2.Some major semiconductor manufacturers are accelerating capital investment

The semiconductor market is not all in recession, but some products are still booming. On February 16th, Infineon Technologies announced a new line for analog/mixed-signal and power semiconductors following the environmental review of the German Federal Ministry for Economic Affairs and Climate Action (BMWK) and the final approval of the company's board of directors. announced that it will start construction of a 300mm plant in Dresden. The plan was announced in November 2022, and at that time, construction was scheduled to start after the European Commission's decision on state subsidies and approval of German subsidy procedures, but demand from customers, mainly automobiles, was increasing. Aiming to meet the rising demand, the company decided to break ground early without waiting for a funding decision. The investment in the new plant will amount to EUR 5 billion, the largest ever for the company. Construction of the new plant is scheduled to start in 2023, and production is scheduled to start in the fall of 2026.
Also on February 16, Texas Instruments (TI) announced plans to build a new 300mm fab adjacent to its existing 300mm fab in Lehi, called LFAB. With a total investment of USD 11 billion, construction is scheduled to start in 2023 and start production in early 2026.
The semiconductor manufacturing equipment market is in an adjustment phase, but demand for some semiconductors such as AI semiconductors and automotive semiconductors is strong, and large-scale investments continue to be made. The main customers of Infineon and TI's semiconductors are presumed to be automobile manufacturers, and testers for in-vehicle semiconductors and wafer transfer systems for IGBTs are likely to benefit.

3. China's semiconductor industry is uncertain

Uncertainty about the future of China's semiconductor and semiconductor manufacturing equipment markets has not disappeared. The US government continues to exert pressure on China's semiconductor industry. Bloomberg reported on January 31, citing industry insiders, that the US government is considering cutting off the Chinese telecom giant from all US tech makers. Four years ago, the U.S. government listed a major Chinese telecommunications equipment maker on the Entity List (EL), which designates companies with national security concerns. , significantly reduced its presence in the 5G base station market. Some officials have reportedly called for a total ban on sales to the company. MUMSS has not been able to confirm the authenticity of the article.
The Democratic Party administration in the United States initially did not substantially strengthen export controls on semiconductor manufacturing equipment to the United States, and American semiconductor manufacturing equipment makers greatly increased their equipment exports to China. Applied Materials will account for 33% of sales to China in the term ending October 2021, and Lam Research will account for 35% in the term ending June 2021. However, in October 2010, the U.S. Department of Commerce announced a number of restrictive measures on exports of advanced semiconductor technology to China, exporting equipment for manufacturing DRAMs of 18nm or less, 3D NAND of 128 layers or more, and logic semiconductors of 14nm or less. subject to regulation. It also barred Americans and permanent residents from supporting the development and production of advanced semiconductors in China. The situation surrounding the Chinese semiconductor manufacturing equipment business has changed completely, and American semiconductor manufacturing equipment manufacturers have withdrawn engineers, service parts, and equipment before customer delivery from China. On January 27, Japan, the Netherlands, and the United States agreed to restrict exports of some advanced semiconductor manufacturing equipment to China.
The reasons for the rapid shift in the United States to tightening its grip on China include the rapid increase in exports of semiconductors from China to Russia after the outbreak of the Ukraine conflict,

and the fact that in addition to the number of papers published on AI, China has also been involved in social implementation. is ahead of the United States, and Chinese foundries have succeeded in developing a 7nm process on par with Intel. In addition, the fact that the major telecommunications equipment manufacturer is challenging itself to manufacture semiconductors and advanced memory without flinching from sanctions seems to have heightened the US government's sense of caution.
China's movement toward in-house semiconductor production is producing some results in non-advanced fields, but we expect that it will be difficult to manufacture competitive semiconductors in advanced fields.
Unlike LCDs and solar cells, which have quickly captured the majority of the global market share, performance fluctuations depending on the installation location of semiconductor manufacturing equipment have a serious impact on yields. Needs tuning. Also, in order to keep up with the 2-3 year cycle of technological innovation, it is necessary to retain engineers.

4. Technological evolution continues ~How to read the miniaturization roadmap~

Technological evolution continues unabated. On February 2, imec updated its semiconductor technology roadmap[3]. imec reviews its roadmap about once every six months. According to the roadmap, the processing size of metal half-pitch, which was 22nm in 2022, will be 16nm in 2016, 16-14nm in 2030, and 16-12nm until 2036, although efforts toward fine processing will continue. , it was suggested that the miniaturization might stop.
imec identified five challenges that the semiconductor industry must overcome: 1) Scaling wall, 2) Memory wall, 3) Power wall, 4) Sustainability wall, and 5) Cost wall, and analyzed them as follows.
1) In order to overcome the scaling wall, in addition to miniaturization by EUVL, the evolution of gate structures from FinFET to GAA and CFET will lead to higher integration of semiconductors. Next to CFET, Atomic Gate, which is a new ultra-thin monolayer material with atomic thickness such as tungsten sulfide and molybdenum, is expected to be promising.
2) Memory wall is a problem that the amount of data transfer between memory and CPU limits CPU performance.
3) Power wall is a problem of heat generation due to increased power consumption of semiconductors. As a solution, BS-PDN (Back-PDN) is formed by forming a multilayer power supply line (Power rail) on a separate wafer and attaching it to the back of the wafer. Side Power Deliver Network) is the most likely candidate.
4) The Sustainability wall is an attempt to control the power and water consumed by semiconductors during the manufacturing process and use, as well as the emission of hazardous substances. Equipment and system manufacturers are listed.
5) Cost wall is a cross-cutting issue for all walls, and in addition to reducing the amount of raw materials used, there will continue to be demand for manufacturing equipment, manufacturing processes, semiconductor structures, etc. with higher cost performance.

5. The Age of Category Giants

In the high-tech industry, we define a category giant as a company that handles products with annual sales of 10 billion yen or more, a market share of 60% or more, and a sales difference of more than twice that of the second-ranked company. , are paying attention.
The customers of category giants have come to rely on the company's ability to solve problems and make proposals, and it is no longer easy for competitors to increase their market share by relying only on catalog specs and costs. Category giants are highly resistant to price pressures and can maintain double-digit operating margins even during recessions, so internal reserves increase with each cycle, allowing for cycles of expansion and reinvestment.
In the semiconductor manufacturing equipment industry, DISCO grinders, dicers, diamond blades, Tokyo Electron coater/developers, Lam Research 3D-NAND etching equipment and plating equipment, Applied Materials PVD, CMP, ASML EUV exposure equipment, ArF liquid This includes immersion exposure equipment, KLA's optical patterned mask inspection equipment, and Lasertec's Actinic patterned mask inspection equipment for EUVL. Our estimate is that the operating profit margin on sales for all products exceeds 30% in fiscal 2022, and despite the price offensives of competitors, our high market share remains unshakable, and our performance is relatively solid.

References

1. Yan Jackleen, Tsutomu Ueno *Deeplearning G Exam*(2021)イスラエルの研究機関
2. A21 Labs *The Cost of Training NLP Models* (2020).
3. IMEC *Smaller, better, faster; imec presents chip scaling roadmap* (2022).

Journal of Photopolymer Science and Technology
Volume 36, Number 1 (2023) 15 − 18 ©2023SPST

Optical Oxygen Measurement using Microneedle of Bioabsorable Polymer

Yukihiro Kanda[1*], Hiroaki Takehara[1, 2], and Takanori Ichiki[1, 2]

[1] Department of Materials Engineering, Graduate School of Engineering, The University of Tokyo, 7-3-1 Hongo, Bunkyo-ku, Tokyo, 113-8656, Japan
[2] Innovation Center of NanoMedicine (iCONM), 3-25-14 Tonomachi, Kawasaki, Kanagawa, 210-0821, Japan
**kanda@bionano.t.u-tokyo.ac.jp*

Microneedles made of polymer materials are attracting attention as minimally invasive medical devices for painless access to the body. To apply microneedles to in-body optical sensing, microneedles with a high aspect ratio (base diameter: 500 μm, height: 2 mm) containing platinum octaethylporphyrin, a phosphorescent probe for oxygen were fabricated using poly(L-lactic acid), a bioabsorbable polymer by vacuum-assisted micromolding process. The tip of the microneedle was excited with UV laser (wavelength: 375 nm), and the quenching time of the phosphorescence was measured by an avalanche photodiode and an oscilloscope at different oxygen partial pressures. The obtained phosphorescence lifetimes at the microneedle tip were approximately 100 μs and the relationship between phosphorescence lifetime and oxygen partial pressure was confirmed to follow the Stern-Volmer equation. This study suggests that microneedles could be applied as a minimally invasive in-body measurement tool by adding optical sensing capabilities to them.

Keywords: Microneedle, Bioabsorbable polymer, Microfabrication, Optical measurement, Oxygen sensor

1. Introduction

Microneedles are known as minimally invasive medical devices for painless access to the body through a skin. Especially, microneedles made of biodegradable polymers, can be safely degraded in tissues even if it broke after insertion [1]. Polymer microneedles are mainly applied for transdermal drug delivery [2-11]. Microneedles for interstitial fluid and blood sampling [12-14] and sensing [15, 16] are also being investigated, but access to blood with polymer microneedles remains challenging. We fabricated the microneedles with a high aspect ratio (base diameter: 500 μm, height: 2 mm) using poly(L-lactic acid) (PLLA), a bioabsorbable polymer, and evaluated their strength to realize microneedles for the painless access to blood vessels [17, 18]. To apply our microneedles to optical sensing, we are aiming to develop microneedle-based oxygen sensing devices using platinum octaethylporphyrin (PtOEP), a phosphorescent probe for oxygen. PtOEP is a metal complex generally used as a phosphorescent probe for oxygen because it has a long phosphorescence lifetime (~100 μs) and high quantum yield at room temperature. It has been reported that phosphorescence by Pt dyes is often quenched by vibrations of hydroxyl groups [19]. Therefore, probes for optical measurement using phosphorescent metal complexes need to be in a state that the phosphorescence intensity and lifetime of the metal complexes are not affected by anything other than oxygen molecules. They are generally dispersed and immobilized in a polymer material [20-22]. In this study, we fabricated PLLA microneedles containing PtOEP and measured the phosphorescence lifetime of the microneedle at different oxygen partial pressures to investigate the application of the microneedles as optical measurement devices.

Received March 31, 2023
Accepted May 9, 2023

2. Materials and methods

The microneedles for optical oxygen measurement were fabricated by mixing and dispersing PtOEP in PLLA during the molding process. The molding process is shown in Fig. 1. First, a poly(dimethylsiloxane) (PDMS) prepolymer (BASE: CAT = 10: 1.5, Sylgard 184, Dow Corning Corp., USA) was cured on the master mold (120 °C, 2 h) and then the PDMS mold was obtained. PLLA (Resomer L 206 S, Sigma-Aldrich Corp., USA) and PtOEP (673625-100MG, Sigma-Aldrich Corp., USA) were mixed (2.5 wt%) on the PDMS mold, and then melted and degassed in a vacuum oven (THERMOVAC VT 210, Kusumoto Chemicals, Ltd., Japan) at 10 hPa, 200 °C. A mechanical pressure of 20 kN/m^2 was applied for 10 h to fill the PDMS mold with melted PLLA. After cooling, the microneedles were obtained.

The optical measurement system constructed for measurement of oxygen partial pressure using the microneedles is shown in Fig. 2. The PLLA microneedle containing PtOEP was excited by UV pulse laser. The phosphorescence was converted into an electrical signal by an avalanche photodiode, and the waveform was observed and recorded with an oscilloscope. The excitation light for the oxygen sensor was provided by a UV laser diode (NDU7212E, Nichia Corp., Japan, wavelength: 375 nm) driven by an LD driver (ALP-7033CB, Asahidata Systems Co., Ltd., Japan). The pulse operation of the excitation light was performed by a function generator (Function/Arbitrary waveform generator 3320A, Agilent Technologies Japan, Ltd., Japan) at a frequency of 1 kHz and an output power of 196.3 mW. The excitation light was irradiated onto the microneedles through an optical fiber (MAF3L1, Thorlabs, Inc., USA) and collimator lens (F950FC-A, Thorlabs, Inc., USA), band-pass filter (FB380-10, Thorlabs, Inc., USA), dichroic mirror (DMLP425, Thorlabs, Inc., USA) and a band-pass filter (FB640-10, Thorlabs, Inc., USA) was used to remove any scattered excitation signal from the data collection. The phosphorescent emission light (wavelength: around 650 nm) was converted to an electric signal through an avalanche photodiode module (APD410A2/M, Thorlabs, Inc., USA). Data were sent to a computer digitizer/oscilloscope (PCI-5114, National Instruments, USA). The phosphorescence lifetime was calculated by fitting an exponential function to the decay curve.

Using the above measurement system, the tip of the microneedle was excited with UV pulse laser, and the quenching time of the phosphorescence was measured at four different oxygen partial pressures (0.017, 0.073, 0.15 and 0.21 atm). The oxygen partial pressure was controlled by N_2 purge and measured by an oxygen gas sensor (XO-2200, New Cosmos Electric Co., Ltd., Japan).

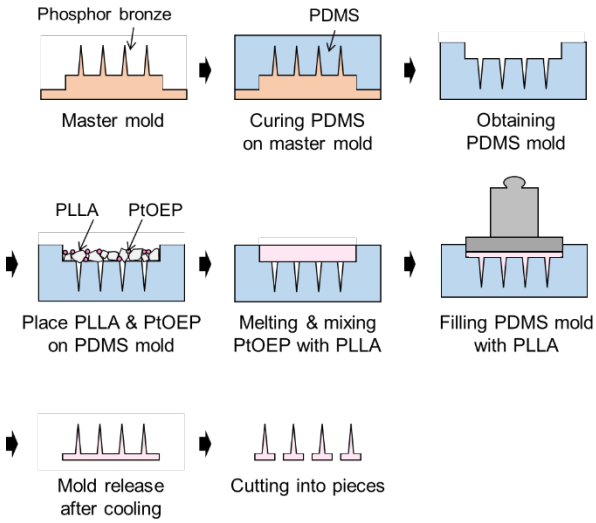

Fig. 1. Schematic of micromolding process of the microneedles for optical oxygen measurement.

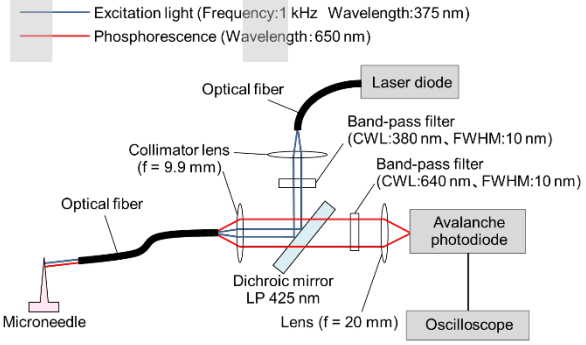

Fig. 2. Schematic diagram of the light path of phosphorescence lifetime measurement system.

3. Results and discussion

Figure 3 shows the fabricated PLLA microneedle containing phosphorescent probes for oxygen, PtOEP (base diameter: 500 μm, height: 2 mm). The oxygen partial pressure was evaluated by measuring the phosphorescence lifetime of the fabricated microneedles at different oxygen partial pressures (0.017, 0.073, 0.15 and 0.21 atm). The typical phosphorescence quenching data are shown in Fig. 4. The quenching time of phosphorescence

was measured five times. The averaged phosphorescence lifetime was 70.5 ± 2.8 μs at an oxygen partial pressure of 0.21 atm, 86.5 ± 5.8 μs at an oxygen partial pressure of 0.15 atm, 82.6 ± 0.3 μs at an oxygen partial pressure of 0.073 atm, and 101.1 ± 1.9 μs at an oxygen partial pressure of 0.017 atm. In the presence of oxygen, the phosphorescence lifetime decreased as a result of the quenching of the excited triplet state by the collision of oxygen molecules with phosphor molecules. It is known that the relationship between phosphorescence lifetime and an oxygen partial pressure can be expressed by the following Stern-Volmer equation [23]

$$\frac{I_0}{I} = \frac{\tau_0}{\tau} = 1 + K_{SV} \cdot P_{O_2} \cdots\cdots\cdots (1)$$

(I_0: phosphorescence intensity in the absence of oxygen, I : phosphorescence intensity in the presence of oxygen, τ_0: phosphorescence lifetime in the absence of oxygen, τ : phosphorescence lifetime in the presence of oxygen, K_{SV} : Stern-Volmer constant, P_{O_2}: oxygen partial pressure)The Stern-Volmer plot of the measured phosphorescence lifetime is shown in Fig. 5. In this plot, the measured phosphorescence lifetime and the oxygen partial pressures exhibited a linear relationship in accordance with the Stern-Volmer equation ($\tau_0/\tau = 1 + 2.03 \cdot P_{O_2}$, $R^2 = 0.94$). It was confirmed that the phosphorescence lifetime obtained from the microneedle tip was responsive to the oxygen partial pressure following the Stern-Volmer equation. These results suggest that the fabricated microneedle can be applied as an oxygen sensor.

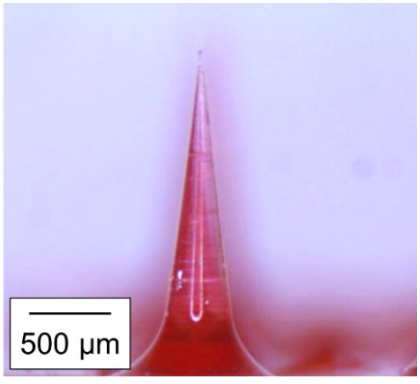

Fig. 3. Photograph of the fabricated microneedle made of PLLA and PtOEP for optical oxygen measurements.

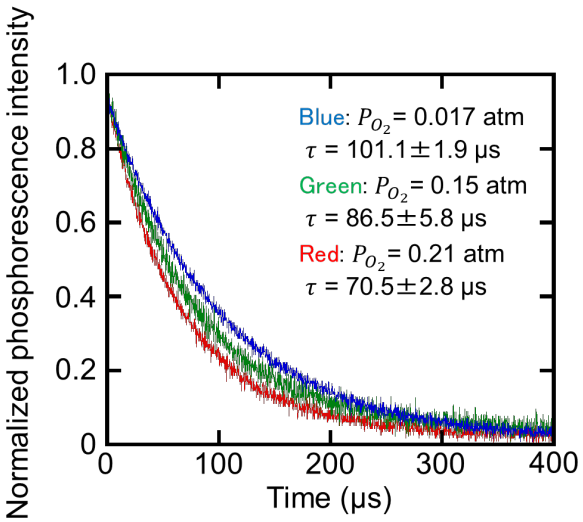

Fig. 4. Typical phosphorescence quenching data at each oxygen partial pressure (red: P_{O_2}= 0.017 atm, blue: P_{O_2}= 0.15 atm, green: P_{O_2}= 0.21 atm).

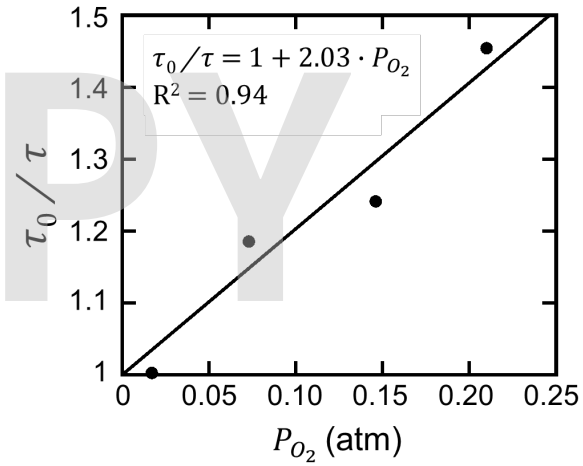

Fig. 5. Stern-Volmer plot of the measured phosphorescence lifetime.

4. Conclusions

To assess the use of bioabsorbable microneedles as optical measurement devices, PLLA microneedles containing phosphorescent probes for oxygen, PtOEP were prepared by vacuum-assisted micromolding process. The obtained phosphorescence lifetime at the microneedle tip was confirmed to be responsive to oxygen partial pressure following the Stern-Volmer equation. Microneedles have conventionally been developed as devices for minimally invasive drug administration, but this study suggests that microneedles could be applied as a minimally invasive in-body measurement tool by adding optical sensing capabilities to them.

Acknowledgements

The authors thank Mr. S. Tsuchiya for providing technical assistance. This research was supported financially by Grants-in-Aid for Japan Society for the Promotion of Science (JSPS) Research Fellow (Grant No. 21J14930), Japan Agency for Medical Research and Development (AMED) (Grant No. JP22he0422015), and the Japan Science and Technology Agency (JST) through the open innovation platform for industry-academia co-creation (COI-NEXT) Program (Grant No. JPMJPF2202)]. Part of this research was conducted at the Advanced Characterization Nanotechnology Platform of The University of Tokyo, supported by the Nanotechnology Platform Program of the Ministry of Education, Culture, Sports, Science and Technology (Grant No. JPMXP09F20UT0026).

References

1. J. W. Lee, M. Han, and J. Park, *J. Drug Target.*, **21**(3) (2013) 211.
2. M. Wang, L. Hu, and C. Xu, *Lab Chip*, **17** (2017) 1373.
3. M. Heckele and W. K. Schomburg, *J. Micromech. Microeng.*, **14** (2004) R1.
4. S. Hirobe, H. Azukizawa, K. Matsuo, Y. Zhai, Y. S. Quan, F. Kamiyama, H. Suzuki, I. Katayama, N. Okada, and S. Nakagawa, Pharm. Res., **30**(10) (2013) 2664.
5. Y. Hiraishi, T. Nakagawa, Y. S. Quan, F. Kamiyama, S. Hirobe, N. Okada, and S. Nakagawa, *Int. J. Pharm.*, **441**(1-2) (2013) 570.
6. K. Tsioris, W. K. Raja, E. M. Pritchard, B. Panilaitis, D. L. Kaplan, and F. G. Omenetto, *Adv. Funct. Mater.*, **22**(2) (2012) 330.
7. S. Baek, J. Shin, Y. Kim, *Biomed. Microdevices*, **19**(1) (2017) 1.
8. M. A. Luzuriaga, D. R. Berry, J. C. Reagan, R. A. Smaldone, and J. J. Gassensmith, *Lab Chip*, **18** (2018) 1223.
9. S. Naito, Y. Ito, T. Kiyohara, M. Kataoka, M. Ochiai, and M. Takeda, *Vaccine*, **30**(6) (2012) 1191.
10. M. Ling and M. Chen, Acta Biomater., **9**(11) (2013) 8952.
11. J. Fang, C. Liu, R. Hsu, Y. Chen, W. Chiang, H. D. Wang, and S-H. Hu, *Polymers*, **12**(6) (2020) 1392.
12. C. G. Li, C. Y. Lee, K. Lee, and H. Jung, *Biomed. Microdevices*, **15**(1) (2012) 17.
13. B. P. Chaudhri, F. Ceyssens, P. De Moor, C. Van Hoof, and R. Puers, *J. Micromech. Microeng.*, **20**(6) (2010) 064006.
14. E. Caffarel-Salvador, A. J. Brady, E. Eltayib, T. Meng, A. Alonso-Vicente, P. Gonzalez-Vazquez, B. M. Torrisi, E. M. Vicente-Perez, K. Mooney, D. S. Jones, S. E. J. Bell, C. P. McCoy, H. O. McCarthy, J. C. McElnay, and R. F. Donnelly, *PloS one*, **10**(12) (2015) e0145644 .
15. G. Gattiker, K. Kaler, and M. Mintchev, *Microsyst. Technol.*, **12**(1) (2005) 44.
16. C. G. Li, H. Joung, H. Noh, M. Song, M. Kim, and H. Jung, *Lab chip*, **15**(16) (2015) 3286.
17. Y. Kanda, H. Takehara, and T. Ichiki, *Jpn. J. Appl. Phys.*, **58** (2019) SDDK05.
18. Y. Kanda, H. Takehara, and T. Ichiki, *Appl. Phys. Express*, **15** (2022) 106503.
19. R. N. Gillanders, M. C. Tedford, P. J. Crilly, and R. T. Bailey, *Anal. Chim. Acta*, **502** (2004) 1
20. Y. Amao, T. Miyashita, and I. Okura, *React. Funct. Polym.*, **47** (2001) 49.
21. P. Hartmann, M. J. P. Leiner, and M. E. Lippitsch, Anal. Chem., **67** (1995) 88.
22. K. Eaton and P. Douglas, *Sens. Actuators B: Chem.*, **82** (2002) 94.
23. A. Mills, *Sens. Actuators B: Chem.,* **51** (1998) 60.

Journal of Photopolymer Science and Technology
Volume 36, Number 1 (2023) 19 − 23 ©2023SPST

Vertical Chemical Unit Operation Using Microcapillary Arrays for Immunosorbent Assay

Mana Honkawa[1], Isao Kawaji[2], Sho Amano[1], Akimobu Yamaguchi[1], Masahiro Takeo[2] and Yuichi Utsumi[1*]

[1] Laboratory of Advanced Science and Technology for Industry, University of Hyogo 1, Kamigorii, 678-1205, Japan
[2]Graduate School of Engineerin, University of Hyogo 6, Himeji, 671-2280, Japan
**utsumi@lasti.u-hyogo.ac.jp*

In order to detect substances using microfluidic devices, fluidic filters with microcapillary arrays with a high aspect ratio were fabricated using deep X-ray lithography. Also, the pressure required to move the solution held on the filter to the lower reservoir was 1~10 kPa in the 10~60 μm capillary diameter range. The microcapillary arrays enable vertical fluid control by integrating various unit chemical operations such as valves, reservoirs, mixers, and reaction fields, where the capillary wall surface was used as a reaction field for highly sensitive detection of the nonylphenol. As a result, it was possible to detect concentrations near the natural environmental existence values defined by The Ministry of the Environment, Japan. This would allow the device to be used for the detection of environmental substances. We also detected mouse IgG using a fluidic filter and found the possibility of detecting enzymatic reactions with a trace amount of reagent.

Keywords : Microchannel, X-ray Lithography, Microcapillary, Fluidic filter, Micro reactor, ELISA

1. Introduction

Microfluidic devices perform various unit chemical operations in microfluidic channels. Because of the small scale of microfluidics, the short diffusion distance and a large specific surface area allow for fast, high-yield reactions and analysis with a small amount of reagent. Therefore, it is expected to detect rapidly and with high sensitivity in medical, food, and environmental substance measurements. Non-natural compounds contain a variety of chemicals, including endocrine disruptors and toxic substances that can have adverse effects on cells. Endocrine disruptors are exogenous substances that, when taken into an animal's system, affect the normal hormonal functions of the body, and can have serious effects from mother to child from generation to generation. Therefore, comprehensive and systematic in situ analysis needs to be performed easily and with high sensitivity in order to obtain guidelines for reducing environmental pollutant. The nonylphenol (NP)[1-3], a type of endocrine disruptor, is used as a synthesis and raw material for the nonylphenol polyethoxylate, which has been used in large quantities as an industrial cleaner and antioxidant for plastic products. Since NPs are not easily degraded in the environment, they can remain in the environment for a long period of time and cause abnormal sexual differentiation and reproductive failure in some wild animals due to their

Received March 31, 2023
Accepted May 18, 2023

disrupting effects. The Ministry of the Environment, Japan has set the predicted no effect concentration of NPs in fish at 0.608μg/kg. Therefore, from the perspective of effective monitoring and conservation of the natural environment, there is an urgent need to establish a system for rapid and highly sensitive analysis of large volumes of environmental samples.

In this study, a fluidic filter for micro reactor[4-7] with microcapillary arrays with a high aspect ratio with thousands of micro threaded holes was fabricated by deep X-ray lithography using synchrotron radiation[8-12] and assembled into a two-layered vertical micro reactor[13-14] to form a three-dimensional fluidic network with multiple integrated functions using stacked structures[15-18]. The vertical reactor has one inlet on the upper reservoir and one on the lower reservoir. Solution and air are injected from the upper reservoir and discharged from the lower reservoir. Vertical fluid operation was performed by the fluidic filter [19-20] inserted between the two reservoirs. When liquid is filled onto the filter, with the affinity between the liquid and the sidewall of the capillary large, and the diameter of the microcapillaries small enough, the liquid does not flow out from the filter but is retained inside the filter. When pressure is applied to the upper reservoir while liquid is held on the filter, the pressure breaks the surface tension of the liquid and the liquid begins to flow out. In addition, the liquid is stirred because of the strong gradient of the fluid velocities in each capillary of the filter as it passes through. In a series of vertical fluid operation processes, the fluidic filter functions as a valve that holds the fluid due to surface tension, as a mixer that mixes the fluid by passing through the filter, and as an immune reaction field by immobilizing antibodies against the inner wall of the microcapillary. In this study, we investigated the possibility of using these functions of the fluidic filter to analyze the endocrine disruptors the nonylphenol and mouse IgG with high speed and sensitivity using an Enzyme-Linked Immunosorbent Assay (ELISA) by vertical chemical manipulation.

2. Experimental

2-1. Fluidic filters fabrication

Fluidic filters with microcapillary arrays used as valves, reservoirs, reaction fields, etc. were fabricated. Fluidic filters were fabricated using deep X-ray lithography at the LIGA beamline (BL2) of the NewSUBARU synchrotron radiation facility established in Hyogo Prefecture, Japan. Experimental conditions are shown in Table 1.

Table1. Exposure conditions

Mask	X-ray mask for micro capillary arrays
Material	PMMA 200(μm)
Does amount	10000(mA・sec/mm)
Scan width	35(mm)
Scanning speed	1(mm/sec)
Gas	He 0.1(atm)
Stores ring energy	1.5(GeV)

The microcapillaries are fabricated with diameters ranging from 10 μm to 50 μm, respectively, and the structure consists of more than 2,000 capillaries integrated in a circle with a diameter of 3 mm. After exposure, the PMMA fluidic filters were developed and fabricated. The development conditions are shown in Table 2 and the fabricated fluid filters are shown in Figure 1.

Table2. Development conditions

Developing solution	GG Developer (Diethlene glycol 60vol%, Morpholine 20vol%, Ethanolamine 5vol%, Water 15vol%,)
Development time	6~36(h)
Bath temperature	25(℃)
Method	Ultrasonic vibration
Primary rinse	Diethylene glycol 80vol%, Deionized water 20vol%
Secondary rinse	Deionized water

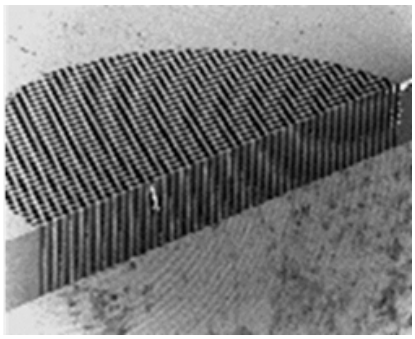

Fig. 1 Fabricated fluidic filter

The vertical reactors using vertical chemical unit operations for executing ELISA were achieved assembling the multi-functional fluid filters.

2-2. ELISA property of the fluidic filter without assembling inside the vertical reactor.

In this experiment, an ELISA property for trace reagents was performed using the fluidic filter without assembled inside the vertical reactor. In the sandwich method, the antigen to be measured is conjugated to the first antibody immobilized on the solid phase to induce an antigen-antibody reaction. Next, the enzyme-labeled antibody to which the enzyme is bound is reacted as a second antibody, and the antigen is sandwiched with the second antibody. The activity of the enzyme labeled on the second antibody is then measured as the degree of optical absorption. Since the binding of the second antibody depends on the amount of antigen bound to the first antibody, the greater the amount of antigen, the greater the amount of coloration. The reagents and conditions used in the experiment are listed in Table 3. Immobilization and blocking of the first antibody to the fluidic filter was performed by immersion overnight (8~12h) at 4°C in the solution. The absorption of each concentration was measured at 450 nm and 630 nm using an absorbance spectrophotometer.

Table3. Experimental conditions for ELISA using only capillary arrays

Reagent	Concentration and reagent amount	Reaction time
Anti-Mouse IgG antibody	10(ng/mL), 5mL	8~12(h)
Blocking solution	Diluted 4 times, 5mL	8~12(h)
Mouse IgG	0.1, 1, 10(ng/mL), 10(μL)	30(min)
Mouse IgG-HRP complex	62.5(ng/mL), 10(μL)	30(min)
Substrate	TMB, 70(μL)	8(min)
Reaction stopper	1M(phosphoric acid), 70(μL)	

2-3. Detection of Nonylphenol using the vertical reactor

The fabricated fluidic filters and vertical reactors were used to detect NPs. The detection method of NPs is described below. Since NPs, the substance to be measured, are small molecules, they were detected by a competitive ELISA. Competitive ELISA is a method in which a substance to be measured and antigen to which an enzyme is preconjugated reacts competitively against an antibody immobilized on a solid phase surface. In this experiment, to use a microcapillary as a reaction field for ELISA, anti-NP antibodies were immobilized on the inner wall of the capillary by physisorption, and the NP-HRP complex and NPs reacted competitively against the immobilized the anti-NP antibody, and the HRP activity of the NP-HRP complex reacting on the solid phase was measured. Here the HRP refers to Horseradish peroxidase. Immobilization of the anti-NP antibody on the inner wall of the microcapillary was performed by immersing the fluid filter in the anti-NP antibody solution. The experimental conditions are listed in Table 4.

Table4. Experimental conditions for the NP measurement

Reagent	Concentration and reagent amount	Reaction time
Anti-NP antibody	0.5(μg/mL),1(mL)	8~12(h)
NP	0, 0.1, 0.2, 0.4, 0.8, 1.6, 3.2(μg/mL),25(μL)	30(min)
NP-HRP complex	Diluted 2500 times, 25(μL)	
Fluorescent Substance	50(μL)	20(min)
Reaction stopper	150(μL)	

Next, vertical fluid operation using a vertical reactor is described. When a fluid filter with immobilized the anti-NP antibody is sandwiched between two reservoirs of the vertical reactor and a mixed solution of the NP and the NP-HRP complex is injected from the upper reservoir by a syringe, the solution enters the capillary and is retained without leaking downward due to the valve function. At this time, the anti-NP antibody immobilized on the inner wall of the capillary reacts with the mixed solution of the NP and the NP-HRP complex. After a certain time, pneumatic pressure is applied from a syringe to the upper layer, causing the liquid to move downward and be discharged. Next, fluorescent substrate was injected to induce an enzymatic reaction of the NP-HRP complex bound to the anti-NP antibody, and the reaction was stopped after a certain time elapsed. This operation was performed with the solutions and reaction times in Table 4. After the reaction was stopped, the reaction solution was extruded into another container, and fluorescence measurements were performed with the excitation and detection wavelengths of the fluorometer set at 320 nm and 405 nm.

3. Result and discussion

3-1. ELISA with fluidic filters

The results of trace reagent measurement of mouse IgG by sandwich ELISA using fluidic filters are shown in Figure 2.

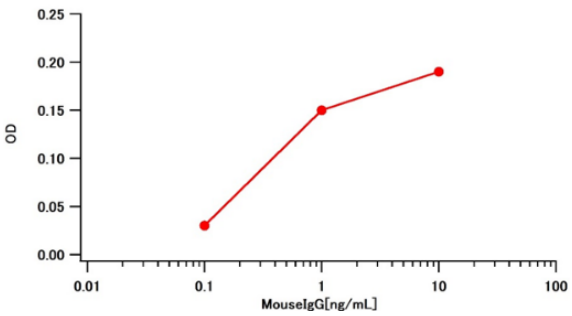

Figure 2. Calibration curve for ELISA with microcapillary arrays

From the above figure, an increase in absorbance was observed with increasing antigen concentration. In addition, a larger change in absorbance was observed in the antigen concentration range of 0.1~1 ng/mL than ELISA on normal 96-well microtiter plate. This gave us the possibility of using PMMA fluidic filters as a reaction field for ELISA to detect with a trace amount of reagent.

3-2. The nonylphenol detection

The results of the NP detection by competitive ELISA using a vertical reactor is shown in Figure 3. We attempted to create a calibration curve for the NP in the concentration range around 0.608 μg/L of NP using fluorescent substrates.

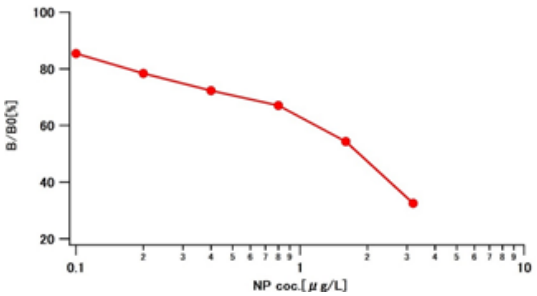

Figure 3 Calibration curve for the NP

From Figure 3, a calibration curve showing an inhibition rate of approximately 90~30% was obtained in the measurement range of 0.1~3.2 μg/mL the NP concentration. Based on these results, it seems possible to detect with high sensitivity concentrations near the predicted no-effect concentration of 0.608 μg/kg for fish in the NP as specified by the Ministry of the Environment, Japan.

4. Conclusion

In this study, fluidic filters with microcapillary arrays with high aspect ratio were fabricated using deep X-ray lithography, and their functions as valves, reservoirs, and reaction fields for chemical reactions were utilized to control vertical fluid flow and detect enzyme reactions. An ELISA for trace reagents was performed using the fluidic filter without assembled inside the vertical reactor as the reaction field, and the samples were detected with high sensitivity in the low concentration range. Also, the detection of the NP using the vertical reactor was highly sensitive near the no-effect concentration specified by the Ministry of the Environment, Japan. The measurements performed in this study using a vertical reactor were made with a large amount of injected solution relative to the reaction field, and it is considered that unreacted solution is present after the reaction time has elapsed. In addition, diffusion of molecules occurs during the reaction, with the degree of diffusion varied from trial to trial, which may cause measurement errors. Therefore, it is necessary in the future to bring the volume of the reaction field and the amount of reagent used closer together, so that more accurate detection can be achieved.

5. Reference

[1]A. Soares, B. Guieysse, B. Jefferson E. Car tmell, J.N. Lester, Environment inter. 34 (2008) 1033
[2]Z. Mao, X. F. Zheng, Y. Q. Zhang, X. X. Tao, Y. Li, & W. Wang, Inter. J. Molecular. Sci.,13 (2012) 491
[3] Paul H. Brunner, S. Capri, A. Marcomini, and W. Giger, Water Research 22(1988)1465
[4]H. Hisamoto, T. Saito, M. Tokeshi, A. Hibara, and T. Kitamori, Chem. Commun. (Cambridge) (2001) 2662.
[5]S. J. Haswell, R. J. Middleton, B. O'Sullivan, V. Skelton, P. Watts, and P. Styring, Chem. Commun. (Cambridge) (2001)39.
[6]H. Lu, M. A. Schmidt, and K. F. Jensen, Lab Chip 1, (2001)22.
[7]M. Gheorghe, D. Dascalu, and M. Ghita, Proc. SPIE 3680 (1999) 1159
[8]A. Ando, S. Amano, S. Hashimoto, H. Kinoshita, S. Miyamoto, T. Mochizuki, M. Niibe, Y. Shoji, M. Terasawa, T. Watanabe and N. Kumagai: J. Synchrotron Rad. 5 (1998) 342
[9]A. Ando, T. Hattori, K. Hosono, K. Kanda, H. Kinoshita, S.Matsui, H.Mekaru, M. Niibe, Y. Utsumi, and T. Watanabe, J. Jpn. Soc. Synchrotron Rad Res. 15 (2002) 336
[10]Y. Utsumi, and Takefumi Kishimoto, J.Vac.Sci.Technol. B 23(2005)2903
[11]Y. Utsumi, Takefumi Kishimoto, Tadashi hattori, and Hirotsugu Hara, Jpn. J. Appl. Phys., 44, 7B (2005)5500
[12]M.Takeuchi, A,Yamaguchi and Y. Utsumi, J. Synchrotron Rad. 26 (2019) 528
[13]Y. Utsumi, T. Asano, Y. Ukita, K. Matsui, M. Takeo, S. Negoro, J. Vac. Sci. Technol. 24 (2006) 2606
[14] Y. Ukita, T. Asano, K. Fujiwara, K. Matsui, M. Takeo, S. Negoro, and Y. Utsumi, Microsyst Technol 14(2008)1573
[15]B. H. van der Schoot, S. Jeanneret, A. van den Berg and N. F. de Rooij: Sens. Actuat. B 15–16 (1993) 211.
[16]T. C. Kuo, D. M. Cannon, W. Feng, M. A. Shannon, J. V. Sweedler and P. W. Bohn: Proc. Micro Total Analysis Systems, (2001) p60
[17]Y. Kikutani, H. Hisamoto, M. Tokeshi and T. Kitamori: Proc. Micro Total Analysis Systems, (2001) p161
[18]K. Ikuta, S. Maruo, T. Fujisawa and A. Yamada: MEMS99, (1999) P 376
[19]T. Asano, Y. Ukita, K. Matsui, M. Takeo, S. Negoro and Y. Utsumi, Microsyst Technol 13 (2007)441
[20]Y. Ukita, T. Asano, and Y. Utsumi, Microsyst Technol 13 (2007)435

Journal of Photopolymer Science and Technology
Volume 36, Number 1 (2023) 25 − 30 ©2023SPST

Spatial Distribution Imaging of Resist Thin Film with Micrometer Resolution using Reflection Type Soft X-ray Projection Microscope

Shuhei Iguchi[1], Tetsuo Harada[1], Shinji Yamakawa[1*], Takeo Watanabe[1], Takeharu Motokawa[2]

[1] Center for EUV Lithography, Laboratory of Advanced Science and Technology for Industry, University of Hyogo
1-1-2, Kouto, Kamigori, Ako-gun, Hyogo, 678-1205, Japan
[2] Institute of Memory Technology Research & Development, Kioxia Corporation
1, Komukai-Toshiba-Cho, Saiwai-ku, Kawasaki, Kanagawa, 212-8582, Japan
** s.ymkw@lasti.u-hyogo.ac.jp*

The spatial distribution observation of resist thin films is important for developing high-performance EUV resists with low line-width roughness property. In our previous study on resist spatial distribution evaluation, aggregation at the micrometer scale was indicated. We developed the reflection-type soft X-ray projection microscope equipped with a capillary mirror optics for focusing. The spatial resolution of this microscope was evaluated in a spatial resolution of a several micrometers. A thin film of a positive-tone chemically amplified resist coated on a glass substrate was observed by this microscope, which had not been patterned. The observation photon energy was around the carbon K-edge absorption region (280 – 300 eV). Non-uniform spatial distribution by reflection mode was observed with a size of several-ten micrometers, which indicated the carbon material aggregation. The micrometer-scale aggregation observation in the resist thin film was very significant to achieve low line-width roughness (LWR).

Keywords: EUV resist, EUV lithography, soft X-ray microscope, aggregation, chemical contrast imaging, capillary mirror optics

1. Introduction

EUV lithography has enabled the mass production of semiconductor devices with 16 nm half-pitch lines. For further miniaturization using EUV lithography, the most important issue is the development of a resist with low line-width roughness (LWR) because the performance of semiconductor devices is limited by the LWR of its LSI pattern. The LWR requirement is generally 1/10 or less of the line width. In the case of 10 nm line and space (L/S) pattern, it requires less than 1 nm. Thus, the line width controllability requires the atom size level. To reduce the LWR, reducing the photon shot noise and spatial non-uniformity of resist components, such as base polymer, protecting group, photoacid generators (PAG), quenchers etc., is significant [1]. Uniform resists are particularly important for next-generation EUV lithography with high spatial resolution. Many measurement methods for the chemical-components distribution analysis of the resist thin films such as time-of-flight secondary-ion mass spectrometry [2-5], and massive-cluster secondary-ion mass spectrometry [6] have been reported. To evaluate the spatial distribution of resist thin films at nanometer scale, we developed two kinds of tools such as the resonant soft X-ray scattering (RSoXS) in transmission mode [7-9] and that in reflectance mode (RSoXR) [10-12] at the BL-10 beamline of the NewSUBARU synchrotron light facility. Since carbon is the main component of the resist, the resonant absorption around the carbon K-edge

Received April 5, 2023
Accepted May 12, 2023

(photon energy of 284 eV) enhanced the contrast of the chemical bond, which would be the functional group such as protecting group of the base resin and the PAG. Reflectance measurements indicated resist film segregation at the surface and bottom. The scattering measurements indicated aggregation of the resist film at nanometer scale [13, 14]. We also developed a reflection-type RSoXS tool to measure resist thin films coated on a Si wafer [15]. The scatterings at the spatial frequency from 20 to 90 nm were evaluated, indicating aggregation for larger spatial frequencies in the micrometer scale.

Therefore, in this study, we developed a soft X-ray microscope with micrometer spatial resolution. A projection image of the resist thin film on a glass substrate was observed.

2. Experimental

2.1. Absorption spectrum of a thin resist film

The soft X-ray absorption (XAS) spectrum was measured to select the observed photon energy of the soft X-ray microscope. The XAS spectrum measured by the total electron yield (TEY) method [16] is shown in Fig. 1. The positive-tone chemical-amplified resist (p-CAR) was employed as a sample. The absorption increased above the photon energy of 285 eV owing to carbon absorption drastically.

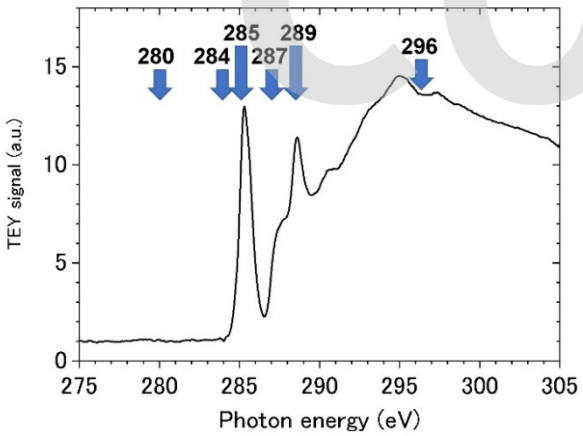

Fig. 1. XAS spectrum of p-CAR by the TEY method around the carbon K-edge.

The resonant absorption peaks at 285, 289, and 295 eV were observed, which correspond to the π* (carbon double bond), acrylate, and σ* bonds, respectively. Absorption was extremely low below the carbon absorption region of less than the photon energy of 285 eV. At the photon energy of 287 eV, the absorption was not high. However, the resonant absorptions at 285 eV and 289 eV were slightly affected. The observation photon energies of this study were 280, 284, 285, 287, 289, and 296 eV as shown in Fig. 1.

2.2. Reflection type soft X-ray projection microscope (RSXRPM)

The schematic layout of the RSXRPM, which was developed at the BL-10 beamline [17, 18] of the NewSUBARU synchrotron light facility which is shown in Fig. 2. The photon energy region of this beamline is from 60 to 950 eV with an energy resolution of more than 1,000, which covers the soft X-ray region including carbon, nitrogen, and oxygen absorption K-edges. The pinhole with a diameter of 100 μm is located at the focusing position of the beamline. The RSXRPM was located 2.1 m downstream from the focus position. The pinhole image was focused by a capillary mirror optic (Sigray), which has an axially symmetric ellipsoidal shape [19]. The reflection at the upper part of the optic is focused behind the sample surface. The focused beam in a sample is reflected the, and the projection image of the sample was recorded by the CCD camera (MTE-2048B Princeton Instrument). The magnification of this microscope depends on the distance from the focusing position on the sample. The distance between the sample and the CCD camera was approximately 164 mm. The CCD camera has a sensing area of 27.6 × 27.6 mm^2 and 2048 × 2048 pixels with a pixel size of 13.5 × 13.5 μm^2. The working distance of the capillary optics is 7.2 mm.

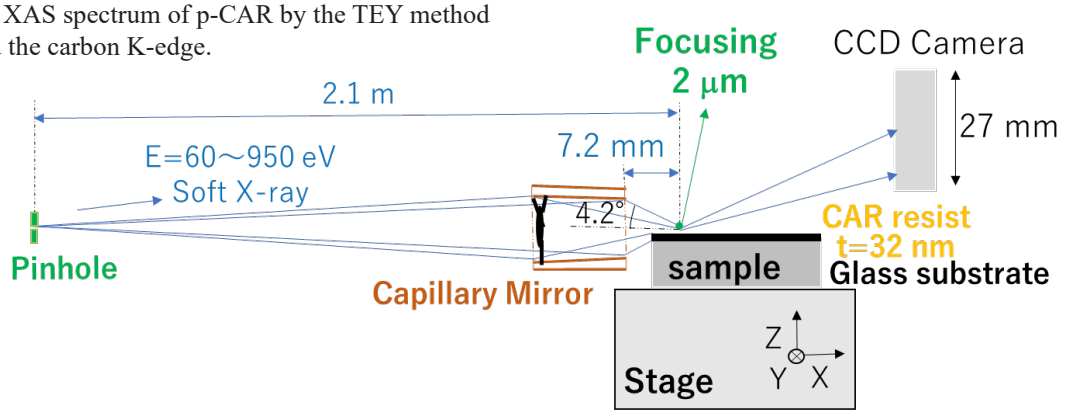

Fig.2 Schematic layout of RSXRPM using the capillary mirror optic.

By the limitation of the working distance, the observation area is limited less than 5 mm from the edge of the sample. The average magnification of the capillary mirror is 1/205, and the designed focusing size is 400 nm. Since this is the reflection type microscope, it can observe a resist thin film coated on a silicon wafer or glass substrate. This is important for resist thin film observation because the aggregation in resist film is strongly dependent on the coating and baking process conditions. The transmission type microscopes are used with much simpler layouts than reflection layouts typically. However, the sample resist must be coated on the membrane. The coating process of the membrane was quite different from that of the wafer and the glass substrate. Therefore, this reflection-type microscope can observe actual a resist-thin-film samples with the actual process, which is significant for resist development.

The observed projection image of the thin film sample of p-CAR is shown in Fig. 3. A bright image with a circular arc shape was recorded, which corresponding to the shape of the capillary mirror. The dark area in the center is the center-stop aperture, which prevents unfocused soft X-rays from the incident pinhole to the sample position. The center stop had three legs as shown in Fig. 4. and two were recorded as shown in Fig. 3. The grazing angle of incidence (GAOI) of the capillary mirror is 2.8°–4.2°, which is dependent on the radius of the pupil. Capillary mirror optics are coated with platinum-single layer. The calculated

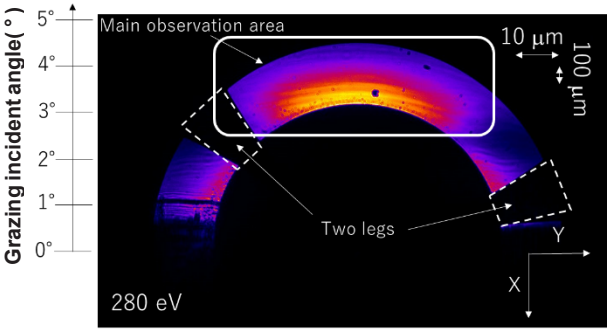

Fig.3 Projection image of a resist thin film on glass substrate at 280 eV.

reflectance of the capillary mirror is >40% in the carbon absorption region, which is a sufficient throughput for this study. The projection image is recorded at the pupil region as a magnified shadow image of the reflection distribution of the sample. The fringe structure of the sample is shown in Fig. 3.

The maximum GAOI of the sample is approximately 4.2° at the upper pupil position. The grazing angle is dependent on the horizontal position of the projection image, as indicated in the left part of Fig. 3. Since the beam illuminated the sample with a grazing angle, the magnification in the vertical direction is 1/14 – 1/23 smaller than that in the horizontal direction in the main observation area. Scale bars of different lengths in the horizontal and vertical directions are shown in Fig. 3. By the difference in the magnification ratio, the sample structure was shown as a fringe shape on the projection image, which would be an isotropic structure on the sample surface.

The sample was coated with p-CAR on a glass substrate with a thickness of 32 nm without any patterns. The sample stage consisted of an XYZ pulse motor stage and an XYZ piezo stage, which was placed on top of the pulse motor [20]. The strokes of the piezo XYZ stage were 100 μm with closed-loop control.

2.3. Spatial resolution of the microscope

Fig.4 shows a copper-grid mesh image with a transmission layout. The capillary mirror angle was aligned to adjust the optical axis. The shadow image (projection image) of the mesh was projected onto the CCD camera. The distortion of this mesh image indicates the residual aberration of the capillary mirror. The mesh had a pitch of 25.6 μm, which was well resolved after alignment. Thus, the spatial resolution was measured at a micrometer scale.

In addition, the resolution of the projection-type microscope was determined from following Eq. (1) and (2), respectively.

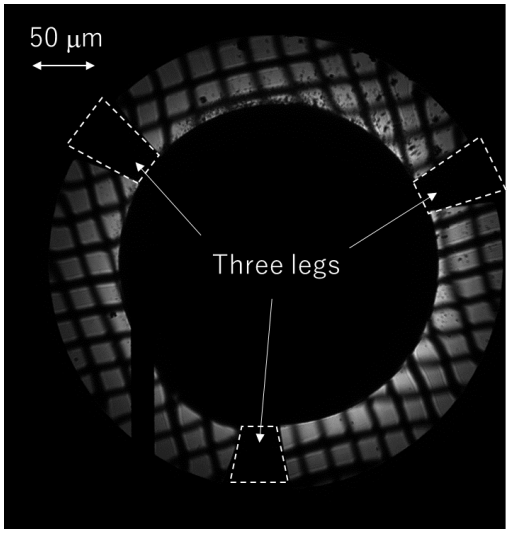

Fig.4 Projection image of the copper mesh at transmission layout.

$$d = \sqrt{d_x^2 + d_F^2} \ldots (1), \quad d_F \approx \sqrt{\lambda b} \ldots (2)$$

Where d_x, λ, and b, indicates the focusing size, the wavelength, and distance from the focusing point to the sample, respectively. The focusing area size is measured by the knife-edge method, which was 2.8 μm in the horizontal direction and 1.2 μm in the vertical direction. The typical b value is in the range from 0.15 to 3.0 mm, which corresponds with the magnification from 1000 to 60, respectively. The typical λ value is in the range from 4.13 to 4.43 nm (280 – 300 eV). Therefore, the resolutions calculated using above Eq. (1) are in the range from 1.5 to 3.7 μm in the horizontal direction and that from 2.9 to 4.5 μm in the vertical direction. The expected beam size calculated using the pinhole size and capillary magnification is 500 nm. The experimental beam size is much larger than the calculated beam size because of residual aberration. If the residual aberration decreases, the resolution is improved to less than 1 μm.

3. Results and discussions

Fig. 5 shows the sample reflection image in the main observation area at the photon energy of 296 eV. There were particles on the image. Some particles were on the sample that moved during stage scanning, and some particles were on the capillary mirror surface that did not move. The magnification of this image can be evaluated using the position difference of the particle on the sample from the two positions of the piezo stage because the piezo stage could move precisely. The evaluated the magnification and field of view (FOV) in the horizontal direction in Fig. 5 are approximately 60 and 150 μm, respectively. This observation was carried out at a low magnification.

In the projection image of Fig. 5, the fringe was recorded as shown in Fig. 3 which was described on the previous page. Since the fringe moved with the stage position change in both the horizontal and vertical directions, the fringe was due to sample reflectance non-uniformity. This non-uniform size was several tens of micrometers in the horizontal and vertical directions. This type of non-uniform image is recorded over the entire area of the sample

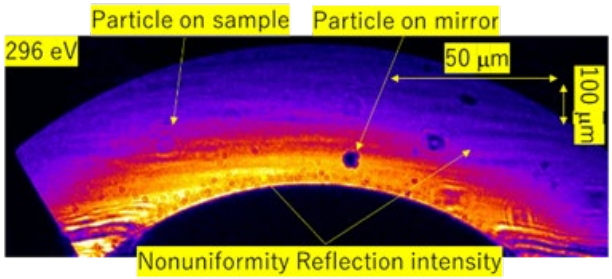

Fig.5 Projection image of the resist thin film with 296 eV at low magnification conditions.

resist. Therefore, the resist has a non-uniform structure several tens of micrometers in scale, which is caused by the aggregation of the resist components.

To evaluate the chemical components of the aggregation, projection images at the same resist positions were observed at 280, 284, 285, 287, 289, and 296 eV as shown in Figs. 6(a) – 6(f). The evaluated the magnification and FOV in the horizontal direction in Fig. 6 were approximately

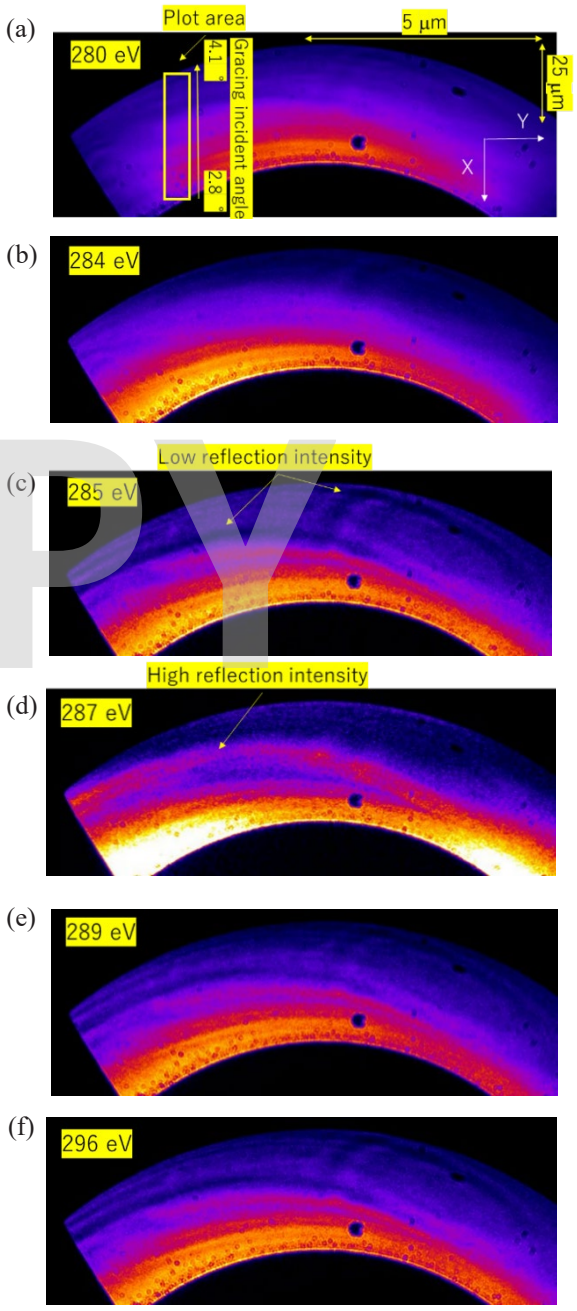

Fig.6 Projection images of the resist thin film at high magnification conditions with the photon energies of (a) 280, (b) 284, (c) 285, (d) 287, (e) 289, and (f) 296 eV. Sample observation position was the same at all photon energies.

1,000 and 10 μm, respectively. This observation was carried out under high-magnification conditions. The intensities were normalized to the maximum intensity in each image. The fringe structures were strongly dependent on the photon energy around the carbon absorption edge. Each image is discussed below.

- At the photon energies of 280 and 284 eV, the absorption was mainly from non-carbon contents, which were not high, and the carbon absorption was very low. Thus, the reflection at the resist surface was low. Since the reflection of the sample was mainly from the substrate reflection, which penetrated the resist film twice, the reflection image corresponds to the total absorption of the resist film. The bright and dark regions indicate the low and high-absorption regions, respectively. The fringe is very weak at these energies. The resist thin film exhibited a small aggregation of non-carbon components, such as oxygen and nitrogen.
- At the photon energy of 285 eV, this energy corresponded to the resonant absorption of the π* bond as shown in Fig. 1, where the absorption was very high. Thus, the beam does not penetrate the resist film onto the substrate. This image corresponds with the surface reflection, which indicates surface-sensitive observation. Since the high-absorption material would cause the high reflection, the bright region was the high-absorption region, which corresponded with the π* bond component of the benzenoid group.
- At the photon energy of 287 eV, carbon absorption was moderately low. The reflection image corresponds to the total absorption of the resist thin film, similar to 280 and 284 eV. However, the absorption of carbon was moderately higher than that of non-carbon components. Thus, the dark region would have a high carbon absorption region, where the fringe contrast is inverse to that of the surface-sensitive energy of 285 eV.
- At the photon energy of 289 eV, this energy corresponds to the resonant absorption of the acrylate bond, where the absorption is very high. Thus, the reflection image was surface-sensitive, similar to 285 eV. The bright region is the high-absorption region, corresponding to the acrylate component.
- At the photon energy of 296 eV, the carbon absorption was high. The reflection image surface was sensitive, similar to 285 and 289 eV. The bright region is the high-absorption region, corresponding to the carbon component.

The fringe structures were recorded with high contrast at 285, 287, 289, and 296 eV. The images correspond to the surface reflections at 285, 289, and 296 eV. At 280 eV, 284 eV, and 287 eV, and the image corresponds to the total absorption of the resist. The reflection intensity profiles are shown in Fig. 7. The horizontal axis represents the vertical positions of the samples. The fringe pitch is approximately 10 μm. The fringe positions were similar at 285, 289, and 296 eV, where surface reflection was recorded. Thus, the spatial distributions of the benzenoid, acrylate, and other carbon bonds were similar. In contrast with 287 eV, the fringe at the 138 μm position was inverted to other energies owing to the inverse absorption contrast. However, at the 125 μm position, the fringe positions were similar. Therefore, the aggregation at the surface and inside the resist would have different one. According to this result, it should be observed at 287 eV to evaluate the aggregation inside the resist. In addition, the surface aggregation of chemical components can be observed at the resonant absorption energies.

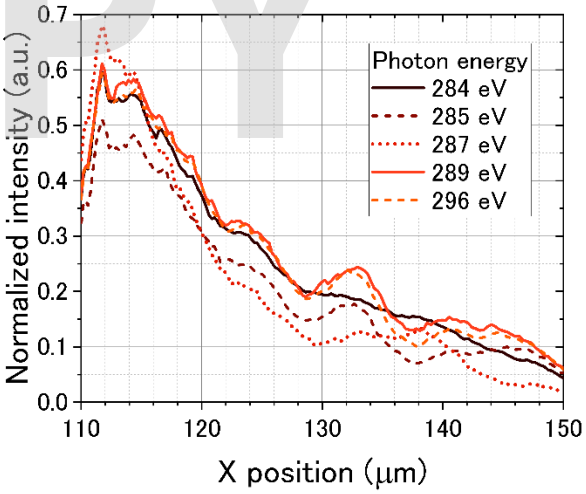

Fig.7 Reflection intensity profiles at the indicated area in Fig. 6(a) with at the photon energies of 284, 285, 287, 289, and 296 eV.

4. Conclusions

We developed an RSXRPM using capillary mirror optics. The spatial resolution was estimated to be several micrometers. According to the observation result of the p-CAR thin film without any pattern, there were non-uniform structures on reflection intensity with a size of several tens of micrometers, which corresponds to carbon aggregation. This aggregation of the resist at

micrometer scale was first observed. In previous study, that of the nanometer-scale aggregation was reported [15]. Both the nanometer-scale and micrometer-scale aggregation would be caused by the polarity, and the difference of these aggregation was the aggregation size. The nanometer-scale aggregation would worse LWR. The micrometer-scale aggregation would cause the local critical-dimension error, local LWR variety, and stochastic-defect concentration. Improvement of these issue is very important for the next-generation EUV lithography. Therefore, the aggregation observation using RSXRPM is helpful.

Acknowledgement

This work was partly supported by JSPS KAKENHI (grant number 21K14212).

References

1. H. J. Levinson, "*Principles of Lithography, Fourth Edition*", SPIE Press Book, Bellingham, Washington (2019).
2. N. Man, H. Okumura, H. Oizumi, N. Nagai, H. Seki, and I. Nishiyama, *Appl. Surf. Sci.*, **231** (2004) 353.
3. T. Hirayama, D. Shiono, S. Matsumaru, T. Ogata, H. Hada, J. Onodera, T. Arai, T. Sakamizu, A. Yamaguchi, H. Shiraishi, H. Fukuda, and M. Ueda, *Jpn. J. Appl. Phys.*, **44** (2005) 5484.
4. T. Hirayama, D. Shiono, J. Onodera, A. Yamaguchi, and H. Fukuda, *Polym. Adv. Technol.*, **17** (2006) 116.
5. T. Hagiwara, T. Ishibashi, M. Terai, T. Kumada, N. Shirota, O. Yokokoji, T. Matsunobe, N. Man, K. Yoshikawa, Y. Tanahashi and T. Hanawa, *J. Photopolym. Sci. Technol.*, **21** (2008) 647.
6. X. Hou, M. Li, M. J. Eller, S. V. Verkhoturov, E. A. Schweikert and P. Trefonas, *J. Micro/Nanolith. MEMS MOEMS*, **18** (2019) 033502.
7. Y. Nakatani, T. Harada, A. Takano, M. Yamada, and T. Watanabe, *J. Photopolym. Sci. Technol*., **30** (2017) 77.
8. F. Liu, M. A. Brady, and C. Wang, *European. Photopolymer. Journal.,* **81** (2016) 555.
9. B. A. Collins, and E Gann, *J. polym. Sci.*, **60** (2022) 1013.
10. T. Ishiguro, J. Tanaka, T. Harada, and T. Watanabe, *J. Photopolym. Sci. Technol*., **32** (2019) 333.
11. M. A. Ruderer, C. Wang, E. Schaible, A. Hexemer, T. Xu, and P. M-Buschbaum, *Macromolecules.*, **46** (2013) 4491.
12. J. Wernecke, H. Okuda, H. Ogawa, F. Siewert, and M. Krumrey, *Macromolecules.*, **47** (2014) 5719.
13. J. Tanaka, T. Ishiguro, T. Harada, and T. Watanabe, *J. Photopolym. Sci. Technol*., **32** (2019) 327.
14. J. Tanaka, T. Ishiguro, T. Harada, and T. Watanabe, *J. Photopolym. Sci. Technol*., **33** (2020) 491.
15. A. Nakamoto, S. Yamakawa, T. Harada, and T. Watanabe, *J. Photopolym. Sci. Technol*., **35** (2022) 61.
16. K. Emura, T. Watanabe, M. Yamaguchi, H. Tanino, T. Fukui, D. Shiono, Y. Haruyama, Y. Muramatsu, K. Ohmori, K. Sato, T. Harada, and H. Kinoshita, *J. Photopolym. Sci. Technol*., **27** (2014) 631.
17. M. Kuki, T. Uemura, M. Yamaguchi, T. Harada, T. Watanabe, Y. Muramatsu, and H. Kinoshita, *J. Photopolym. Sci. Technol*., **28** (2015) 531.
18. T. Fujii, S. Yamakawa, T. Harada, and T. Watanabe, *Proc. SPIE*, **11908** (2021) 119080T.
19. R.J. Koch, C. Jozwiak, A. Bostwick, B. Stripe, M. Cordier, Z. Hussain, W. Yun, and E. Rotenberg, *Synchrotron Rad. News*, **31** (2018)50.
20. Y. Tanaka, T. Harada, T. Amano, Y. Usui, T. Takeo, H. Kinoshita, *Jpn. J. Appl. Phys.*, **53** (2014) 06JC03.

Communication

Journal of Photopolymer Science and Technology
Volume 36, Number 1 (2023) 31 − 39 ©2023SPST

Design of High-sensitive Resist Materials Based on Polyacetals

Hiroyuki Maekawa[1], Yutaro Iwashige[2], Hiroki Yamamoto[3], Kazumasa Okamoto[2], Takahiro Kozawa [2] and Hiroto Kudo[1*]

[1] Department of Chemistry and Materials Engineering, Faculty of Chemistry, Materials and Bioengineering, Kansai University, 3-3-35, Yamate-cho, Suita-shi, Osaka, 564-8680, Japan
[2] National Institutes for Quantum and Radiological Science and Technology, 1233 Watanuki-machi, Takasaki, Gunma, 370-1292, Japan
[3] Institute of Scientific and Industrial Research, Osaka University, 8-1 Mihogaoka, Ibaraki, Osaka 567-0047, Japan
**kudoh@kansai-u.ac.jp*

We examined the synthesis and resist properties of various polyacetals. By the polyaddition of the PDP, TDP, PFPD as A_2 monomers with BVEP (B_2 monomer), TVPM (B_3 monomer), BCA[4]-VE (A_4 monomer), and BCA[8]-VE (A_8 monomer) were investigated to give corresponding linear type [poly(PDP-*co*-BVEP), poly(TDP-*co*-BVEP), poly(PFPD-*co*-BVEP)], hyperbranched type [poly(PDP-*co*-TVPM), poly(TDP-*co*-TVPM), poly(PFPD-*co*-TVPM), and botryosin type [poly(PDP-*co*-BCA[4]-VE), poly(TDP-*co*-BCA[4]-VE), poly(PFPD-*co*-BCA[4]-VE), poly(PDP-*co*-BCA[8]-VE), poly(TDP-*co*-BCA[8]-VE), and poly(PFPD-*co*-BCA[8]-VE)], respectively. The synthesized polyacetals had good physical properties (thermal stability, solubility and film-forming ability) and good film-thickness loss property. Their resist sensitivities in the EB exposure system were higher, i.e., E_0 = 10 μC/cm^2 for poly(PDP-*co*-BVEP), (TDP-*co*-BVEP) and poly(PFPD-*co*-BVEP), E_0 = 30 μC/cm^2 for poly(PDP-*co*-TVPM), poly(PFPD-*co*-TVPM), poly(PFPD-*co*-BCA[4]-VE) and poly(PFPD-*co*-BCA[8]-VE), E_0 = 50 μC/cm^2 for poly(PDP-*co*-BCA[4]-VE) and poly(PDP-*co*-BCA[8]-VE), indicating that these resist materials are good candidate to offer higher resolution resist pattern.

Keywords: High sensitivity, Polyacetal, Hyperbranched, Botryosin, Calixarene

1. Introduction

Lithography system using extreme ultraviolet (EUV) light as the exposure source has been attractive a great deal of attention due to that it enables the formation of sub-10 nm resolution resist pattern. However, EUV resist material still present critical issues known as trade-off: Sensitivity (S), Line edge roughness (L), and Resolution (R) [1]. In order to overcome these issues, it is important to develop a new resist material capable of forming a resist pattern with a small amount of exposure, i.e., it is necessary to develop a higher sensitive resist material [2-7]. At present time, a chemically amplified resist (CAR) system is utilized to increase sensitivity [8-11]. We have also reported the synthesis of the higher sensitive EUV resist materials based on ladder cyclic oligomer noria derivatives ("noria" = water wheel in Latin) [12-20], tannic acid derivatives [21], tellurium-containing compounds [22-23], cage oligomer consistent of calixarene in the main chain [24], botryosin-type polymer [25], and iodine-containing hyper branched polymer [26]. Consequently, resist sensitivities were consistent with the structures of resist materials and these results prompt us the systematical examination of the relationship between the sensitivity and the structure of the resist materials.

In this time, we designed and synthesized of linear polyacetals, hyper branched polyacetals and botryosin type polyacetals. Furthermore, we examined the various physical properties (thermal

Received April 8, 2023
Accepted May 16, 2023

stability, solubility, and film-forming ability) and resist properties (film thickness loss properties, and EB sensitivity).

2. Experimental

2.1. Materials

4,4'-(Propane-2,2-diyl)diphenol (PDP), 4,4'-thiodiphenol (TDP), 4,4'-(perfluoropropane-2,2-diyl)diphenol (PFPD), pyridinium *p*-toluenesulfonate (PPTS), potassium carbonate (K_2CO_3), tri-*n*-octylamine (TOA) and methyl ethyl ketone (MEK) were purchased from Tokyo Kasei Kogyo Co., Ltd. Japan. Tetrahydrofuran (THF) was purchased from FUJIFILM Wako Pure Chemical Co., Ltd. Japan. Tetramethyl ammonium hydroxide aqueous (2.38 wt% $TMAH_{aq}$) was purchased from TAMA CHEMICALS CO., LTD. TPS-109 was used as photo acid generator (PAG), it purchased from Midori Kagaku Co., LTD. THF was dried by distillation from sodium benzophenone ketyl before use. 2,2-Bis[4-{2-(vinyloxy)ethoxy}phenyl]propane (BVEP) was synthesized by means of Williamson-synthesis method using bisphenol A with chloroethyl vinyl ether. By the same way for the synthesis of trihydroxy phenyl methane derivative (TVPM), BCA[4] derivative (BCA[4]-VE), and BCA[8] derivative (BCA[8]-VE) were synthesized and their structures were confirmed by ^{1}H NMR and IR spectroscopy.

2.2. Measurements

Fourier-transform infrared (FT-IR) spectra were taken with a JASCO FT/IR4200. The ^{1}H NMR and ^{13}C NMR spectra were recorded on JEOL ECS-400K (400 MHz and 100 MHz, respectively) instruments in $CDCl_3$ with Me_4Si (TMS) as an internal standard for ^{1}H NMR. Number-average molecular weight (M_n) and molecular weight distribution (M_w/M_n) of the synthesized polymers were measured by size exclusion chromatography (SEC) with a Tosoh HLC-8220 SEC instrument equipped with TSK gel columns (TSKgel Super AW3000 and AW2500 × 2) and refractive-index, using a solution of LiBr and phosphoric acid in DMF (20 mM) as the solvent at flow rate of 0.6 mL/min. Calibration was done with narrow-molecular-weight polystyrene standards (0.5 - 1000 kg/mol). Thermal analysis was performed on a Shimazu thermogravimetric analyzer (TGA) TGA-50/50H at a heating rate of 10 °C/min under nitrogen. Resist thin films were spin-coated (Mikasa 1H-360s) between 80 and 100 nm thickness onto silicon wafers. The film thickness was measured with a film thickness measurement system (spectroscopic ellipsometer with a Photonic Lattice model SE-101 and a Bruker Dektak-XT surface profile). EB sensitivity curves were measured by EB exposure tool (HAMAMATSU EB-ENGINE System, acceleration electron voltage: 50 KeV)

2.3. Synthesis of poly(PDP-*co*-BVEP), poly(TDP-*co*-BVEP), and poly(PFPD-*co*-BVEP)

Typical procedure: A mixture of PDP (3.0 mmol, 0.68 g), BVEP (3.0 mmol, 1.11 g), and PPTS (0.3 mmol, 75 mg) as catalyst in THF (2.4 ml) was stirred at 25 °C. After 12 h, a small amount of NEt_3 was added and the resulting mixture was poured into a large amount of methanol to precipitate the solid, which was collected by decantation. The resulting solid was prepared to be the solution added by $CHCl_3$. Then the organic phase was washed with water thrice, dried over anhydrous magnesium sulfate, and concentrated in a rotary evaporator. The obtained residue was dried *in vacuo* at room temperature for 24 h to afford a white solid [poly(PDP-*co*-BVEP)]. Yield = 1.38 g (77 %). M_n = 2,880. M_w/M_n = 2.01. FT-IR (KBr, cm^{-1}): 3398 (ν O-H), 2929 (ν C-H), 1591 (ν C=C of vinyl), 1485 (ν C=C of aromatic), 1236 (ν C-O of ether), 1130 (ν C-O of acetal), 754 (ν C-S). ^{1}H NMR (400 MHz, $CDCl_3$, TMS) δ (ppm): 1.45 ~ 1.53 (br d, -CH_3), 1.57 ~ 1.68 (br, -CH_3 of acetal), 3.77 ~ 4.25 (br m, -CH_2-, >CH- and O-CH_2-O), 4.88 ~ 4.96 (br, -OH), 5.40 ~ 5.56 (br q, >CH- of acetal), 6.50 ~ 6.59 (br q, CH_2 of vinyl ether), 6.68 ~ 7.47 (br m, aromatic H).

Poly(TDP-*co*-BVEP)**;** The reaction of TDP and BVEP was carried out in the same way for the reaction of PDP and BVEP. Yield = 72 %. M_n = 2,630. M_w/M_n = 1.99. FT-IR (KBr, cm^{-1}): 3398 (ν O-H), 2929 (ν C-H), 1591 (ν C=C of vinyl), 1485 (ν C=C of aromatic), 1236 (ν C-O of ether), 1130 (ν C-O of acetal), 754 (ν C-S). ^{1}H NMR (400 MHz, $CDCl_3$, TMS) δ (ppm): 1.45 ~ 1.53 (br d, -CH_3), 1.57 ~ 1.68 (br, -CH_3 of acetal), 3.77 ~ 4.25 (br m, -CH_2-, >CH- and O-CH_2-O), 4.88 ~ 4.96 (br, -OH), 5.40 ~ 5.56 (br q, >CH- of acetal), 6.50 ~ 6.59 (br q, CH_2 of vinyl ether), 6.68 ~ 7.47 (br m, aromatic H).

Poly(PFPD-*co*-BVEP); The reaction of PFPD and BVEP was carried out in the same way for the reaction of PDP and BVEP. Yield = 86 %. M_n = 2,050. M_w/M_n = 1.80. FT-IR (KBr, cm^{-1}): 3400 (ν O-H), 2965 (ν C-H), 1611 (ν C=C of vinyl), 1513 (ν C=C of aromatic), 1250 (ν C-O of ether), 1171 (ν C-O of acetal), 703 (ν C-F). ^{1}H NMR (400 MHz, $CDCl_3$, TMS) δ (ppm): 1.49 ~ 1.59 (br d, -CH_3),

1.60 ~ 1.77 (br d, -CH_3 of acetal) 3.78 ~ 4.24 (br m, -CH_2-, >CH- and O-CH_2-O), 4.92 ~ 4.98 (br, -OH), 5.49 ~ 5.70 (br d, >CH- of acetal), 6.52 ~ 6.60 (br q, CH_2 of vinyl ether), 6.73 ~ 7.47 (br, aromatic H).

2.4. Synthesis of poly(PDP-*co*-TVPM), poly(TDP-*co*-TVPM), and poly(PFPD-*co*-TVPM).

Typical procedure: The reaction of PDP (4.0 mmol, 0.91 g), TVPM (2.7 mmol, 1.34 g), and PPTS (4.0 mmol, 0.1 g) as catalyst in THF (5.0 ml) was carried out in the same way for the synthesis of poly(PDP-*co*-BVEP). Yield = 1.50 g (67 %). M_n = 3,480. M_w/M_n = 3.38. FT-IR (KBr, cm^{-1}): 3405 (ν O-H), 2933 (ν C-H), 1608 (ν C=C of vinyl), 1508 (ν C=C of aromatic), 1240 (ν C-O of ether), 1126 (ν C-O of acetal). ^{1}H NMR (400 MHz, $CDCl_3$, TMS) δ (ppm): 1.45 ~ 1.53 (s, -CH_3 of acetal), 1.53 ~ 1.68 (m, -CH_3), 3.78 ~ 4.27 (br m, -CH_2-, O-CH_2-O), 4.87 ~ 4.93 (br, -OH), 5.28 ~ 5.39 (m, >CH- of methine), 5.40 ~ 5.51 (br, >CH- of acetal), 6.49 ~ 6.57 (br, CH_2 of vinyl ether), 6.63 ~ 7.15 (br, aromatic H).

Poly(TDP-*co*-TVPM); Yield =75 %. M_n = 3,750. M_w/M_n = 2.68. FT-IR (KBr, cm^{-1}): 3407 (ν O-H), 2933 (ν C-H), 1606 (ν C=C of vinyl), 1509 (ν C=C of aromatic), 1235 (ν C-O of ether), 1131 (ν C-O of acetal), 752 (ν C-S). ^{1}H NMR (400 MHz, $CDCl_3$, TMS) δ (ppm): 1.44 ~ 1.56 (s, -CH_3 of acetal), 3.80 ~ 4.29 (br m, -CH_2-, O-CH_2-O), 4.86 ~ 4.94 (br, -OH), 5.31 ~ 5.39 (m, >CH- of methine), 5.40 ~ 5.51 (br, >CH- of acetal), 6.49 ~ 6.54 (br, CH_2 of vinyl ether), 6.67 ~ 7.34 (br, aromatic H).

Poly(PFPD-*co*-TVPM); Yield = 56 %. M_n = 5,690. M_w/M_n = 2.53. FT-IR (KBr, cm^{-1}): 3407 (ν O-H), 2931 (ν C-H), 1610 (ν C=C of vinyl), 1508 (ν C=C of aromatic), 1252 (ν C-O of ether), 1131 (ν C-O of acetal), 703 (ν C-F). ^{1}H NMR (400 MHz, $CDCl_3$, TMS) δ (ppm): 1.40 ~ 1.59 (s, -CH_3 of acetal), 3.78 ~ 4.30 (br m, -CH_2-, O-CH_2-O), 4.90 ~ 5.28 (br, -OH), 5.28 ~ 5.38 (m, >CH- of methine), 5.45 ~ 5.54 (br, >CH- of acetal), 6.47 ~ 6.57 (br, CH_2 of vinyl ether), 7.03 ~ 7.31 (br, aromatic H).

2.5. Synthesis of poly(PDP-*co*-BCA[4]-VE), poly(TDP-*co*-BCA[4]-VE) poly(PFPD-*co*-BCA[4]-VE).

Typical procedure: The reaction of PDP (4.0 mmol, 0.87 g), BCA[4]-VE (2.0 mmol, 1.86 g), and PPTS (4.0 mmol, 0.1 g) as catalyst in THF (5.0 ml) was carried out in the same way for the synthesis of poly(PDP -*co*-BVEP). Yield = 1.83 g (66 %). M_n = 3,780. M_w/M_n = 1.32. FT-IR (KBr, cm^{-1}): 3417 (ν O-H), 2961 (ν C-H), 1605 (ν C=C of vinyl), 1507 (ν C=C of aromatic), 1234 (ν C-O of ether), 1122 (ν C-O of acetal). ^{1}H NMR (400 MHz, $CDCl_3$, TMS) δ (ppm): 0.69 ~ 1.79 (m, -CH_3), 3.06 ~ 4.53 (br m, -CH_2-, >CH- and O-CH_2-O), 4.68 ~ 4.82 (br, -OH), 5.31 ~ 5.56 (br, >CH- of acetal), 6.42 ~ 6.56 (br, CH_2 of vinyl ether), 6.60 ~ 7.28 (br, aromatic H).

Poly(TDP-*co*-BCA[4]-VE); Yield = 77 %. M_n = 3,050. M_w/M_n = 1.39. FT-IR (KBr, cm^{-1}): 3433 (ν O-H), 2958 (ν C-H), 1591 (ν C=C of vinyl), 1486 (ν C=C of aromatic), 1231 (ν C-O of ether), 1122 (ν C-O of acetal), 634 (ν C-S). ^{1}H NMR (400 MHz, $CDCl_3$, TMS) δ (ppm): 0.72 ~ 1.57 (m, -CH_3), 2.96 ~ 4.56 (br m, -CH_2-, >CH- and O-CH_2-O), 4.64 ~ 4.77 (br, -OH), 5.27 ~ 5.60 (br, >CH- of acetal), 6.39 ~ 6.59 (br, CH_2 of vinyl ether), 6.66 ~ 7.32 (br, aromatic H).

Poly(TDP-*co*-BCA[4]-VE); Yield = 44 %. M_n = 4,590. M_w/M_n = 1.20. FT-IR (KBr, cm^{-1}): 3434 (ν O-H), 2954 (ν C-H), 1611 (ν C=C of vinyl), 1511 (ν C=C of aromatic), 1243 (ν C-O of ether), 1173 (ν C-O of acetal), 704 (ν C-F). ^{1}H NMR (400 MHz, $CDCl_3$, TMS) δ (ppm): 0.66 ~ 1.63 (m, -CH_3), 3.07 ~ 4.55 (br m, -CH_2-, >CH- and O-CH_2-O), 4.65 ~ 4.77 (br, -OH), 5.36 ~ 5.75 (br, >CH- of acetal), 6.40 ~ 6,59 (br, CH_2 of vinyl ether), 6.67 ~ 7.34 (br, aromatic H).

2.6. Synthesis of poly(PDP-*co*-BCA[8]-VE), poly(TDP-*co*-BCA[8]-VE), and poly(PFPD-*co*-BCA[8]-VE).

Typical procedure: A mixture of PDP (4.0 mmol, 0.87 g), BCA[8]-VE (1.0 mmol, 1.86 g), and PPTS (4.0 mmol, 0.1 g) as catalyst in THF (5.0 ml) was carried out in the same way for the synthesis of poly(PDP-*co*-BVEP). Yield = 64 %. M_n = 8,190. M_w/M_n = 3.29. FT-IR (KBr, cm^{-1}): 3410 (ν O-H), 2961 (ν C-H), 1609 (ν C=C of vinyl), 1507 (ν C=C of aromatic), 1237 (ν C-O of ether), 1115 (ν C-O of acetal). ^{1}H NMR (400 MHz, $CDCl_3$, TMS) δ (ppm): 0.24 ~ 1.39 (m, -CH_3), 1.40 ~ 1.67 (s, -CH_3 of acetal), 2.76 ~ 4.31 (br m, -CH_2-, >CH- and O-CH_2-O), 4.32 ~ 4.69 (br, -OH), 5.16 ~ 5.51 (br, >CH- of acetal), 5.97 ~ 6.37 (br, CH_2 of vinyl ether), 6.38 ~ 7.29 (br, aromatic H).

Poly(TDP-*co*-BCA[8]-VE); Yield = 68 %. M_n = 4,260. M_w/M_n = 1.93. FT-IR (KBr, cm^{-1}): 3393 (ν O-H), 2955 (ν C-H), 1594 (ν C=C of vinyl), 1482 (ν C=C of aromatic), 1233 (ν C-O of ether), 1116 (ν C-O of acetal), 682 (ν C-S). ^{1}H NMR (400 MHz, $CDCl_3$, TMS) δ (ppm): 0.42 ~ 1.58 (m, -CH_3), 2.97 ~ 4.59 (br m, -CH_2-, >CH- and O-CH_2-O), 4.68 ~ 5.05 (br, -OH), 5.05 ~ 5.54 (br, >CH- of acetal), 5.90 ~ 6.48 (br, CH_2 of vinyl ether), 6.49 ~ 7.37 (br, aromatic H).

Poly(PFPD-*co*-BCA[8]-VE); Yield = 39 %. M_n =

3,420. M_w/M_n = 1.47. FT-IR (KBr, cm^{-1}): 3412 (ν O-H), 2963 (ν C-H), 1617 (ν C=C of vinyl), 1515 (ν C=C of aromatic), 1246 (ν C-O of ether), 1131 (ν C-O of acetal), 704 (ν C-F). ^{1}H NMR (400 MHz, $CDCl_3$, TMS) δ (ppm): 0.39 ~ 1.61 (m, $-CH_3$), 2.92 ~ 4.49 (br m, $-CH_2-$, >CH- and O-CH_2-O), 4.77 ~ 4.98 (br, -OH), 5.01 ~ 5.64 (br, >CH- of acetal), 5.99 ~ 6.49 (br, CH_2 of vinyl ether), 6.50 ~ 7.40 (br, aromatic H).

2.7. Film forming ability and thickness loss property on silicon wafer in 2.38 wt% tetramethylammonium hydroxide (2.38 wt% $TMAH_{aq}$)

The solutions of the synthesized polymers in methyl ethyl ketone (MEK) were spin-coated on the silicon wafer which were primed with hexamethyldisilazane (HMDS) to prepare corresponding thin films with about 100 nm thickness. The value of thickness of the thin films was determined by ellipsometry before and after soaking in 2.38 wt% $TMAH_{aq}$ for 30 sec.

2.8. Resist sensitivity

The resist solutions of these polymers and oligomer in the presence of 10 wt% of TPS-109 as a PAG and 100 mol% of TOA as a quencher were filtered through a 0.20 μm PTFE syringe filter prior to spin-coating on silicon wafers which were primed with hexamethyldisilazane (HMDS). Spin-coating was performed at 2500 rpm for 30 sec to form thin films on the silicon wafers. Then these spin-coated films were prebaked at 90 ˚C for 60 sec. The resulting films were exposed to EB lithography (HAMAMATSU EB-ENGINE System; the acceleration electron voltage is 50 KeV). The area of exposure was approximately 1 * 1 cm^2. After the exposure, the silicon wafer was post exposure bake (PEB). The PEB temperature and time are 90 °C and 30 s, respectively. Next the silicon wafer developed by dipping in 2.38 wt% $TMAH_{aq}$. at room temperature for 30 s then rinsed in deionized water for 10 s before drying. The resist film thickness was measured with an ellipsometry to obtain sensitivity curves.

3. Results and discussion

3.1. Synthesis of linear and branched polyacetals by the polyaddition of A_2 monomers (PDP, TDP, and PFPD) with B_2 monomer (BVEP) and B_3 monomer (TVPM).

Reaction of PDP and BVEP was carried out using PPTS as a catalyst in THF at 25 °C for 12 h, to give the corresponding soluble polymer poly(PDP-*co*-BVEP) with M_n = 2,880, M_w/M_n = 2.01 in 77 % yield. Its structure was confirmed by ^{1}H NMR and FT-IR spectroscopy. In ^{1}H NMR spectroscopy, the peaks at 6.68 ~ 7.47 and around 5.50 ppm were seen, which were assignable to aromatic protons and acetal group, respectively. This means that polyaddition of PDP and BVEP proceeded to give corresponding a linear polymer. In the same way, the reaction of TDP with BVEP and PFPD was performed to give corresponding linear type polymer poly(TDP-*co*-BVEP) and poly(PFPD-*co*-BVEP) with M_n = 2,050 ~ 2,630, M_w/M_n = 1.80 ~ 1.99 in 72 ~ 86 % yield (Scheme 1). Next, the polyaddition of bisphenols (PDP, TDP, PFPD) as A_2 type monomers and TVPM as B_3 monomer was examined in the similar way as mentioned above. As the result, the corresponding hyperbranched polyacetals poly(PDP-co-TVPM), poly(TDP-*co*-TVPM) and poly(PFPD-*co*-TVPM) M_n = 3,480 ~ 5,690, M_w/M_n = 2.53 ~ 3.38 were obtained in 56 ~ 75 % yield.

3.2. Synthesis of Botryosin type polyacetals by the polyaddition of A_2 monomers (PDP, TDP and PFPD) with B_4 monomer (BCA[4]-VE) and B_8 monomer (BCA[8]-VE).

In our previous report, we examined the reaction of BCA[8] and hexamethylene diisocyanate (HDI), i.e., $A_8 + B_2$ type reaction, and the only soluble polymer poly(BCA[8]-*co*-HDI) could be obtained in satisfactory yield [27]. The structure analysis by MALDI-TOF MS and AFM indicated that poly(BCA[8]-*co*-HDI) consists of nanoscale-gel-shaped structures resembling a bunch of grapes, presumably because the hydroxyl groups of BCA[8] are located at the lower rim and the polymerization of BCA[8] and HDI proceeded homogeneously not to three dimensional cross-linked polymers. We named "Botryosin" after the Greek word botrys, meaning a bunch of grapes. In this time, we examined the reaction of A_2 monomers (PDP, TDP and PFPD) and BCA[8] (BCA[8]-VE) as B_8 monomer. Their reactions were carried out in THF at 25 °C for 150 ~ 720 min in the presence of PPTS as a catalyst, yielding the soluble polymers poly(PDP-*co*-BCA[8]-VE), poly(TDP-*co*-BCA[8]-VE) and poly(PFPD-*co*-BCA[8]-VE) with M_n = 3,420 ~ 8,190, M_w/M_n = 1.47 ~ 3.29 in 39 ~ 68 % yield. Furthermore, the polyaddition of A_2 monomers and BCA[4]-VE were also examined in the same way as mentioned above. As a results, corresponding botryosin type polyacetals poly(PDP-*co*-BCA[4]-VE), poly(TDP-*co*-BCA[4]-VE) and poly(PFPD-*co*-BCA[4]-VE) with M_n = 3,050 ~ 4,590, M_w/M_n = 1.20 ~ 1.39 were obtained in 44 ~ 77 % yields. Their structure was

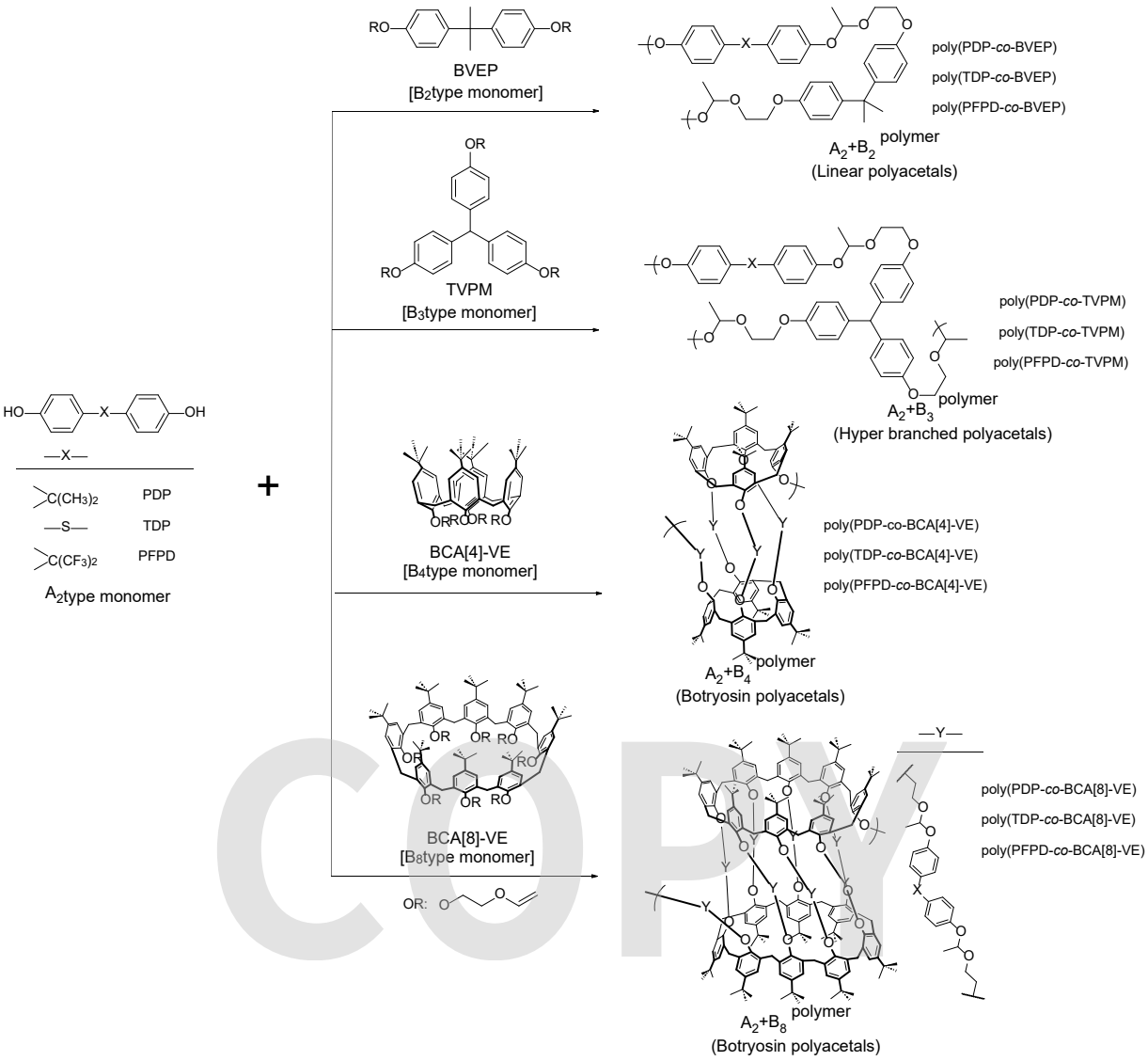

Scheme 1. Synthesis of various polyacetals.

confirmed by ^{1}H NMR and FT-IR spectroscopy and it was suggested that these were botryosin-type polymer.

The structures of the synthesized polyacetals are summarized in Scheme 1 and they have acetal bonds in the main chain, i.e., it was expected that they would perform the main-chain scission type positive resist materials.

3.3. Physical properties (solubility, film-forming ability, thermal stability, and thickness loss property)

Physical properties of synthesized polymer relevant to their applicability as resist materials were examined.

Solubility. The synthesized resist materials were soluble in common organic solvents such as NMP, DMSO, DMF, ethyl acetate, acetone, $CHCl_3$, PGMEA, and MEK. They were also insoluble in MeOH and *n*-hexane.

Film-forming ability. The film-forming ability was examined by spin coating a solution of synthesized resist materials 60 mg in MEK 2.0 g on silicon wafer. As a results, all synthesized polymers could show good film-forming ability and it is about 100 nm that the film thickness on silicon wafer.

Thermal stability. The thermal properties of the synthesized resist materials were determined by TGA. The initial decomposition temperature (T_d^i) of linear polyacetals were in the range between 180 and 197 °C, those hyperbranched polyacetals were

Table 1. Polyaddition reaction of A_2 type monomers with B_n (n = 2, 3, 4 and 8) type monomers

Run	Sample	Yield (%)[a]	M_n (M_w/M_n)[b]	T_d^i (°C)[c]	Film forming ability[d]	Thickness lost (%)[e]
1	Poly(PDP-*co*-BVEP)	77	2,880 (2.01)	197	good	5
2	Poly(TDP-*co*-BVEP)	72	2,630 (1.99)	189	good	4
3	Poly(PFPD-*co*-BVEP)	86	2,050 (1.80)	180	good	3
4	Poly(PDP-*co*-TVPM)	67	3,480 (3.38)	201	good	3
5	Poly(TDP-*co*-TVPM)	75	3,750 (2.68)	205	good	2
6	Poly(PFPD-*co*-TVPM)	56	5,690 (2.53)	199	good	<1
7	Poly(PDP-*co*-BCA[4]-VE)	66	3,780 (1.32)	225	good	2
8	Poly(TDP-*co*-BCA[4]-VE)	77	3,050 (1.39)	235	good	3
9	Poly(PFPD-*co*-BCA[4]-VE)	44	4,590 (1.20)	240	good	<1
10	Poly(PDP-*co*-BCA[8]-VE)	64	8,190 (3.29)	230	good	1
11	Poly(TDP-*co*-BCA[8]-VE)	68	4,260 (1.93)	243	good	2
12	Poly(PFPD-*co*-BCA[8]-VE)	39	3,420 (1.47)	241	good	<1

[a]Insoluble part in MeOH. [b]Estimated by SEC based on polystyrene standards; LiBr and phosphoric acid solution in DMF (20 mM). [c]T_d^i = Initial thermal decomposition temperature determined by TGA. [d]Spin-coated onto silicon wafer.
[e]Measured by ellipsometry at 636 nm.

in the range between 199 and 205 °C. Furthermore, botryosin type polyacetals were in the range between 225 and 243 °C. These means that the synthesized polyacetals have sufficient thermal stability which can be applied as photoresist materials withstand high temperature of nearly 100 °C in prebake and postexposure bake (PEB).

Thickness loss property on the silicon wafer after soaking in 2.38 wt% $TMAH_{aq}$ solution. Next, the value of film thickness loss of the thin films prepared from the synthesized polymer was determined anticipating for the application of positive-type resist materials. As a result, they showed good substrate adhesion. The decrease of their thickness was hardly observed. This means that they can be used as positive resist materials with 2.38 wt% $TMAH_{aq}$ as an alkaline developer. These results are summarized in Table 1.

3.4. Resist sensitivity

At first, the resist sensitivity of linear-type polyacetals [poly(PDP-*co*-BVEP), poly(TDP-*co*-BVEP), poly(PFPD-*co*-BVEP)] and branched-type polyacetals [poly(PDP-*co*-TVPM), poly(TDP-*co*-TVPM), poly(PFPD-*co*-TVPM) was examined using EB exposure tool. Solutions of these resist materials in the presence of 10 wt% of TPS-109 as a PAG in the absence of a quencher in MEK were spin coated on silicon wafer which were primed with hexamethyldisilazane (HMDS) to prepare corresponding thin films with about 100 nm thickness. The postexposure baking (PEB) temperature and times were 90 °C and 30s, respectively. Next, the silicon wafer developments by dipping in 2.38wt% $TMAH_{aq}$ at room temperature for 30s afterward rinsed in deionized water before drying. The value of the thickness of remained thin films was measured by means of ellipsometer after the lithography process. As the result, the values of resist sensitivities (E_0) were very high to be 10 μC/cm^2 (Fig. 1 [A] and [B]). Furthermore, the branched polyacetals containing sulfide could not show full sensitive curve, indicating that some side reaction might be occurred derived from sulfide backbone (Fig. 1 [B]).

When the resist pattern is examined using TOA as a quencher, its sensitivity would be lower and

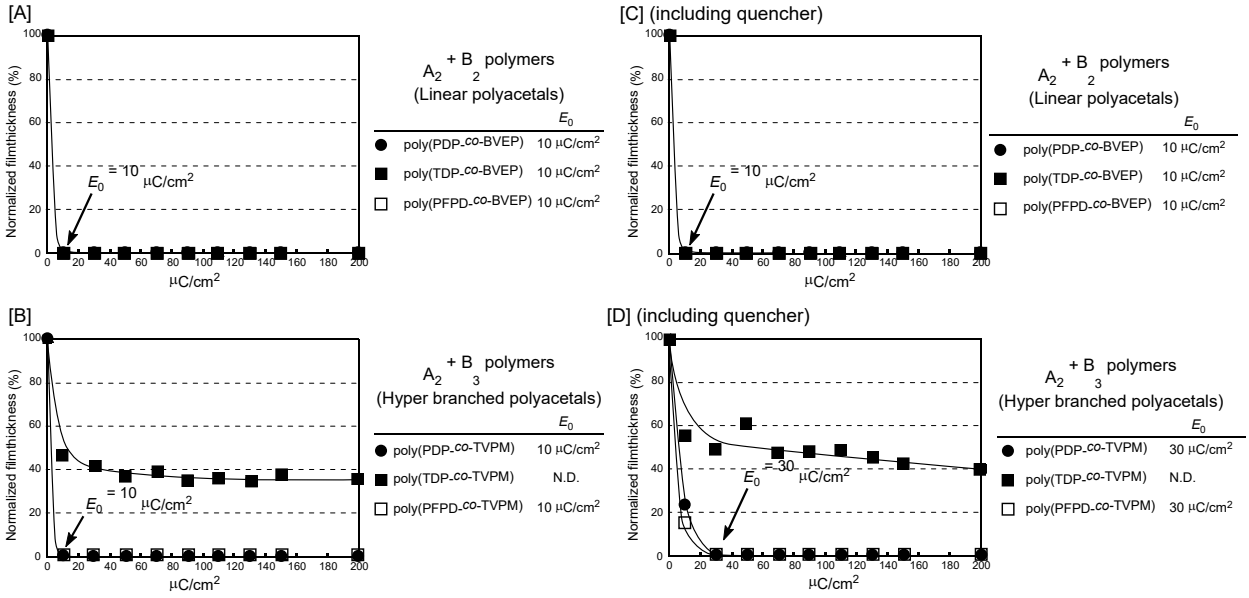

Fig. 1. EB sensitivity curves of linear polyacetals and hyperbranched polyacetals. [A]; linear polyacetals [B]; hyper branched polyacetals [C]; linear polyacetals including quencher [D]; hyper branched polyacetals including quencher.

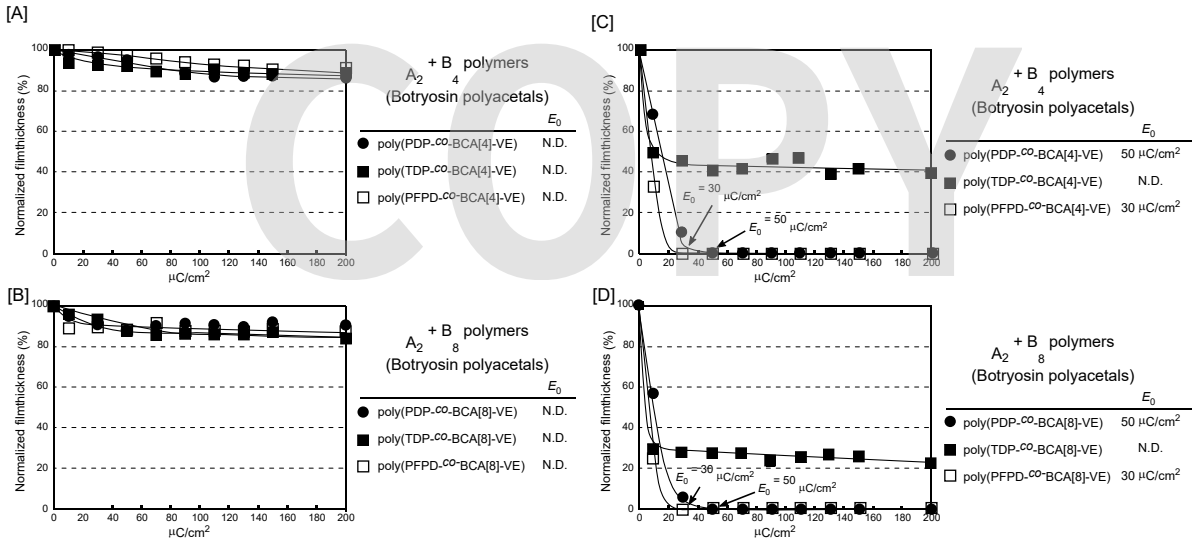

Fig. 2. EB sensitivity curves of botryosin-type polyacetals. [A]; botryosin polyacetals based on BCA[4]-VE, developing in 2.38wt% $TMAH_{aq}$ [B]; botryosin polyacetals based on BCA[8]-VE, developing in 2.38wt% $TMAH_{aq}$ [C]; botryosin polyacetals based on BCA[4]-VE, developing in the mixture of MeOH and 2.38wt% $TMAH_{aq}$ [D]; botryosin polyacetals based on BCA[8]-VE, developing in the mixture of MeOH and 2.38wt% $TMAH_{aq}$.

resolution performance could be expected to improve. Then, we examined resist sensitivities of the thin films prepared by the solutions of the resist materials in the presence of TOA as a quencher to PAG 100 mol% in MEK. In the case of linear type polyacetals, $E_0 = 10$ μC/cm², which was same to that in the absence of TOA (Fig. 1 [A] and [C]). The sensitivities of branched type polyacetals decreased to be $E_0 = 30$ μC/cm².

Next, the EB exposure sensitivity of botryosin-type polyacetals containing BCA[4]-VE and BCA[8]-VE were also examined in the same way. However, the sensitivity curves could not be observed (Fig. 2 [A] and [B]). These results were initially unexpected for us. The decomposition reaction of the acetal bonds should proceed by the acid generator. The reason why the sensitivity curve was not obtained might be due to the

influence of the calixarene skeleton forming botryosin-type polyacetal. It is considered that the calixarene derivatives produced by the decomposition of the acetal bond with the acid generator cannot dissolve in the alkaline developer. Then, the alkaline developer was changed to the mixture of MeOH and 2.38wt% $TMAH_{aq}$ (50v./50v.). As the result, E_0 of poly(PDP-*co*-BCA[4]-VE), poly(PFPD-*co*-BCA[4]-VE), poly(PDP-*co*-BCA[8]-VE), and poly(PFPD-*co*-BCA[8]-VE) were 50, 30, 50, and 30 μC/cm^2, respectively (Figure 2 [C] and [D]).

4. Conclusion

In summary, we examined the synthesis of various polyacetals linear type [poly(PDP-*co*-BVEP), poly(TDP-*co*-BVEP), poly(PFPD-*co*-BVEP)], hyperbranched type [poly(PDP-*co*-TVPM), poly(TDP-*co*-TVPM), poly(PFPD-*co*-TVPM), and botryosin type [poly(PDP-*co*-BCA[4]-VE), poly(TDP-*co*-BCA[4]-VE), poly(PFPD-*co*-BCA[4]-VE), poly(PDP-*co*-BCA[8]-VE), poly(TDP-*co*-BCA[8]-VE), and poly(PFPD-*co*-BCA[8]-VE)]. These have good solubility, good film-forming ability, and high thermal stability which are relevant to the resist materials. Thickness-loss property of these materials were also very good. Their resist sensitivities were examined in the film state using EB exposure system. As the result, higher resist sensitivities could be observed, and their values were consistent with the structures of resist materials. These results showed that the synthesized polyacetals have high potential property to offer higher resolution of resist pattern for next generation resist system.

Acknowledgement

This work was partly supported by Cooperative Research Program “Network Joint Research Center for Materials and Devices”.

References

1. J. Lee, J. Kim, S. Jeong, M. Lim, S. Koo, C. M. Lim, and Y. S. Kim, *SPIE*, **9776** (2016) 612.
2. T. Kozawa and S. Tagawa, *Jpn. J. Appl. Phys*. **49** (2010) 030001.
3. K. Matsuzawa, T. Fujii, S. Matsumura, T. Yamada, Y. Komuro, D. Kawana and K. Ohmori, *J. Photopolym. Sci. Technol.*, **29** (2016) 489.
4. L. Li, X. Liu, S. Pal, S. Wang, C. K. Ober, and E. Giannelis, *P. Chem. Soc. Rev.*, **46** (2017) 4855.
5. A. Narasimhan, L. Wisehart, S. Grzeskowiak, L. E. Ocola, G. Denbeaux, and R. L. Brainard, *J. Photopolym. Sci. Tech.*, **30** (2017) 113.
6. T. Manouras and P. Argitis, *Nanomaterials*, **10** (2020) 1593.
7. Y. Wang, L. Chen, J. Yu, X. Guo, S. Wang, and G. Yang, *Royal Soc. Open Sci.*, **8** (2021) 202132.
8. T. Kozawa and S. Tagawa, *J. Photopolym. Sci. Technol.*, **24** (2011) 137.
9. H. J. Levinson and T. A. Brunner, *SPIE*, **10809** (2018) 5.
10. X. Wang, Z. Tasdemir, L. Mochi, M. Vockenhuber, L. V. Lent-Protasova, M. Meeuwissen, R. Custers, G. Rispens, R. Hoefnagels, and Y. Ekinci, *SPIE*, **10957** (2019) 19.
11. K. Nishikori, K. Kasahara, T. Kaneko, T. Sakurai, S. Dei, K. Maruyama, and R. Ayothi, *SPIE*, **11326** (2020) 185.
12. H. Kudo, R. Hayashi, K. Mitani, T. Yokozawa, N. C. Kasuga, and T. Nishikubo, *Angew. Chem. Int. Ed*. **45** (2006) 7948.
13. X. André, J. K. Lee, A. DeSilva, C.K. Ober, H.B. Cao, H. Deng, H. Kudo, D. Watanabe, and T. Nishikubo, *SPIE* **6519** (2007) 65194B.
14. H. Kudo, D. Watanabe, T. Nishikubo, K. Maruyama, D. Shimizu, T. Kai, T. Shimokawa, and C. K. Ober, *J. Mater. Chem.* **18** (2008) 3588.
15. M. Tanaka, A. Rastogi, H. Kudo, D. Watanabe, T. Nishikubo, and C. K. Ober, *J. Mater. Chem*. **19** (2009) 4622.
16. T. Nishikubo, H. Kudo, Y. Suyama, H. Oizumi, and T. Itani, *J. Photopolym. Sci. Technol*., **22** (2009) 73.
17. H. Kudo, Y. Suyama, H. Oizumi, T. Itani, and T. Nishikubo, *J. Mater. Chem*. **20** (2010) 4445.
18. H. Kudo, M. Jinguji, T. Nishikubo, H. Oizumi, and T. Itani, *J. Photopolym. Sci. Technol.* **23** (2010) 657.
19. H. Seki, Y. Kato, H. Kudo, H. Oizumi, T. Itani, and T. Nishikubo, *Jpn. J. Appl. Phys.* **49** (2010) 06GF06-1.
20. N. Niina, H. Kudo, H. Oizumi, T. Itani, and T. Nishikubo, *Thin Solid Films* **534** (2013) 459.
21. H. Kudo, S. Ohori, H. Takeda, H. Ogawa, T. Watanabe, H. Yamamoto, and T. Kozawa, *J. Photopolym. Sci. Technol.*, **28** (2018) 221.
22. M. Fukunaga, H. Yamamoto, T. Kozawa, T. Watanabe, and H. Kudo, *J. Photopolym. Sci. Technol.*, **30** (2017) 103.
23. H Kudo, M. Fukunaga, T. Yamada, S. Yamakawa, T. Watanabe, H. Yamamoto, K. Okamoto, and T. Kozawa, *J. Photopolym. Sci. Technol.*, **32** (2020) 805.
24. H. Maekawa, H. Kudo, T. Watanabe, H. Yamamoto, K. Okamoto, and T. Kozawa, *J.*

Photopolym. Sci. Technol., **33** (2020) 45.
25. H. Kudo, H. Ogawa, H. Yamamoto, and T. Kozawa, *J. Photopolym. Sci. Technol.*, **29** (2016) 495.
26. Y. Iwashige, H. Kudo, K. Okamoto, and T. Kozawa, *J. Photopolym. Sci. Technol.*, **35** (2022) 41.
27. H. Kudo, M. Shizuma, K. Kubo, and T. Hayashi, *Chem. Lett.*, **44** (2015) 1765.

Journal of Photopolymer Science and Technology
Volume 36, Number 1 (2023) 41 − 45 ©2023SPST

Spatial Distribution Analysis of Polymers in Resist Thin Film by Reflection-mode Resonant Soft X-ray Scattering

Atsunori Nakamoto[1], Shinji Yamakawa[1]*, Tetsuo Harada[1], and Takeo Watanabe[1]

[1]Center for EUV Lithography, Laboratory of Advanced Science and Technology for Industry, University of Hyogo
1-1-2 NewSUBARU, Kouto, Kamigori, Ako-gun, Hyogo 678-1205, Japan
**s.ymkw@lasti.u-hyogo.ac.jp*

For the development of low line width roughness (LWR) resist, it is necessary to achieve uniform spatial distribution of chemical components in resist thin films at the nanometer scale. To evaluate the chemical distribution, we have developed the resonant soft X-ray scattering (RSoXS) technique. In this study, we evaluated the chemical distribution in five resist thin films spin-coated on a silicon wafer by reflection-mode RSoXS at NewSUBARU synchrotron light facility. The samples were also measured by X-ray absorption spectroscopy. At the reflection-mode RSoXS, the scattered light from the sample surface was recorded by the soft X-ray CMOS camera. The grazing angle of incidence was set to 5 degrees for the sample. The scattering profile for each sample represents the chemical aggregation of the resist polymer. A non-chemically amplified resist had low chemical aggregation, and chemically amplified resist had higher chemical aggregation due to its hydroxyl group of base polymers.

Keywords: EUV lithography, LWR, resonant soft X-ray scattering, resist thin film, chemical aggregation

1. Introduction

Extreme ultraviolet lithography (EUVL) with a wavelength of 13.5 nm began to be used for the mass production of 7 nm+ node semiconductor logic devices since 2019. The chemically amplified resist (CAR) is widely used in EUVL. The CAR is composed of a base polymer and a photoacid generator (PAG). The circuit pattern is replicated on the resist coated on the silicon wafer. The low line-width roughness (LWR) of the resist is crucial for achieving high-performance devices. The non-uniform spatial distribution of the chemical components in the resist thin film worsens the LWR. Since the LWR of the resist pattern is large, it is difficult to maintain the electronic performance of the devices, such as the operating speed and power consumption etc. Therefore, development of a low-LWR resist is required. In the case of next-generation EUVL, the target line width is 10 nm or less. The acceptable LWR is less than 1 nm, which is less than 1/10 of the line width. In particular, the depth of focus (DoF) for high numerical-aperture EUV exposure system [1] become smaller than 30 nm. The resist must be thinner than the DoF. However, it has been reported that the LWR worsens when the film thickness becomes thinner [2, 3].

With such challenges, it is necessary to evaluate the spatial distribution of chemical components on the nanometer scale. Previously, we reported the spatial distribution analysis results of the resist using transmission-mode RSoXS and reflection-mode RSoXS tools [4-7]. The RSoXS is a scattering measurement with the soft X-ray around the resonance absorption energy of low-z material [8-15]. This method is also helpful for analyzing the morphology of polymer blend and bilayer films. In this study, we report a spatial distribution analysis of the chemical components in resist thin films using the reflection-mode RSoXS.

Received May 3, 2023
Accepted May 12, 2023

2. Experimental

2.1. Reflection-mode RSoXS

The reflection-mode RSoXS measurements were performed at BL-10 beamline at NewSUBARU synchrotron light facility [7]. At BL-10, the incident photon energy ranges from 60 to 950 eV in the soft X-ray region [15]. Fig. 1 shows a schematic drawing of the reflection-mode RSoXS.

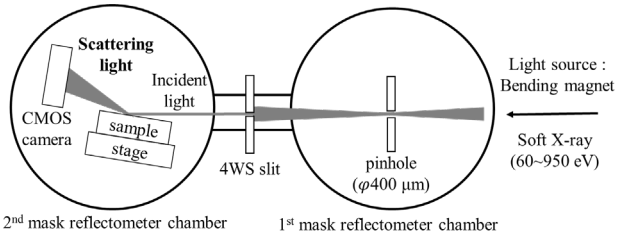

Fig. 1. Schematic drawing of the measurement setup of the reflection-mode RSoXS.

The incident X-ray beam was irradiated from the right to left side in Fig. 1. There are two mask reflectometers. A pinhole with a diameter of 400 μm was introduced in the 1st mask reflectometer chamber at the focusing point of BL-10. Four jaw slit (4WS) was introduced between 1st and 2nd reflectometers. The scattering component of the incident light was cut off by the pinhole and 4WS. The grazing angle of incidence (GAOI) was 5 degrees for each sample. The beam size was 2.4 mm (horizontal) × 1.1 mm (vertical) at the sample position. The vertical beam size on the sample depended on the GAOI, which was approximately 13 mm at 5°. The incident beam was reflected at the sample. Scattered light from the sample was recorded by a soft X-ray CMOS camera [17]. The sensing area size of the camera is 22.5 mm × 22.5 mm. The camera has 2048 × 2048 pixels and a pixel size of 11 μm × 11 μm. The exposure position was changed by the sample stage motion, which had long stroke of 152 mm. The GAOI was changed by the sample rotation stage. The CMOS camera was on the detector rotation stage.

2.2. Resist samples

The five resist samples were measured, which were a base polymer, two CARs, bound-CAR, and ZEP520A resist (ZEON).

The chemical structures of the sample polymers and PAGs are shown in Fig. 2. The base polymer is Poly(hydroxystyrene-*co*-*tert*-butylacrylate) (PHS-TBA). This polymer was also employed as the base polymer for the two CARs. Two PAGs of Triphenylsulfonium triflate (TPS-TfO) and diphenyl[4-(phenylthio)phenyl]sulfonium triflate (DPS-TfO) were blended to PHS-TBA with 2.2 mol% TPS-TfO (CAR(TPS-TfO)) and 2.2 mol% DPS-TfO (CAR(DPS-TfO)). At the boulnd-CAR, a PAG unit was bounded to the polymer with 5.2 mol%, which was prepared according to the procedure in Ref. 18. ZEP520A was used as a non-CAR type. All the samples were coated on a Si wafer with the thickness of 50 nm. The resist-coating conditions are listed in Table 1. We discuss the chemical aggregation behavior of these five resist based on the differences in their chemical structures.

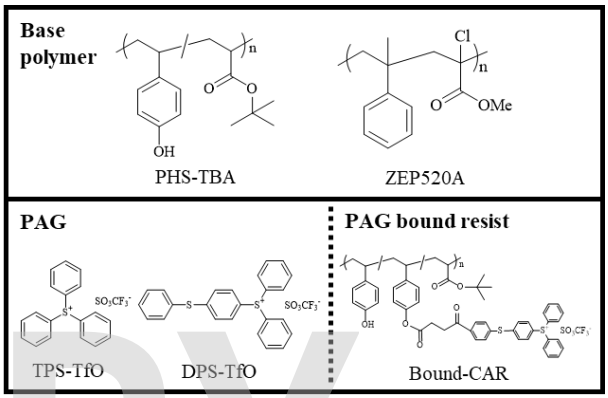

Fig. 2. Chemical structural formulae of the resist samples.

Table 1. Coating conditions for the five samples.

	Wafer processing	Spin-coating	Prebake
PHS-TBA	HMDS processing (110°C, 90 s)	2500 rpm 45 s	130 °C 60 s
PHS-TBA+TPS-TfO CAR(TPS-TfO)			
PHS-TBA+DPS-TfO CAR(DPS-TfO)			
Bound-CAR			
ZEP520A	O_3 ashing (10 min)	3000 rpm, 30 s	180 °C, 180 s

2.3. X-ray absorption spectroscopy (XAS)

The sample resists of PHS-TBA, CAR(TPS-TfO), and ZEP520A were measured by XAS before the RSoXS measurements. The XAS results are shown in Fig. 3. The measured photon energy was around carbon *K*-edge of 270 – 315 eV. The measurement method was total electron yield (TEY) method, which measure the TEY current from the sample. The sample setup was the same as that for the reflection-mode RSoXS measurement, with GAOI of 15°. This large GAOI was selected to prevent interference of the incident and reflected light. In Fig. 3, the vertical axis shows the normalized TEY signal intensity, which corresponds to the X-ray absorption of the resist. The horizontal axis represents the photon energy of the incident soft X-ray beam. The absorption peaks

at 286, 289, and 296 eV were assigned to π* (C=C), π* (C=O), and σ* (C-C) bonds, respectively [7]. The absorption peaks were almost same position for the three resist, because they had similar carbon structure of phenyl and acrylate groups.

In reflection-mode RSoXS, if the sample has high absorption, the incident light cannot penetrate the sample films. Thus, scattering from the sample surface information is dominant in the measured scattering signal [7, 19], which includes the roughness and chemical aggregation at the surface. Because the resist surface on the smooth Si wafer is usually smooth, the scattering signal from the surface chemical aggregation would be dominant. In contrast, if the sample has a low absorption, the reflection from the Si wafer substrate is much higher than that from the resist surface. Because scattering from the Si wafer surface is low owing to its smooth surface, internal scattering signal from the total resist film is dominant. In this study, we would like to measure the chemical aggregation in the resist thin film. Thus, photon energy of 280 eV was selected to measure the internal scattering of the resist thin films, where the carbon absorption was low.

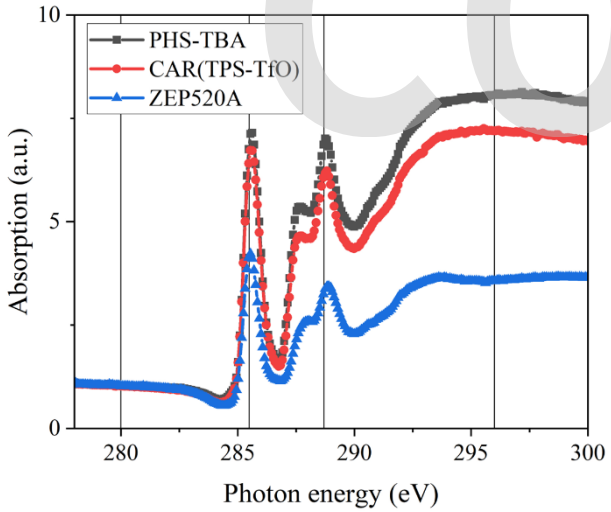

Fig. 3. XAS spectra of PHS-TBA, CAR (TPS-TfO), and ZEP520A around the carbon *K*-edge region.

2.4. Scattering image

A schematic geometry of the reflection-mode RSoXS is shown in Fig. 4. There was very strong direct reflection on the CMOS image, and strong vertical scattering signal, which mainly includes resist information of thickness direction. Because that of horizontal direction was indicated in-plane spatial distribution, we discussed this horizontal scattering profile in this study. The horizontal scattering profile was evaluated from the white dotted line region in the CMOS image, which was normalized to that of the direct beam without the sample.

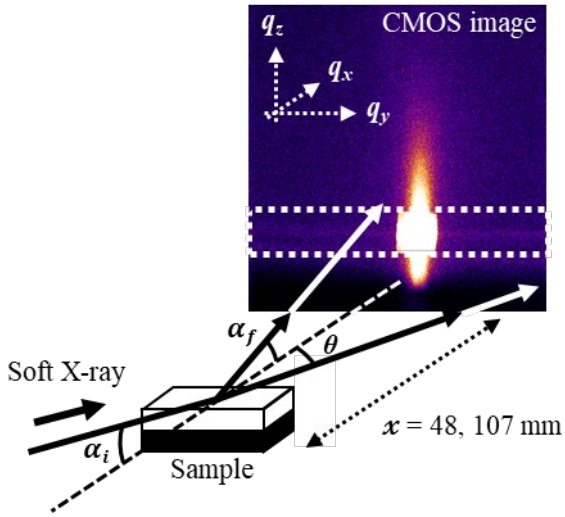

Fig. 4. Schematic geometry of reflection-mode RSoXS

The scattering intensity profile has horizontal axis of scattering vector q_y. The scattering vector in the q_y direction is expressed by the following equation (1).

$$q_y = \frac{2\pi}{\lambda} \sin\theta \cos\alpha_f \qquad (1)$$

The α_i is GAOI. The α_f and θ are the scattering angle of the vertically and horizontally scattered light, respectively. The λ is wavelength of the incident light. The x is camera length from the sample to the camera. This camera length was set at two lengths of x = 48 mm and 107 mm. At a short camera length of 48 mm, the camera can record the scattering signal of a wide scattering angle, which includes high-frequency information. At a long camera length of 107 mm, the camera can record a small scattering angle, which includes low-frequency information.

3. Results and discussion

The results of the reflection-mode RSoXS measurements of the five resist samples are shown in Fig. 5. The camera length x was 48 mm at Fig. 5(a). The scattering vector range is approximately 0.075–0.35 nm^{-1}. The q_y value of 0.20 nm^{-1} and 0.10 nm^{-1} corresponds to spatial frequencies of 30 nm and 60 nm, respectively. The camera lengths x was 107 mm at Fig. 5(b). The scattering vector range is approximately 0.032–0.15 nm^{-1}. The q_y value of 0.05 nm^{-1} corresponds to spatial frequencies of 120

nm. In this setup, ZEP520A, PHS-TBA, and CAR (TPS-TfO) samples were measured.

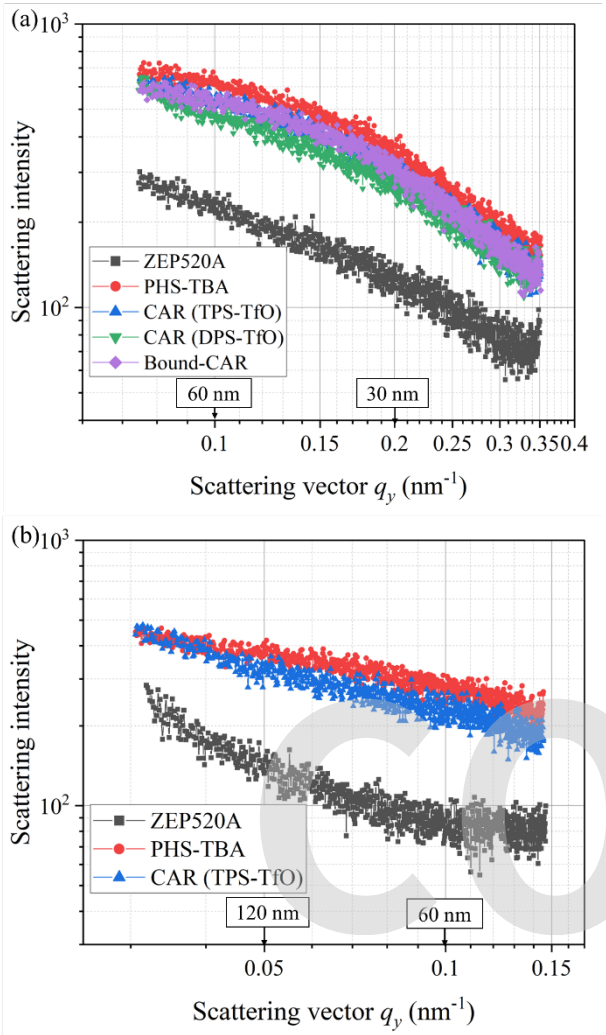

Fig. 5. Scattering intensity profiles of the resist with the camera length of (a) $x = 48$ mm, and (b) $x = 107$ mm at the photon energy of 280 eV.

To evaluate the scattering profile with wide q_y, Figs. of 5(a) and 5(b) are combined as shown in Fig. 6. Because the camera length in Fig. 5(b) is long, the intensity in Fig. 5(b) is lower than that in Fig. 5(a). Thus, the intensity of Fig. 5(b) is normalized to combine continuously to Fig. 5(a). The profile of ZEP520A was slightly discontinuous at the combined position around $q_y = 0.1$ nm^{-1} due to the background difference of the measurements. Fig. 6 shows the scattering profile with wide q_y region of 0.032–0.35 nm^{-1}.

The scattering intensity of ZEP520A was smaller than that of the other PHS-TBA-based samples, such as PHS-TBA, CARs, and bound-CAR. In addition, the scattering profile of ZEP520A had a straight shape, as shown in Fig. 6. This indicates that there were small aggregations in the ZEP520A thin film and it is the best sample in those 5 samples. In contrast, PHS-TBA and CAR(TPS-TfO) have large scattering signal and curved profile in Fig. 6. This indicates a large aggregation in this spatial frequency region. At this photon energy of 280 eV, the carbon was almost transparent, and the other components, such as oxygen, had a large absorption. This significant difference in aggregation between ZEP520A and other resists could be caused by differences in the chemical structure of hydroxyl groups in the base polymers.

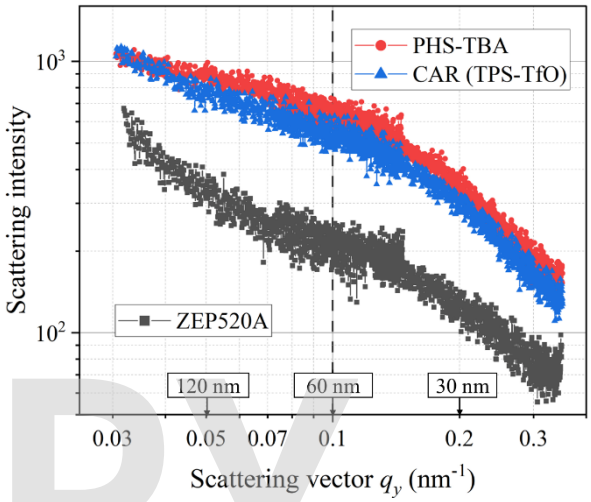

Fig. 6. Combined scattering profiles from Fig. 5(a) and 5(b).

In a comparison of the scattering intensities of PHS-TBA, CARs, and bound-CAR shown in Fig. 5(a), the scattering intensity of CARs was lower than that of PHS-TBA without PAGs. In other words, the presence of PAG in the PHS-TBA-based resist suppressed polymer chemical aggregation. In addition, the scattering intensity of CAR(DPS-TfO) is lower than that of CAR(TPS-TfO). DPS-TfO has a different chemical structure from TPS-TfO, which also has different polarities. The polarity of PAG could control the chemical aggregation of CAR.

4. Conclusion

In this study, the spatial distribution of chemical components of several resist thin films on Si wafers was evaluated using a reflection-mode RSoXS measurement system installed at BL-10 at the NewSUBARU synchrotron light facility. The scattering intensity profiles indicates the chemical aggregation. It was observed that the scattering intensity of ZEP520A was the lowest in five samples, and it is the best sample which has less aggregation. The difference in scattering intensity between the ZEP520A and PHS-TBA-based resists

suggests that the hydroxyl groups in the polymer structure affect the chemical aggregation. The scattering intensity of PHS-TBA was larger than that with PAGs. The chemical aggregation could be reduced by adding PAG. Then, it can be considered that the absence of polar group or the control the polarity is necessary for resist material development.

Reflection-mode RSoXS measured the chemical aggregation in the resist, which is helpful for resist development. In the future, we will measure the resist at another resonant absorption energy to evaluate differences in the aggregation of specific functional groups.

Acknowledgement

This work was partly supported by JSPS KAKENHI (grant number 21K14212).

References

1. A. Burov, A. V. Pret, R. Gronheid, *Proc. SPIE,* **12293** (2022) 122930V.
2. N. Maeda, A. Konda, K. Okamoto, T. Kozawa, and T. Tamura, *J Appl. Phys*., **59** (2020) 086501
3. M. Muramatsu, A. Hara, A. Shimura, and H. Yaegashi, *J. Photopolym. Sci. Technol*., **34** (2021) 55.
4. Y. Nakatani, T. Harada, A. Takano, M. Yamada, and T. Watanabe, *J. Photopolym. Sci. Technol*., **30** (2017) 77.
5. J. Tanaka, T. Ishiguro, T. Harada and T. Watanabe, *J. Photopolym. Sci. Technol.*, **32** (2019) 327.
6. J. Tanaka, T. Ishiguro, T. Harada and T. Watanabe, *J. Photopolym. Sci. Technol.*, **33** (2020) 491.
7. A. Nakamoto, S. Yamakawa, T. Harada, and T. Watanabe, *J. Photopolym. Sci. Technol.*, **35** (2022) 61.
8. C. Wang, D. H. Lee, A. Hexemer, M. I. Kim, W. Zhao, H. Hasegawa, H. Ade, and T. P. Russell, *Nano Lett.*, **11** (2011) 3906.
9. M. A. Ruderer, C. Wang, E. Schaible, A. Hexemer, T. Xu, and P. M-Buschbaum, *Macromolecules*, **46** (2013) 4491.
10. J. Wernecke, H. Okuda, H. Ogawa, F. Siewert, and M. Krumrey, *Macromolecules*, **47** (2014) 5719.
11. T. Pfadler, M. Coric, C. M. Palumbiny, A. C. Jakowetz, K.-P. Strunk, J. A. Dorman, P. Ehrenreich, C. Wang, A. Hexemer, R.-Q. Png, P. K. H. Ho, P. M.-Buschbaum, J. Weickert, and L. S.- Mende, *ACS Nano,* **8** (2014) 12397.
12. E. Gann, A. Watson, J. R. Tumbleston, J. Cochran, H. Yan, C. Wang, J. Seok, M. Chabinyc, and H. Ade, *Phys. Rev. B*, **90** (2014) 245421.
13. C. J. Schaffer, C. Wang, A. Hexemer, P. M.-Buschbaum, *Polymer.*, **105** (2016) 357.
14. F. Liu, M. A. Brady, C. Wang, *Eur. Polym. J.*, **81** (2016) 555.
15. W. Zhong, F. Liu, and C. Wang. *J. Phys*., **33** (2021) 313001.
16. M. Kuki, T. Uemura, M. Yamaguchi, T. Harada, T. Watanabe, Y. Muramatsu, and H. Kinoshita, *J. Photopolym. Sci. Technol.*, **28** (2015) 531.
17. T. Harada, N. Teranishi, T. Watanabe, Q. Zhou, J. Bogaerts, and X. wang, *Appl. Phys. Exp.*, **13** (2020) 103009.
18. S. Yamakawa, A. Yamamoto, S. Yasui, T. Watanabe, and T. Harada, *J. Photopolym. Sci. Techonl.*, **34** (2021) 111.
19. T. Ishiguro, J. Tanaka, T. Harada, and T. Watanabe, *J. Photopolym. Sci. Technol.*, **32** (2019) 333.
20. A. Duparre, J. Ferre-Borrull, S. Gliech, G. Notni, J. Steinert, and J. M. Bennett, *Applied Optics*., **41** (2002) 154.

Journal of Photopolymer Science and Technology
Volume 36, Number 1 (2023) 47 − 52 ©2023SPST

Characterization of Photoacid Generator Bound Resist with X-ray Absorption Spectroscopy at NewSUBARU

Shinji Yamakawa[1]*, Tetsuo Harada[1], Koji Nakanishi[2] and Takeo Watanabe[1]

[1] Center for EUV Lithography, Laboratory of Advanced Science and Technology for Industry, University of Hyogo, 1-1-2, Kouto, Kamigori, Ako-gun, Hyogo 678-1205, Japan
[2] Laboratory of Advanced Science and Technology for Industry, University of Hyogo, 1-1-2, Kouto, Kamigori, Ako-gun, Hyogo 678-1205, Japan
**s.ymkw@lasti.u-hyogo.ac.jp*

Post-synthesis or post-extreme ultraviolet (EUV)-exposure chemical analysis is necessary to develop resist materials on the next-generation EUV lithography. It is effective to use the X-ray analysis method for a resist coated on a Si wafer. In this paper, the photoacid generator (PAG) unit in the PAG bound type resist is analyzed by the X-ray absorption spectroscopy (XAS). As a result, the amount of anion species in PAG was estimated by sulfur K-edge (S K-edge) XAS spectrum. Further, the chemical structure of resist after the EUV irradiation was suggested by carbon K-edge (C K-edge) and sulfur L-edge (S L-edge) XAS spectra.
Keywords: EUV lithography, EUV resist, X-ray absorption spectroscopy (XAS), sulfur, PAG bound resist

1. Introduction

Since in the next-generation extreme ultraviolet (EUV) lithography, it is strongly required to develop EUV resist satisfied the high resolution, high sensitivity, and low line-width-roughness (LWR), simultaneously. The chemical analysis of EUV resist is significant in the EUV resist development. However, it is difficult to analyze using general solution analysis method such as the nuclear magnetic resonance (NMR) and liquid chromatography since the resist is coated on a Si wafer with a thickness of only a few tens nanometers. Therefore, the solid-state analysis methods such as the Fourier-transform infrared spectroscopy (FTIR) [1], secondary ion mass spectroscopy (SIMS) [2, 3], X-ray photoelectron spectroscopy (XPS) [1, 4-7], and X-ray absorption spectroscopy (XAS) [1, 4-5, 8-10] are used. In particular, the XAS measurement has the advantage of being able to perform element-selective analysis with relatively good resolution, and to investigate the chemical state of the material, such as the difference in the chemical bond and valence.

Our group has been reported the chemical analysis of the decomposed photoacid generator (PAG) by carbon K-edge (C K-edge) and fluorine K-edge (F K-edge) XAS spectroscopy [8-10]. Here, for sulfonium-based PAG, the XAS measurements of sulfur K-edge and L-edge (S K-edge and S L-edge) are also possible. However, the reports of the XAS analysis for sulfur atom in PAG is rare case. For example, the PAG bound resist having PAG in the polymer side chain is known to be effective in reducing LWR [11]. In addition, since PAG-bound resist can introduce PAG into the polymer side chain at a rate of several tens of percent, it is possible to increase the sensitivity. Therefore, the XAS analysis of the PAG bound resist will help develop resists with high sensitivity and low LWR.

In this paper, it is analyzed some PAG units in the PAG bound type resists by S K-edge, and S L-edge, and C K-edge XAS spectroscopy and discussed chemical structures, and chemical reaction scheme.

2. Experimental

2.1. Materials

Dimethylsulofoxide (DMSO)-d_6, sodium trifluoromethanesulfonate ($NaSO_3CF_3$) and

Received May 3, 2023
Accepted May 16, 2023

dimethyl acetoamide (DMAc), hexamethyldisilazane (HMDS), 2.38wt% tetramethylammonium hydroxide in aqueous solution ($TMAH_{aq.}$), poly(hydroxystyrene-*co-tert*-butylacrylate) (PHS-TBA) poly hydroxystyrene (PHS) were used as purchased. PAG was provided by San-Apro Ltd.

2.2. Measurements

NMR (^1H and $^{19}F\{^1H\}$) spectra were recorded on JEOL JNM-ECZ600R (600 MHz) spectrometer. The peaks were referenced to DMSO (δ2.50) in the DMSO-d_6 solvent for ^1H NMR. EUV Dose estimation was examined at NewSUBARU BL03 beamline [12]. S K-edge XAS spectroscopy was performed at NewSUBARU BL05 beamline [13]. C K-edge and S L-edge XAS spectroscopy was performed at NewSUBARU BL10 beamline [14, 15]. The XAS spectra were obatined with the partial fluoresence yield (PFY) using the silicon drift detector or total electron yield (TEY) by monitoring the sample drain current. The incident X-ray energy of S K-edge region was calibrated with the first main peak of K_2SO_4 at the photon-abstorption energy of 2481.7 eV [16]. The incident X-ray energy of C K-edge and S L-edge region was calibrated with the first main peak of resist-2 at the photon-absorption energy of 286 eV [17].

2.3. Preparation of resists

Resist 1a, 1b and **2** as shown in Fig. 1 were prepared according to the procedure in reference 18. However, as a salt exchange process, for **Resist 1b** and **2**, $NaSO_3CF_3$ 1 eq per PAG unit was added to mixture then stirred for 1 h at r.t. after the PAG bound resist synthesis process. Yield of **Resist 1b** and **2** were 85% and 75%, respectively. The signals and their positions are as follows: ^1H NMR: δ8.19-7.39 (PAG), 7.20-6.06 (phenyl) and 2.05-0.0 (alkyl); $^{19}F\{^1H\}$ NMR: δ-77.7 (CF_3).

The ration of the microstructure of the PHS unit and the degree of introduction (DI) of the PAG moiety in the polymer was calculated according to procedure in reference 18. The DI of PAG moiety of resist 1a, 1b, and 2 was 5.2, 5.5, 79 mol%, respectively.

2.4. Preparation of resist thin films by spin coating

Before the resist spin coating process, surface of Si wafers were HMDS treated to improving the adhesion of a resist coating. The spin-coating process was performed at 3000 rpm for 30 s to form HMDS adhesion treatment on silicon wafers. Then these spin-coated films were baked at 110 ºC for 90 s.

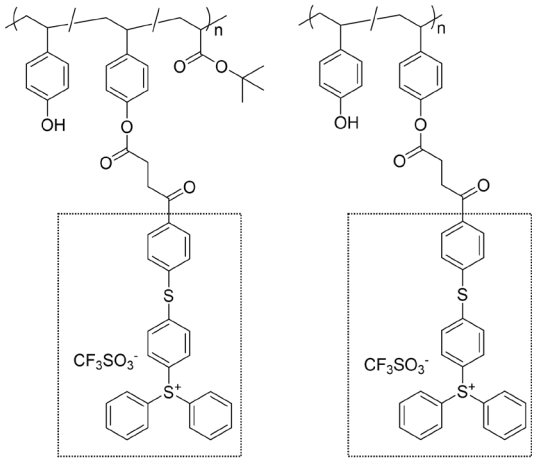

Fig. 1. The chemical structure of (a) resist 1 (1a and 1b) and (b) resist 2. Resist 1b and 2 were carried out the salt exchange process after the PAG bound resist synthesis process. The DI of PAG moiety of resist 1a, 1b and 2 was 5.2, 5.5, 79 mol%, respectively. The chemical structure in dashed box is PAG moiety.

The resist solutions in DMAc prepared were filtered through a 0.22 μm PTFE syringe filter prior to spin-coat on silicon wafers. All resist thin films were applied to the thickness of 40 nm on Si wafer at a spin-coating speed of 2500 rpm for 45 s and the PAB temperature at 130 ºC for 60 s. The resist thin film thickness was measured by the optical-interference-type film thickness measurement tool (NanoSpec6100, NANO metrics Inc.).

2.5. Developing and rinse technique

After the EUV exposure, all resist thin films were post-exposure baked at 110 ºC for 90 s and then cooled down to room temperature. Then, resists 1a and 1b were developed with 2.38 wt% TMAH aq. for 60 s and then rinsed with UPW for 30 s. Resist 2 was developed with 2.38 wt% TMAH aq. for 60 s and then rinsed with UPW for 30 s, or developed with butyl acetate for 240 s without rinsing.

3. Results and discussions

3.1. Dose estimation and XAS analysis for resist 1a and 1b

The dose estimation of resists 1a and 1b were evaluated from the sensitivity curves. Resist 1b was prepared to the salt exchange process after the synthesis process (as described in section 2.3). Resist thin films on Si wafer were exposed by EUV light while changing the exposure dose. After the development, rinse technique, and measuring the thickness of the residual resist thin film, sensitivity

curve can be obtained. Fig.2 shows the sensitivity curve of resists 1a (black square), and 1b (red circle). As a result, E_0 dose sensitivities of resists 1a and 1b showed 10 and 8 mJ/cm^2, respectively. To clarify these results, the XAS measurement was performed.

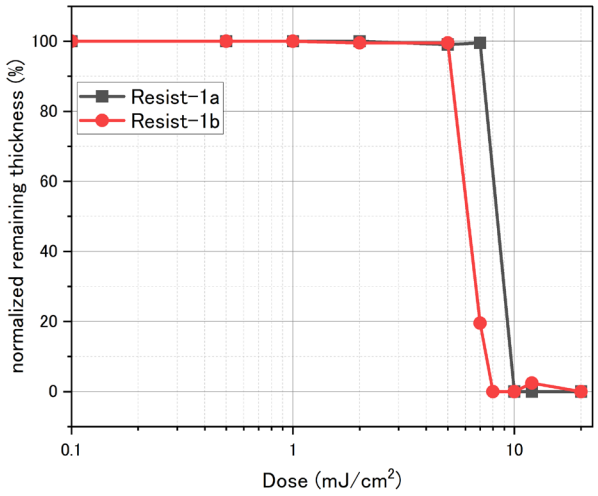

Fig. 2. Sensitivity curves of resists 1a (black square), and 1b (red circle).

XAS spectroscopy for resists 1a, and 1b was examined. Fig. 3 shows the S K-edge XAS spectrum of resist 1a (blue line) and peak fitting results. The edge jump was assumed at 2478.6 eV due to peak fit. Two peaks A, and B at 2474.4 and 2480.3 eV were assigned R-S-R', and RSO_3^- [19]. It is considered that R-S-R' and RSO_3^- is derived from diphenyl sulfide moiety and trifluoromethanesulfonate (TfO^-) ion species, respectively. The comparison of the peak area ratio of B/A with PFY or TEY for resists 1a, and 1b is summarized in Table 1. For both PFY and TEY

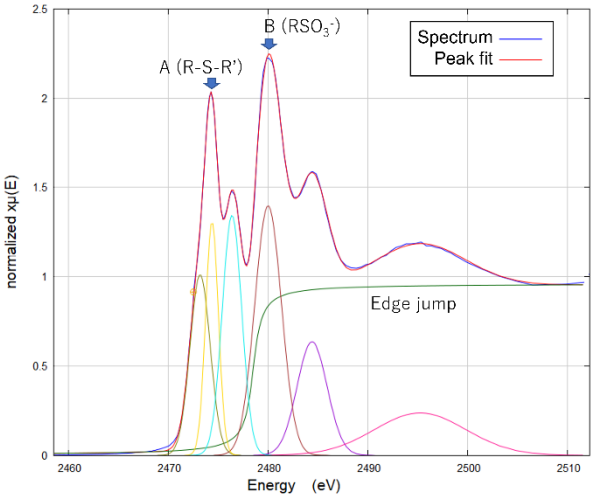

Fig. 3. S K-edge XAS spectrum and peak fitting results of resist-1a by PFY.

to be 1.16 or 1.06 times than that of resist 1a. These results, the peak area ratio of resist 1b was estimated results mean that the amount of TfO^- ion moiety in resist 1b was higher than resist 1a. Thus, the TfO^- ion moiety in resist 1b increased by the salt exchange process. Taken together with the result of dose estimation, it was guessed that the anion species was exchanged weaker anion species during the resist synthesis process. Hence, E_0 of resist 1a was lower than that of resist 1b due to the slow decomposition of dissolution inhibiting groups. It is suggested that performing a salt exchange process after the synthesis process is useful for synthesizing a high-purity resist.

Table 1. Peak area ratio of resist 1a and 1b

	Peak area ratio of fitting peak B/A	
	Resist-1a	Resist-1b
PFY	1.45	1.69
TEY	1.60	1.71

3.2. Dose estimation and XAS analysis for resist 2

The dose estimation of resists 2 was evaluated from the sensitivity curves as shown Fig.3. In the case of using TMAH aq. as developer, the 40% thickness loss of resist film was occurred. However, remaining thickness was showed 94% at 50 mJ/cm^2 in the exposed area (black square in Fig. 2), resist 2 was behaved as a negative-tone resist. In contrast, when butyl acetate was used as a developer, the film thickness loss did not occur, and the remaining thickness was showed 86% at 50 mJ/cm^2 in the exposed area (red circle in Fig. 2). To understand this development behavior, C K-edge, and S L-edge XAS measurements were performed.

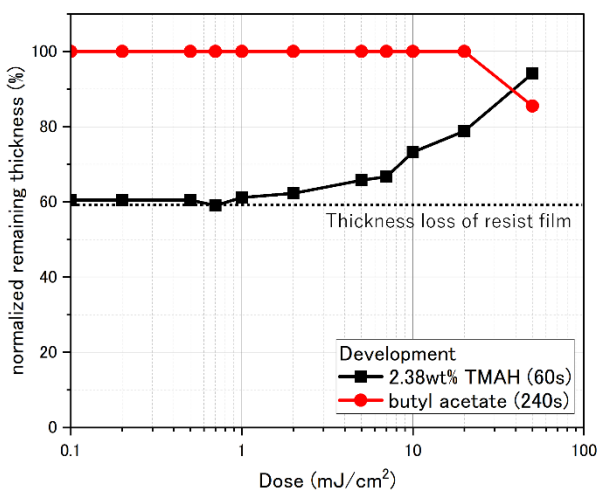

Fig. 4. Sensitivity curve of resist 2 developed 2.38wt% TMAH aq. (black square), and butyl acetate (red circle).

Fig. 5 shows C K-edge XAS spectra of resist 2 before (black square) and after (red circle) EUV irradiation by TEY. As samples before and after EUV irradiation, powder resist 2 and a resist thin film after coating and developing with 2.38 wt% TMAH aq. on a Si substrate were used, respectively. The absorption peaks of 286.0, 289.4, 294.3 and 295.4 eV were assigned to π*(C=C), π*(C=O), σ*(C-C), and σ*(C-F) bonding, respectively [8-9].

The peak intensity derived from σ*(C-F) was decreased after EUV irradiation. It is considered that the TfO^- ion moiety dissolved in the developer due to the decompose PAG unit. However, it was unclear that the changes in the chemical structure of the cationic species in PAG. Thus, S L-edge XAS spectroscopy was performed by the same samples. Fig. 6 shows S L-edge XAS spectra of resist 2 before (black square) and after (red circle) EUV

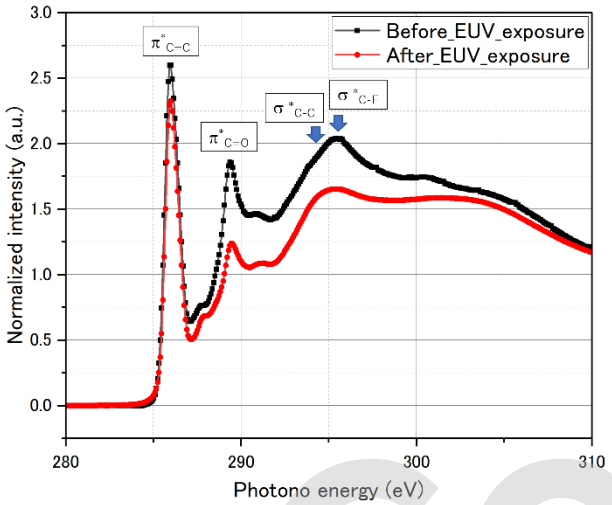

Fig. 5. C K-edge XAS spectra of resist 2 before (black square) and after (red circle) EUV exposure.

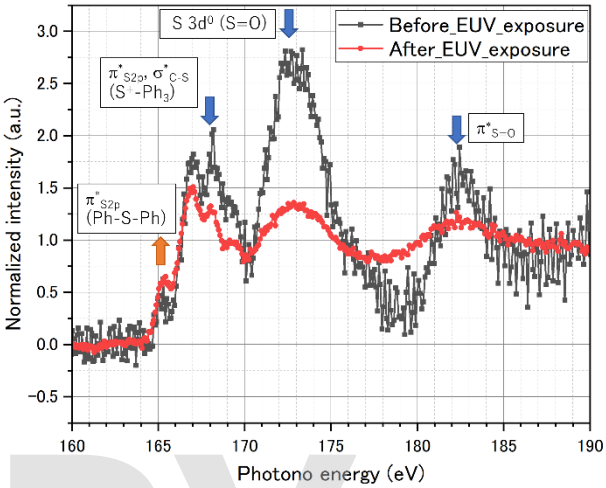

Fig. 6. S L-edge XAS spectra of resist-2 before (black square) and after (red circle) EUV exposure.

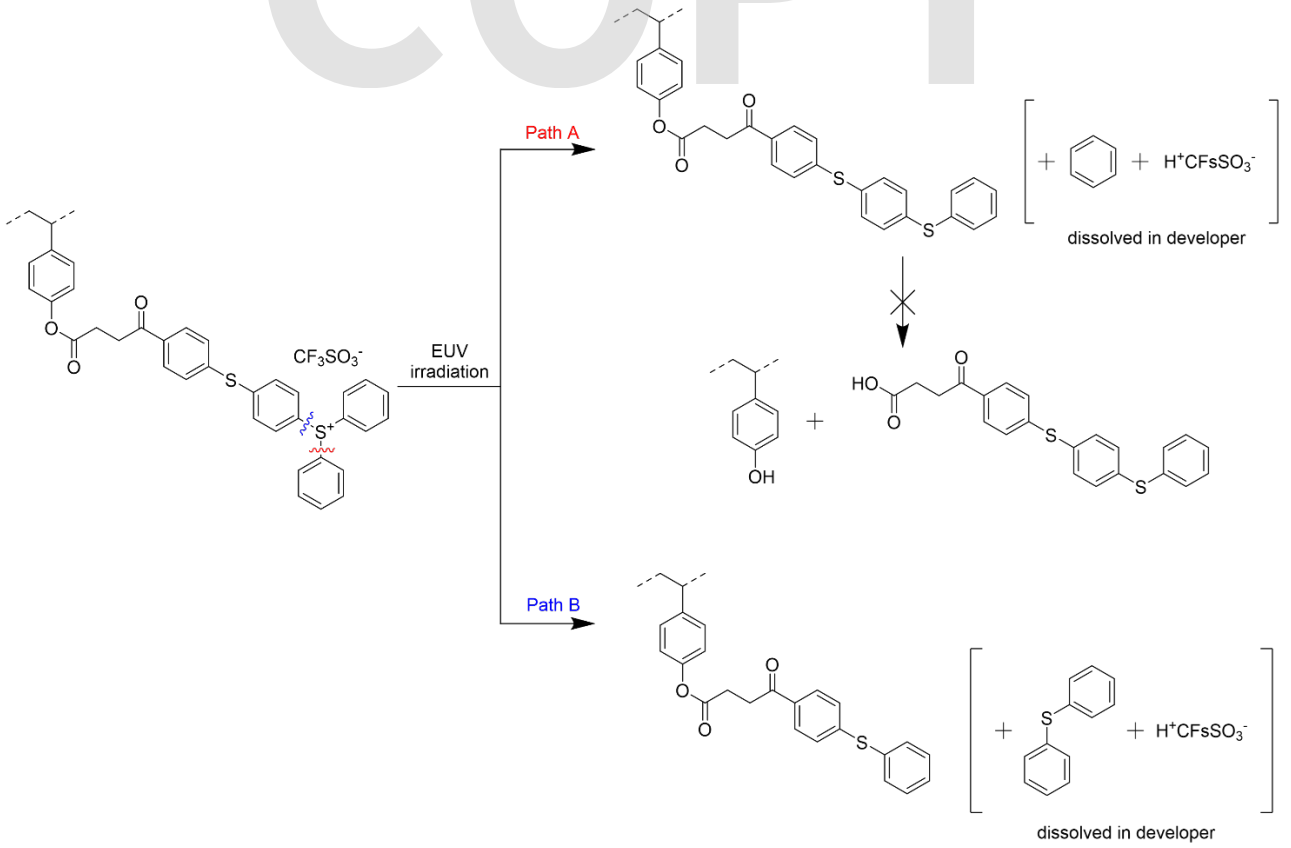

Scheme 1. Proposed decomposition reaction mechanism of resist 2 after EUV irradiation.

irradiation by TEY. The absorption peaks of 165.3, 168.1, 172.8, and 182.4 eV were assigned to π*(S 2p), π*(S 2p) or σ*(C-S), S $3d^0$ and π*(S=O) bonding, respectively [20-21]. As a result, the peak intensity of π*(S 2p) derived from diphenyl sulfide moiety in PAG increased after EUV irradiation. However, the peak intensity of π*(S 2p) or σ*(C-S) derived from triphenyl sulfonium cation and S $3d^0$ and π*(S=O) corresponding to TfO^- ion moiety decreased after EUV irradiation. The possible reaction mechanism after EUV irradiation is shown in Scheme 1. If the ester bond connected main chain to side chain was decomposed by acid generated from PAG, the PAG moiety would dissolve in the developer and the XAS peak intensity derived from PAG should decrease overall. However, the peak intensity corresponding to diphenyl sulfide moiety (165.3 eV) did not decrease, indicating that the PAG moiety remained after the alkaline development That is, it is suggested that the ester decomposition reaction did not occur. Additionally, the decomposition mechanism of PAG unit is thought to be paths A and B. However, since there is no decrease in the peak intensity derived from diphenyl sulfide moiety, path A is presumed to be the major path. Therefore, it was strongly suggested that the resist 2 after EUV irradiation has phenyl sulfide group at the side chain.

The development behavior is considered based on the above discussion. The resist 2 is relatively hydrophilic because it has an ionic PAG before EUV irradiation. However, after EUV irradiation, PAG unit in resist 2 side chain decomposes, and the resist 2 becomes hydrophobicity. Therefore, it is considered that they exhibited as negative-tone-development behavior in the alkaline developer, and as positive-tone-development behavior in organic developer.

4. Conclusion

In this study, it is analyzed PAG unit in PAG bound type resist by S L-edge and K-edge, and C K-edge XAS spectroscopy. Comparison of S K-edge XAS spectra of resists 1a and 1b were suggested to the salt exchange process was effective for the synthesis high-purity resist. Further, before and after EUV irradiation, resist 2 was analyzed by C K-edge and S L-edge XAS spectroscopy and discussed the decomposition mechanism of PAG moiety. We believe that the XAS spectroscopy of sulfur atom in PAG will help in the development of an EUV resist with high sensitivity and low LWR.

Acknowledgement

This work was partly supported by JSPS KAKENHI (grant number 21K14212).

References

1. N. Thakur, M. Vockenhuber, Y. Ekinci, B. Watts, A. Giglia, N. Mahne, S. Nannarone, S. Castellanos, and A. M. Brouwer, *ACS Matter. Au*, **2** (2022) 343.
2. N. Man, A. Sekiguchi, and Y. Matsumoto, *Proc. of SPIE*, **9425** (2015) 94251H-1.
3. X. Hou, M. Li, M. J. Eller, S. V. Verkhoturov, E. A. Schweikert, and P. Trefonas, *J. Micro/Nanolith. MEMS MOEMS*, **18** (2019) 033502.
4. V. S. V. Satyanarayana, F. Kessler, V. Singh, F. R. Scheffer, D. E. Weibel, S. Ghosh, and K. E. Gonsalves, *ACS appl. Mater. Interfaces*, **6** (2014) 4223.
5. C. Singh, V. S. V. Satyanarayana, N. Batina, I. M. Reyes, S. K. Sharma, F. Kessler, F. R. Scheffer, D. E. Weibel, S. Ghosh, K. E. Gonsalves, *J. Micro/Nanolith. MEMS MOEMS*, **13** (2014) 043002.
6. Z. Wang, J. Chen, T. Yu, Y. Zeng, X. Guo, S. Wang, T. Allenet, M. Vockenhuber, Y. Ekinci, G. Yang, and Y. Li, *ACS appl. Mater. Interfaces*, **15** (2023) 2289.
7. Q. Everard, N. Sadegh, Y. Ekinci, M. Vockenhuber, N. Mahne, A. Giglia, S. Nannarone, T. Goya, T. Sugioka, and A. M. Brouwer, *J. Photopolym. Sci. Technol.*, **35** (2022) 95.
8. T. Watanabe, Y. Haruyama, D. Shiono, K. Emura, T. Urayama, T. Harada, and H. Kinoshita, *J. Photopolym. Sci. Technol.*, **25** (2012) 569.
9. T. Wanatabe, K. Emura, D. Shiono, Y. Haruyama, Y. Muramatsu, K. Ohmori, K. Sato, T. Harada, and H. Kinoshita, *J. Photopolym. Sci. Technol.*, **26** (2013) 635.
10. K. Emura, T. Watanabe, M. Yamaguchi, H. Tanino, T. Fukui, D. Shiono, Y. Haruyama, Y. Muramatsu, K. Ohmori, K. Sato, T. Harada, and H. Kinoshita, *J. Photopolym. Sci. Technol.*, **27** (2014) 631.
11. T. Watanabe, Y. Fukushima, H. Shiotani, M. Hayakawa, S. Ogi, Y. Endo, T. Yamanaka, S. Yusa, and H. Kinoshita, *J. Photopolym. Sci. Technol.*, **19** (2006) 521.
12. T. Watanabe, H. Kinoshita, N. Sakaya, T. Shoki, and S. Y. Lee, *Jpn. J. Appl. Phys.* **44** (2005) 5556.

13. K. Nakanishi, *LASTI Annual Report*, **23** (2021) 27.
14. M. Kuki, T. Uemura, M. Yamaguchi, T. Harada, T. Watanabe, Y. Muramatsu, and H. Kinoshita, *J. Photopolym. Sci. Technol.*, **28** (2015) 531.
15. T. Fujii, S. Yamakawa, T. Harada, and T. Watanabe, *Proc. SPIE*, **11908**, (2021), 119080T.
16. K. Takemoto, D. Bamba, M. Ogawa, and T. Ohta, *J. Water Environ. Technol*., **14** (2016) 82.
17. A, Nakamoto, S. Yamakawa, T. Harada, and T. Watanabe, *J. Photopolym. Sci. Technol.*, **35** (2022) 61.
18. S. Yamakawa, A. Yamamoto, S. Yasui, T. Watanabe, and T. Harada, *J. Photopolym. Sci. Technol.*, **34** (2021) 111.
19. I. J. Pickering, R. C. Prince, T. Divers, G. N. George, *FEBS Lett.*, **441**, (1998), 11.
20. E. Cortés, C. O. D. Védova, M. Geronés, R. M. Romano, and M. F. Erben, *J. Phys. Chem. A*, **113** (2009) 9624.
21. K. E. Gonsalves, and D. E. Weibel, *RSC Adv*., **8** (2018) 10930.

Journal of Photopolymer Science and Technology
Volume 36, Number 1 (2023) 53 − 59 ©2023SPST

Present Status of EUV Interference Lithography at NewSUBARU

Rikuya Imai[1], Shinji Yamakawa[1]*, Tetsuo Harada[1], Takeo Watanabe[1]

[1]Center for EUV Lithography, Laboratory of Advanced Science and Technology for Industry, University of Hyogo
1-1-2 NewSUBARU, Kouto, Kamigori, Ako-gun, Hyogo, 678-1205, Japan
**s.ymkw@lasti.u-hyogo.ac.jp*

Since 2019, EUV lithography with a wavelength of 13.5 nm has been used for the mass production of 7 nm+ node semiconductor logic devices, and pattern processing of 16-nm-half pitch and below is also possible. According to IRDS, further miniaturization is still required by 2037. In EUVL, the most important issue is the development of resists with high sensitivity, high resolution, and low line-width roughness, simultaneously. At the NewSUBARU synchrotron light facility, the exposure tool on EUV interference lithography was developed to replicate EUV resist patterns, which can evaluate the resolution and line-width roughness performance. In this study, it is reported that the current results and status of this tool, especially on the improvement of the exposure shot numbers with a new grating holder and exposure-process automation by developing specific software program. As a result, the exposure shot numbers were improved to 48 shots, which were more than three times larger than those of the previous condition.
Keywords: EUV lithography, EUV resist, EUV interference lithography

1. Introduction

Since 2019, EUV lithography with a wavelength of 13.5 nm has been used for the mass production of 7-nm + node semiconductor logic devices, and has a resist patterning scalability of 16-nm-half pitch and below is also possible. However, the EUV technical issues are still remain for further miniaturization. The most important issue is the development of EUV resists with high sensitivity, high resolution, and low line-width roughness (LWR), simultaneously [1]. There is a trade-off between the resolution, sensitivity, and LWR. Therefore, it is difficult to develop an EUV resist which satisfies their requirements.

In order to evaluate the patterning performance of EUV resists, it is necessary to pattern the resist using the actual EUV exposure tool. The exposure tools such as ASML exposure tools and micro exposure tools that use masks and exposure optics complicated to be design owing to the complexity of the optical system [2]. In contrast, EUV interference lithography (EUV-IL) is simple because the resist pattern is replicated as the EUV interference fringes, and since it does not need EUV mask and optics, the patterned EUV resist do not affected by mask errors and optical aberration. Therefore, the EUV-IL exposure tools have been constructed at the end station of the beamline of the synchrotron light facilities worldwide and are widely used for resist evaluation [3]. The two-window interference lithography using the transmission grating usually is used, which does not require temporal coherence. This method is suitable for the undulator insertion light source of synchrotron without using a monochromator. For example, there are EUV-IL tools in the Swiss Light source of synchrotron without using a monochromator. For example, there are EUV-IL tools in the Swiss Light Source [4], Shanghai Synchrotron Radiation Facility in the world [5].

In Japan, the EUV-IL exposure tool was developed at BL09b beamline at NewSUBARU synchrotron light facility, which was used for the EUV patterning tool to evaluate resist

Received May 5, 2023
Accepted May 12, 2023

performance [6–12]. In this study, it is reported that the current results and status of this EUV-IL tool, especially the improvements in the exposure shot number increase by improving the grating holder design and exposure process automation by developing the specific software program.

2. Experimental

2.1. Principle of EUV-IL

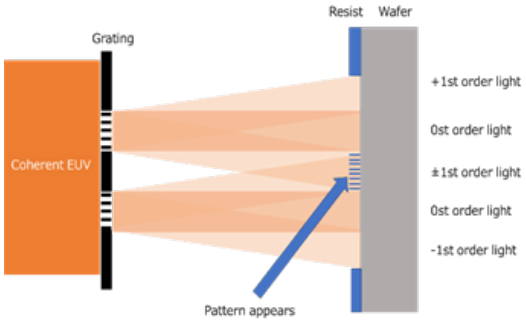

Fig. 1. Principle of EUV-IL patterning on EUV interference lithography based on the two-window-transmission grating. The diffracted light from the transmission gratings and the fringes were generated on the resist coated on a wafer to form the resist pattern.

Fig. 1 shows the principle of EUV-IL patterning. The 1st harmonics from the long undulator of the BL09 beamline was employed as a EUV light for the EUV-IL tool. This undulator light was tuned to EUV light which has a wavelength of 13.5 nm with the undulator gap of 36.5 mm at the electron-beam energy of 0.95 GeV of the storage ring at NewSUBARU. This EUV light was not enough to monochromatized for the EUV interference lithography by the BL09-beamline monochromator, which is 0th order diffraction from the monochromator grating. At 3.3 m upstream of that EUV-IL grating, the EUV was focused on the exitance slit with 25-μm width. Spatially the coherent length was approximately 0.57 mm at the EUV-IL grating position. The spatially coherent EUV exposes the EUV-IL grating which is a two-window transmission-type diffraction grating. An interference line fringe is generated at the overlap position of the +1st-order and -1st -order diffracted light as shown in Fig. 1. A silicon wafer coated with a sample resist was set to this overlap position, and the line-and-space resist pattern is replicated on a wafer by this interference fringes. The line and space pattern pitches are a half pitches of the diffraction grating [13].

2.2. EUV-IL grating

The diffraction grating was fabricated by NTT-AT Corp. The grating-support membrane consisted of 200-nm-thick SiC and 50-nm-thick Si_3N_4. SiC membrane is very strong in terms of both X-ray radiation and mechanical stress. The patterned-absorber material was Ta, with a thickness of 30 nm. The calculated diffraction efficiency is 1.39% which is enough sufficient for the EUV interference lithography at the BL09b beamline. Fig. 2(a) shows the schematic layout of the grating pattern regions. There were six line-and-space-pattern region pairs with the half-pitches of 100, 60, 50, 40, 35, and 30 nm. The size of the patterned region was 100 × 50 μm^2. The patterning size of the EUV fringe on the resist is 1/2 of these line-and-space-pattern sizes, which were the half pitches of 50, 30, 25, 20, 17.5, and 15 nm. The distance between these grating region pairs was varied to overlap the pattern area at the wafer position. The design distance between the grating and wafer was approximately 1 mm. Fig. 2(b) shows an optical microscope image of an exposed region on the EUV resist coated on a silicon wafer. The six pattern areas were replicated on a wafer aligned at the center position of the grating.

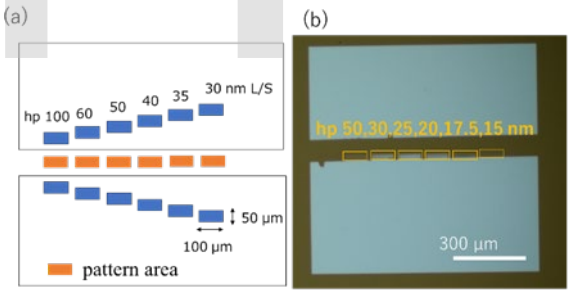

Fig. 2. (a) Schematic layout of the EUV-IL grating region and (b) an optical microscope image of the exposed region on the resist.

2.3. Grating holder

A schematic side view of the diffraction grating, wafer, and grating holder in EUV exposure is shown in Fig. 3. A center stop was placed on the front side of the grating holder to prevent straight EUV light transmission at the center of the grating layout. The residual straight EUV transmission would reduce the interference contrast of the diffraction grating pairs. In this study, a tungsten wire with a diameter of 100 μm was used as the center stop. The wire position was adjusted to the center of the pattern region pairs. Fig. 4 shows an optical microscope image

of the wire and patterning regions. This image is a composite image with two images focused on the wire and patterning region. The wire was well aligned to the center of the pattern regions. As shown in Fig. 2(b), since the wire stopped the straight EUV perfectly, the diffracted EUV at the wire was not observed in the exposed regions.

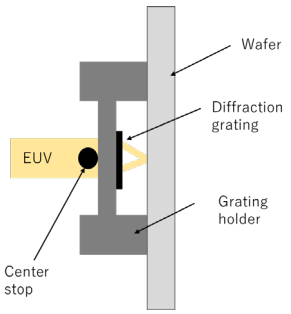

Fig. 3. Schematic view of the EUV exposure setup of grating holder and wafer in EUV interference.

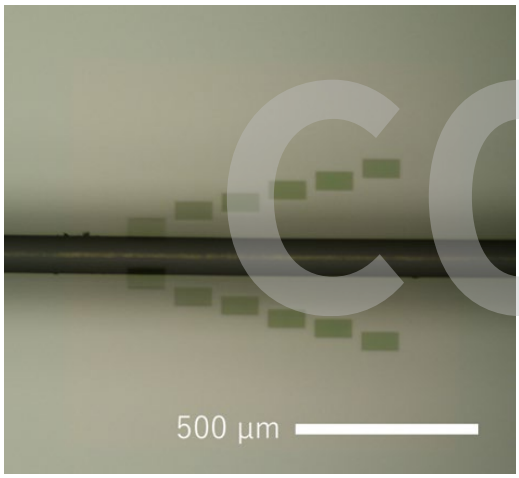

Fig. 4. Optical microscope image of the wire center stop and grating regions.

Since during the EUV exposure, the grating holder is contacted to the wafer to reduce the relative vibration between the grating and the wafer as shown in Fig. 3, the region in contact with the holder was damaged. It is necessary to avoid overlapping of the contacted and patterned regions, which limits the exposure layout on a wafer. A photograph of the conventional grating holder and expected exposure area are shown in Fig. 5(a) and (b), respectively. The holder has a clear aperture with a diameter of 40 mm, and the contact area of a wafer with the grating holder surface is shown with a dotted line. Since the shape of the contact area is circular, the exposure range is limited to 15 × 15 mm^2. In this case, the maximum number of exposure shots per wafer is approximately 15. However, more exposure shots were required for the resist evaluation.

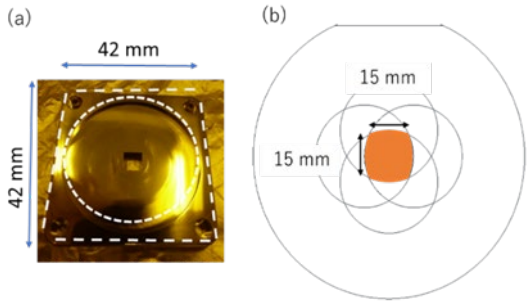

Fig. 5. (a) Photograph of the conventional grating holder, and (b) schematic image of the exposure area with this grating holder.

2.4. Exposure process

Fig. 6 shows a schematic view of the shutter and exposure chamber, and the exposure process is listed below. The definition of the stage axes direction is shown in the right-down part with *x*, *y* and *z* arrows. The wafer position to the grating is controlled by *y*- and *z*-stages. The distance between the grating and the wafer is controlled by the *x*-stage.

1. The wafer *x*- and *y*-stages are controlled to the exposure position.
2. The wafer *x*-stage is controlled to the contact position with the grating stage to suppress the vibration.
3. All the motor driver of the stages are turned off. After the turned off, 60 s waiting time is needed to suppress the vibration.
4. The exposure shutter is opened, and exposure time is controlled.
5. The wafer *x*-stage is moved away from the diffraction grating holder.
6. The above exposure processes from 1 to 5 are repeated to complete the required number of shots.

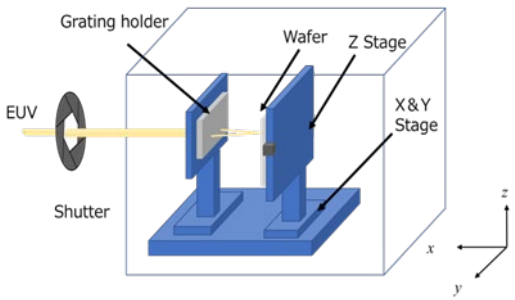

Fig. 6. Schematic view of EUV-IL with the grating holder, wafer *x*-, *y*-, and *z*-stages, and exposure shutter.

In the previous study, there were some mistakes to control the exposure stage positions and exposure times in manually. In this study, it is developed exposure software program that enables batch processing of exposures by entering exposure recipes. This type of automation is very important for reliable exposures.

The waiting time for the vibration suppression is crucial to obtain fine pattern. The scanning electron microscopy (SEM) images of EUV-IL replicated patterns with the different waiting times are shown in Fig. 7. The critical-dimension SEM (CD-SEM) of S8840 (Hitachi High-Tech) was used for the resist pattern observations in top view. The acceleration voltage was set at 800 V. The resists were coated with PtPd alloy by an ion coater.

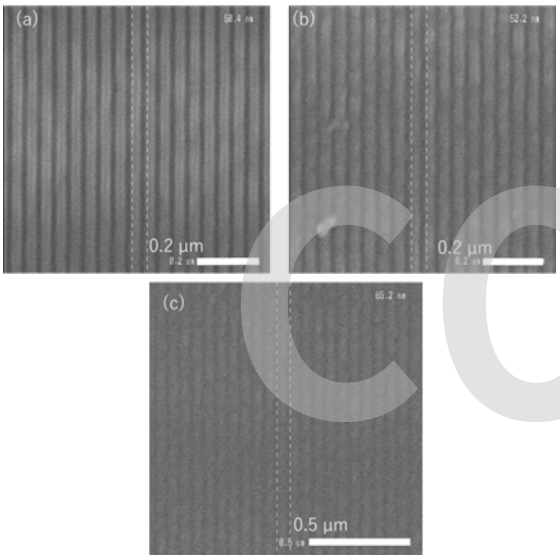

Fig. 7. CD-SEM image of line patterns with the pattern sizes (half pitches) and waiting times of (a) 25 nm, 60 s (b) 25 nm, 30 s, and (c) 30 nm, 10 s.

Fig. 7(a) and (b) show line patterns of 25 nm in half pitch with waiting times of 60 and 30 s, respectively. Fig. 7(c) shows a line pattern SEM -top-view-image of 30 nm in half pitch with waiting time of 10 s. The line pattern of 25 nm in half pitch is clearly resolved in Fig. 7(a) with that of 60 s. However, it was slightly blurred in Fig. 7(b) with that of 30 s. With a waiting time of 10 s, the line pattern with the same 25 nm half pitch was not resolved. The CD-SEM image with that of 30 nm was much blurred in Fig. 7(c) Therefore, the waiting time was set to 60 s in this study, which was much longer than the exposure time and stage-moving time. The typical exposure time was several tens of seconds, and the stage-moving time was approximately 10 s per shot. Thus, this waiting time was the dominant time in the EUV-IL exposure.

3. Results and Discussion

3.1. Novel grating holder

A novel grating holder was introduced, which is shown in Fig. 8(a). This novel grating holder has four square regions to contact the wafer, which is not a circular shape such as the previous holder. The exposure possible area on a wafer was expanded as shown in Fig. 8(b). The length of the exposure possible area is extended to be 64 mm, which is limited by the *y*-stage stroke. The exposure possible area size was more than three times larger than that with the previous holder.

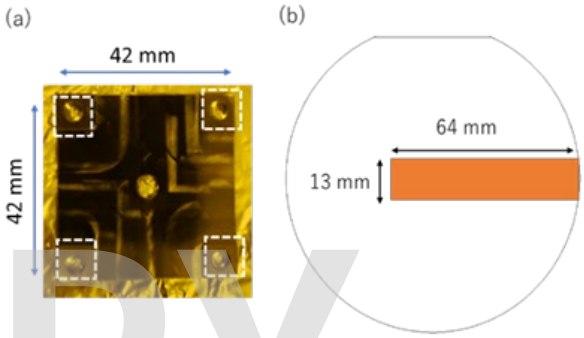

Fig. 8. (a) Photograph of the novel grating holder, and (b) schematic view of the extended exposure area.

3.2. Exposure results

The sample resist ZEP520A (ZEON) was spin-coated on a 4-inches-silicon wafer. The resist film thickness was 50 nm. The pre-baking temperature and its time period were 180 °C and 180 s, respectively. The developer and rinse solution were hexyl acetate and 2-propanol, respectively. Both of the dip development and dip rinsing times were 30 s of each.

Number of the exposure shots on this wafer were 48, which was more than three times larger than that with previous holder. A photograph of the exposed area after the development process is shown in Fig. 9. The white regions represent the exposed areas. There were orderly aligned 3 × 16 shots without any mistakes of the exposure positioning.

Fig. 10 shows the CD-SEM images of the replicated resist patterns in top views. The exposure-time periods were varied at (a) 11.50 s, (b) 11.75 s, (c) 12.00 s, and (d) 12.25 s. The interval of the exposure time period was 0.25 s. There are partially unresolved areas in (a) 11.5 s and (d) 12.25 s.

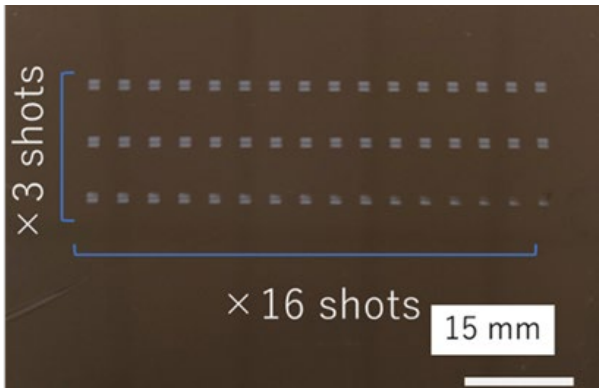

Fig. 9. Photograph of the exposed wafer with the 48 shots.

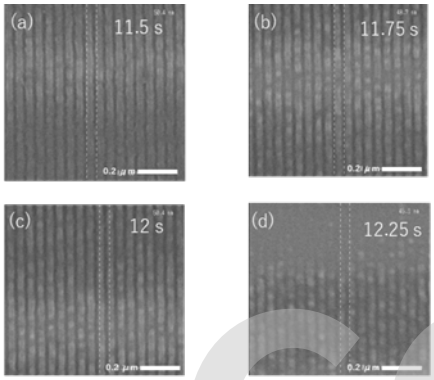

Fig. 10. CD-SEM images of line patterns of 25 nm half pitch with the exposure time of (a) 11.50 s, (b) 11.75 s, (c) 12.00 s, and (d) 12.25 s.

Under this development condition, the dose margin of the exposure time was not wide from (b) 11.75 to (c) 12.00 s, where the pattern was resolved. The resist with narrow dose margin such as this condition requires many exposure shots to evaluate best exposure dose for patterning.

3.3. Developer comparison

The line patterns in Fig. 10 with the hexyl acetate developer were not clearly resolved. It is attempted to use other developers such as *o*-xylene and butyl acetate. Fig.11 shows CD-SEM images of line patterns of 25 nm half pitch with three types of developers: (a)hexyl acetate, (b)*o*-xylene, and (c)butyl acetate. The dip development-time periods in Fig. 11(a), 11(b), and 11(c) were 30 s, 30 s, and 60 s, respectively. The dip rinse solution was 2-propanol for (a) and (b), with rinse-time period of 30 s. For the rinse process of (c), the resist-coated wafer was dried by N_2 gas shower. The exposure dose under EUV-IL was optimized. Since the best exposure doses of (b) and (c) were lower than that of (a), which were 70% and 25% of (a), respectively, the sensitivity of the ZEP520A resist strongly depended on the developer.

The patterns of Figs. 11(a) and 11(c) were not clearly resolved, and. that of Fig. 11(b) with the *o*-xylene developer was clearly resolved. The patterning resolution also depended on the developer solution.

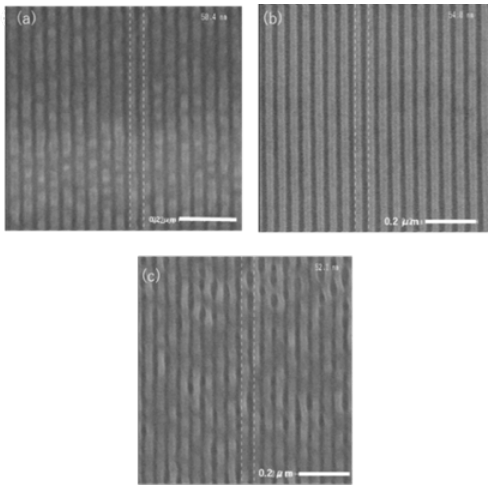

Fig. 11. CD-SEM images of the resist pattern developed with (a) hexyl acetate, (b) *o*-xylene, and (c) butyl acetate.

To evaluate the resolution of ZEP520A with the *o*-xylene developer, CD-SEM images with three-line-pattern sizes of (a) 30, (b) 25, and (c) 20 nm half pitches are shown in Fig. 12. The line patterns of (a) and (b) have good contrast. However, the pattern of (c) has low contrast. On the same wafer, there were exposed regions with smaller size of 17.5 nm and 15 nm, which were not resolved. Thus, the resolution limit of ZEP520A under this development condition was estimated to be 20 nm in half-pitch size.

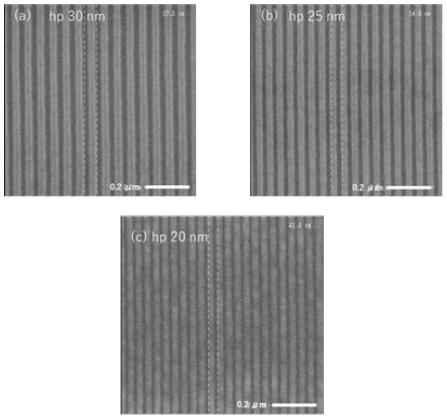

Fig. 12. CD-SEM images of the resist line patterns with (a) 30 nm, (b) 25 nm, and (c) 20 nm half pitch.

3.4. Cross-sectional SEM (CS-SEM) sample

The CS-SEM observations are typically used to evaluate the cross-sectional resist-pattern quality. To observe the CS-SEM image, the Si wafer should be cut in the patterned region. On the other hand, in the case of manual cutting, the position accuracy of the wafer cutting was approximately 500 µm. Therefore, the length of the pattern region should be longer than 500 µm. However, the length of the pattern region of the current grating (Fig. 2) was 100 µm. Thus, a novel exposure-shot layout shown in Fig. 13 was applied to the EUV-IL exposure, where the interval of the exposure position was 100 µm.

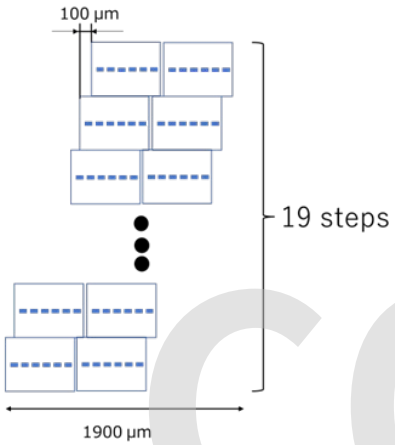

Fig. 13. Schematic designed layout of the exposure-shot positions for CS-SEM observations.

Fig. 14 shows a photograph of the patterned region with 38 exposure shots. The required position accuracy was less than 1.9 mm in this layout, which made it easy to cut the patterned region for the pattern observation with the CS-SEM.

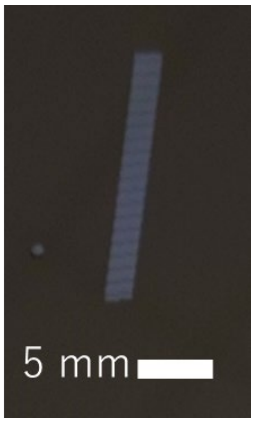

Fig. 14. Photograph of the exposure area on the wafer with the designed layout of the exposure shots shown in Fig. 13.

Then this wafer was cut into the patterned region successfully. Fig. 15 shows optical microscope images of the cutting edge of this wafer. The pattern sizes were (a) 30 nm, (b) 25 nm, and (c) 20 nm in half pitches in size. The patterned regions of all pattern sizes were well cut, which could be observed by the CS-SEM. Therefore, this shot layout was effective for the CS-SEM observations.

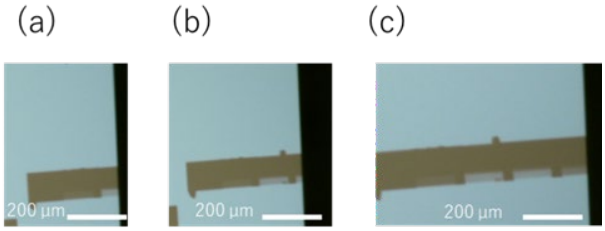

Fig. 15. Optical microscope images of the wafer cutting edges at the pattern regions of (a) 30 nm, (b) 25 nm, and (c) 20 nm.

4. Summary

For EUV resist evaluation of the resolution, LWR, and resist process, since it is necessary to evaluate the EUV replicated pattern, it should be developed the EUV-IL exposure tool at the BL09b beamline at NewSUBARU synchrotron light facility. In this study, we introduced the novel grating holder and exposure-process-controlled by the software program to increase the number of the exposure shots. As a results, the number of exposure shots on the wafer can be achieved to be 48, which was more than three times larger than that of previously reported.

The ZEP520A resist was evaluated for the resolution and development process. The exposure dose margin was optimized with a small dose step, and three developers were evaluated to achieve a high-contrast pattern. As a result, the pattern with the developer of *o*-xylene had the highest pattern contrast, and the resolution limit was 20 nm in half pitch in this study. The exposure layout for the CS-SEM observation was performed, and the pattern regions were cut well on the wafer edge.

Consequently, the increase of the number of the exposure shot made it possible to optimize the resist patterning condition to achieve high resolution in EUV-IL, which is crucial for EUV resist performance evaluation.

Acknowledgement

This work was partly supported by JSPS KAKENHI (grant number 21K14212).

References

1. D. V. Steenwinckel, J. H. Lammers, L. H. A. Leunissen, and J. A. J. M. Kwinten, *Proc. SPIE*, **5753** (2005) 269.
2. C. Anderson, A. Allezy, W. Chao, L. Conley, C. Cork, W. Cork, R. Delano, J. DePonte, M. Dickinson, G. Gaines, J. Gamsby, E. Gullikson, G. Jones, L. McQuade, R. Miyakawa, P. Naulleau, S. Rekawa, F. Salmassi, B. Vollmer, D. Zehm, W. Zhu, *Proc. SPIE*, **11323** (2020) 113230B.
3. T. Allenet, M. Vockenhuber, C-K. Yeh, D. Kazazis, J. G. Santaclara, L. van Lent-Protasova, and Y. Ekinci, *Proc. SPIE*, **11854** (2021) 118540N.
4. E. Buitrago, R. Fallica, D. Fan, W. Karim, M. Vockenhuber, J. A. van Bokhoven, and Y. Ekinci, *Proc. SPIE*., **9926** (2016) 99260T.
5. J. Zhao, S. Yang, C. Xue, L. Wang, Z. Liang, L. Zhang, Y. Wang, Y. Wu, and R. Tai, *Int. J. Extrem. Manuf.*, **2** (2020) 012005.
6. S. Suzuki, Y. Fukushima, R. Ohnishi, T. Watanabe, and H. Kinoshita, *J. Photopolym. Sci. Technol.,* **21** (2008) 435.
7. Y. Fukushima, Y. Yamaguchi, T. Kimura, T. Iguchi, T. Harada, T. Watanabe, and H. Kinoshita, *J. Photopolym. Sci. Technol*., **23** (2010) 673.
8. Y. Yamaguchi, Y. Fukushima, T. Iguchi, H. Kinoshita, T, Harada, and T. Watanabe *J. Photopolym. Sci. Technol.,* **23** (2010) 681.
9. T. Urayama, T. Watanabe, Y. Yamaguchi, N. Matsuda, Y. Fukushima, T. Iguchi, T. Harada, and H. Kinoshita. *J. Photopolym. Sci. Technol.,* **24** (2011) 153.
10. T. Fukui, H. Tanino, Y. Fukuda, M. Kuki, T. Watanabe, H. Kinoshita, and T. Harada, *J. Photopolym. Sci. Technol.,* **28** (2015) 525.
11. M. Yoshifuji, S. Niihara, T. Harada, and T. Watanabe, *J. Photopolym. Sci. Technol*., **31** (2018) 215.
12. M. Yoshifuji, S. Niihara, T. Harada, and T. Watanabe, *Jpn. J. Appl. Phys.*, **58** (2019) SDDA02.
13. Z. H. Levine, S. Grantham, and T. B. Lucatorto, *J. Micro/Nanolith. MEMS MOEM.,* **8** (2009) 021202

Technical Paper

Journal of Photopolymer Science and Technology
Volume 36, Number 1 (2023) 61 − 66 ©2023SPST

Photoresist Design to Address Stochastics Issues in EUV Resists

Florian Kaefer[1], Chenyun Yuan[1], Cameron Adams[2], Rachel Segalman[2] and Christopher K. Ober*,[1]

[1]Materials Science and Engineering, Cornell University, Ithaca 14853, NY, USA
[2]Chemical Engineering and Materials, UC Santa Barbara, Santa Barbara, CA, 93106-5080
cko3@cornell.edu

Low stochastics, high sensitivity photoresists remain a goal for EUV lithography. Here we contrast two positive photoresist systems, polypeptoids (PPs) and poly(phthalaldehyde)s (PPAs), both of which are selected to minimize chemical stochastics. In the former, a chemically amplified resist with identical molecular weight, composition, and sequence is studied. In the latter, a PPA homopolymer enables preparation of a chemically homogeneous resist which can be chemically scissioned in exposed areas. We report the results of exposure of these materials to DUV, e-beam and EUV radiation and physical changes that occur. In addition, we highlight unexpected observations of the role of sequence on lithographic performance.

Keywords: EUV photolithography, Stochastics, Sequence control, Polypeptoid, Polyphthaldehyde

1. Introduction

The development of EUV photoresists continues to be hampered by the issue of stochastics, that is, the random probability distributions of exposure dose, and secondary electron generation that changes solubility in a photoresist with its inherent variation in molecular size and molecular composition which ultimately leads to imperfections in pattern formation. For example, in a classical chemically amplified photoresist there is: i) heterogeneity in polymer molecular size, composition and sequence and ii) in the mixing of the photoresist and photoactive additives [1]. The effect of inhomogeneity is believed to contribute to line edge roughness and defect formation among other issues. Most polymer preparation methods in which several building blocks are incorporated results in strong compositional heterogeneity due to the statistical nature of random copolymerization.

In recent studies, metal organic clusters (MOCs) have been shown to produce high resolution photoresists. It could be argued that the basic molecular structure of MOCs leads to molecular homogeneity [2]. Nevertheless, there remain advantages in working with polymer systems if chemical stochastics and thus patterning stochastics can be addressed. The chemical versatility of monomer building blocks remain very attractive if chemical control of synthesis can be implemented. In this report we discuss recent approaches to chemical control of stochastics in which: 1) a self-immolative resist is used to mitigate the effect of chemical variability in a photoresist by focusing on homopolymer design [3] and 2) solid supported synthetic chemistry is used to prepare polymer chains that eliminate chemical variability and are identical in composition, molecular weight and in sequence [4].

Self-immolative polymers have been previously studied as photoresists, particularly for mask writing. These polymers, with relatively low ceiling temperatures, will revert to monomer under the right thermal conditions after radiation exposure. They are generally homopolymers and while they may have high molecular weight the depolymerization process means that molecular size is not a critical factor in image formation. Poly(alkylene sulfone)s are one family of such polymers [5].

Received May 7, 2023
Accepted May 10, 2023

Poly(phthalaldehyde)s are an alternative family of scissionable polymers [6] that we have studied in this context. We compare these highly sensitive resists that depend on a non-ionic photoacid generator for pattern formation [7] to the peptoid materials and what it implies for peptoid design.

Peptoids instead are aliphatic polyamides that mimic the structure and sequence control of proteins, are easier to synthesize, and yet are different because they both lack stereocenters present in proteins, and they have functional groups attached to nitrogen rather than carbon [8]. This polymer family, prepared using a robot synthesizer system originally developed for protein synthesis, depends on polymer supported chemistry and can result in multigram yields. The number of units in each chain is identical, the average composition is identical, and the sequence is identical thus minimizing issues of compositional stochastics.

In our prior report [9] on peptoid resists, we prepared sequences with tyramine as PHOST analog using the t-BOC protecting group in combination with hydrophobic comonomers such as phenyl ethylene amine and propargyl amine units. In this report we expand on the hydrophobic groups and explore the effect of sequence selection on patterning and development and to update our progress on the study of these new polymer systems.

Ongoing studies of the lithographic behavior of these resist systems have been carried out using DUV, e-beam and EUV radiation and will be discussed.

2. Experimental

All reagents were purchased from Sigma Aldrich, Millipore Sigma, TCI America, and Oakwood Products at the highest purity available and used without further purification. Tyramine, diphenyl propyl amine and hexyl amine were purchased from Sigma Aldrich and used as received.

2.1 Synthesis of poly(phthalaldehyde) (PPA)

The PPA polymers with bromine substituents have been previously reported and are included here to compare with the peptoid resists [10]. In a sample synthesis of PPA, Br-phthalaldehyde monomer and boron trifluoride etherate initiator were added to a Schlenk flask [11]. The solids were dissolved in THF and then the solution cooled to -78 °C. The reaction was left stirring at -78 ℃ for 2 h, then pyridine was added. The reaction was stirred an additional *2 h* while maintaining at *-78 °C*. The solution was then warmed to room temperature and the polymer was precipitated by adding slowly into methanol. The white powder was collected by filtration, then further purified by dissolving in dichloromethane and re-precipitating from methanol and washing in diethyl ether The polymers were further purified by dissolving in dichloromethane and re-precipitating into methanol. The resulting polymers are shown in Scheme 1.

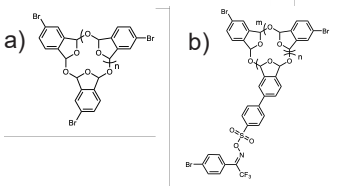

Scheme 1. PPA Polymers a) without PAG attached and with b) PAG attached.

Photoresist solution containing *5 wt.%* polymer in cyclohexanone blended with PAG was prepared in varying ratios of *10-20 wt.%* to PPA. The solution was then spin coated onto a silicon wafer at *3000 rpm* for *1 min* and post baked at *90°C* for *1 min* to remove excessive solvent.

2.2 Synthesis of peptoid photoresists

The peptoid syntheses were conducted using a CSBio Peptide Synthesizer, Model CS336X. The important structural units and a typical sequence are shown in Scheme 2. For the solid-phase supported synthesis of the peptoids *1g* of 2-chlorotrityl chloride resin with a loading of *1.7 mmol* g^{-1} was swollen in dichloroethane (DCE) for 10 minutes and washed with dimethyl-formamide (DMF). The first

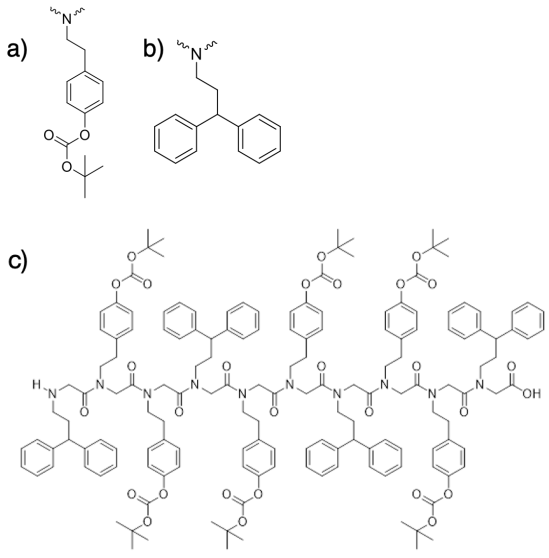

Scheme 2. Key building blocks in peptoid photoresist: a) t-Boc protected tyramine and b) diphenylpropyl amine. c) Peptoid sequence prepared for these studies. These components produce e-beam and EUV resists capable of sub-20 nm resolution.

bromoacetylation step was carried out by adding *10 mL* of a *1.3 M* bromoacetic acid (BAA) in DMF and *10 mL* of a *1.3 M N, N*-diisopropylethylamine (DIEA) in DMF to the resin and bubbling with nitrogen and shaking for 30 minutes. The resin was then washed repeatedly with DMF. Amination was performed by reacting the acylated resin with *1-2 M* of the amine in DMF for *60 minutes* constantly bubbling nitrogen and shaking the reactor. Additional bromoacetylation steps were conducted with *1.2 M* BAA and *1.4 M N, N'*-diisopropylcarbodiimide (DIC) in DMF. Cleavage was accomplished by treatment with *20%* hexafluoroisopropanol in dichloromethane (DCM). The resin was filtered, and the solution was concentrated via rotary evaporation and lyophilized. The resulting solid was dissolved in 1:1 acetonitrile/water and purified using a preparative HPLC and lyophilized and characterized using a Bruker Matrix Assisted Laser Desorption - Time of Flight (MALDI-TOF) Bruker AutoFlex Max tool. To introduce solubility switching groups the tyramine hydroxyl groups were protected with of di-tert-butyl dicarbonate (tBOC). For the *1*g peptoid synthesis, it was dissolved in *10 mL* acetone and *1.3 equivalents* of tBOC and *0.1 mol* equivalent 4-dimethylaminopyridine (DMAP), were added and the solution was stirred for *24 hours* at room temperature. Afterwards, the sample was concentrated, purified by preparative HPLC and lyophilized. The resulting solid was characterized using MALDI-TOF.

2.3 Lithographic characterization:

For deep-ultraviolet (DUV) exposures *25 mg* peptoid were dissolved in *1ml* of propylene glycol methyl ether. To this solution *20 wt%* (with respect to peptoid) photoacid generator (TPS-nonaflate) was added and the solution was sonicated for 5min. The solution was filtered, and spin coated on a UVO cleaned silicon wafer. The coated wafer was post-apply baked for *60s* at *110℃*.

DUV exposures were conducted on an ASML PAS 5500/300C Wafer Stepper. When carried out, E-beam exposures were performed using a JEOL 6300, *100kV* e-beam tool. After exposure, the patterns were post-exposure baked for *60s* at *110℃* for 60s and developed in the appropriate developer (aqueous base or solvent depending on the sequence). The resulting patterns were characterized using a Zeiss-Gemini-500-FESEM.

Extreme-ultraviolet exposures were conducted at the Paul-Scherrer Institute (PSI) in Switzerland. After exposure, the patterns were post-exposure baked for *60s* at *110℃* for *60s* and developed in the appropriate developer (aqueous base or solvent depending on the sequence). The resulting patterns were characterized using a Zeiss-Gemini-500-FESEM.

3. Results and discussion

3.1 Patterning. Behavior of Brominated PPA Resists

In our study of PPA photoresists we incorporated Br as a substituent for subsequent modification of each repeat unit and on the hope that Br might enable direct radiation induced depolymerization. Instead, we found that the presence of Br enhances the stability of the PPA and gives it better shelf life, but it does require a PAG to induce depolymerization [10]. The resulting polymer had a molecular weight of ~3,000 g/mol and was soluble in solvents such as cyclohexanone. We chose non-ionic PAGs for incorporation as a free component and for direct attachment to the polymer itself. Active and inactive PAGs are shown in Scheme 3.

Interestingly, not all non-ionic PAGs are active under EUV conditions even though they work under DUV and e-beam conditions and as shown in Scheme 3 similar PAGs do have different activities which we ascribe to the nature of bonding around the groups that lead to release of the sulfonic acid.

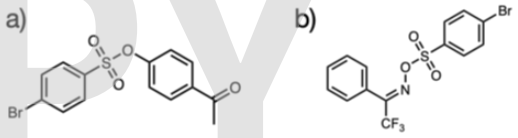

Scheme 3. Non-ionic PAGs investigated with Br-PPA EUV resists. PAG a) is EUV inactive while PAG b) is very EUV active.

An EUV active and EUV inactive PAG are shown in the figure. We consider the actions of secondary electrons in bond cleavage events to be the source of this difference. PAGs with a C-O-S linkage are EUV inactive whereas PAGs with an N-O-S linkage is very active. DFT studies suggest that the O-S bond is weaker in the C-O-S PAGs while the N-O bond is weaker in the N-O-S PAGs [10]. We will pursue EUV active PAGs in our future peptoid studies for incorporation directly the polymer backbone.

Resolution in photoresists is controlled by the solubility difference between the exposed and unexposed regions. Similarly, line edge roughness has been correlated to inhomogeneities in regions of the resist possessing both soluble and insoluble components after exposure [12]. These inhomogeneities are partially the result of stochastics in the initial distribution of photoacid generators and solubility change groups [13]. Minimizing such variations via control of the polymer's molecular size is crucial to achieving the

lithography performance requirements set by the IEEE IRDS [14].

In order to minimize stochastics variability, we explored incorporating PAG groups on each and every repeat unit in our PPA photoresists. Monomers were modified before polymerization and tested under various exposure conditions. The all PAG resists were found to be extraordinarily sensitive requiring doses well under 5 *mJ/cm*^{2} by EUV exposure. Only when 1 PAG was incorporated per chain (or per macrocycle in the tested materials)

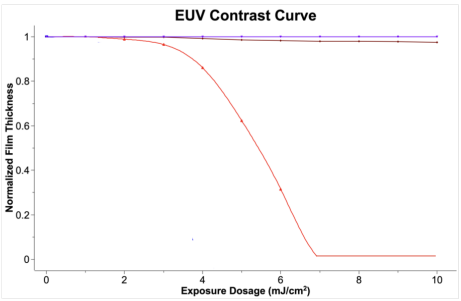

Figure 1. EUV contrast curves for inactive Br-PPA resist alone (Scheme 1a), with inactive PAG on macrocycle and active PAG on macrocycle (Scheme 1b) exposed to EUV source. Data from reference 15.

were we able to produce reasonable results.

Figure 1 shows the contrast curves for the EUV inactive Br-PPA homopolymer resist alone (Fig. 1a), with the Br-PPA with inactive PAG, both with unchanging contrast curves and the active PAG on macrocycle (Fig. 1b) exposed to EUV. Several other PAGs were tested and showed in the fastest case maximum contrast at *2mJ/cm*^{2} or faster with a single PAG per macrocycle. Importantly, this suggests that we can think about stochastics more broadly than all repeat units are identical and design macromolecular units that have identical size, composition and sequence but made from different components.

3.2 Patterning. Behavior of Peptoid Resists

Peptoids possess repeat units built from *N*-substituted glycines. Compared to peptides, peptoids present numerous advantages including a wider range of functional groups and lower-cost. More efficient synthesis enables production of higher molecular weights with high precision when compared to protein synthesis in molecular weight ranges suitable for photoresists [16]. The most well-developed solid-phase method is the submonomer synthesis (SMS), which combines two types of repeat units, primary amines and bromoacetic acid, in a stepwise manner [17]. Following synthesis, preparatory HPLC is used to remove any excess lower molecular weight segments that might have been produced [18].

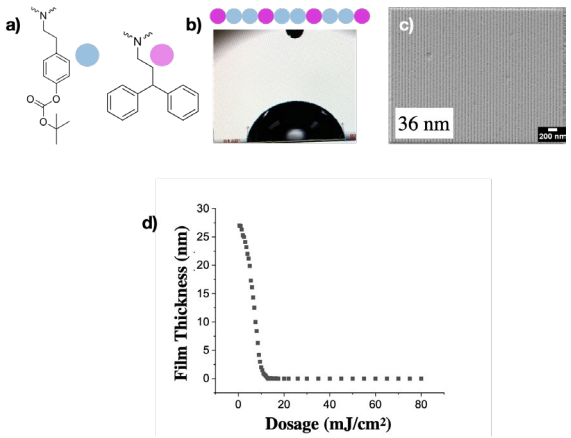

Figure 2. a) Structure of amine units in peptoid repeat. t-Boc protected tyramine is colored cyan and diphenylpropyl amine is colored magenta. B) An effective sequence is shown with 4 diphenylpropyl amine units and 6 tyramine units in a decamer (Scheme 2c). All peptoids in a sample have the same quantity of each unit type in the same length chain with the same sequence. The resist is moderately hydrophobic. c) The micrograph shows a 36 nm line/space pattern made using e-beam exposures. Recent results from both e-beam and EUV patterning are approaching *15 nm* resolution. d) Contrast curve for tyramine/diphenyl propyl amine peptoid exposed to EUV radiation.

In this report we briefly describe resists made with tyramine and diphenylpropyl amine (Figure 2) [19]. The molecular weight of each molecule of peptoid is 2687 g/mol.

This polypeptoid can be dissolved in acetone, isopropyl alcohol, N,N-dimethylformamide and acetonitrile. In these sequences we have used our understanding of the importance of the distribution and sequence of the tyramine (PHOST mimic) in the sequence and observed the effect of architecture of lithographic performance first using DUV patterning of these materials. Subsequently we used e-beam patterning and most recently EUV patterning at the Paul Scherer Institute.

Development conditions originally required inorganic solvent due to the high polarity of the peptoid backbone, but with the introduction of hydrophobic peptoid units (diphenyl propylamine), we are now able to develop patterns in dilute aqueous base. The appropriate selection of sequence and the more hydrophobic peptoid sequence has led to a dramatic improvement in peptoid resolution

under e-beam and EUV exposures (see Fig. 2c). The result of patterning studies has shown the ability to produce patterns that are comparable to those produced by all but the best metal organic cluster photoresists.

As we relate sequence to enhanced development, we find that the overall sensitivity of the peptoid resists is showing marked improvement. At present we are using free ionic PAGs (TPS-nonaflate) and anticipate even more improved performance when we incorporate PAGs (non-ionic) into the peptoid sequence. As an example of the current sensitivity of these peptoid resists, we provide a contrast curve for EUV exposure in Fig. 2d [20].

At present there remains much to explore as we continue to introduce new functions into these peptoid systems including units for etch resistance, units that enhance resist adhesion or compatibility with ARC materials. We need to understand how their inclusion content and placement in a sequence influence resist performance.

4. Conclusion

To summarize, these photopolymers have shown high sensitivity EUV photoresponse and each family brings advantages to high resolution patterning. Through the PPA polymers and the covalently attached PACs we have shown that certain non-ionic PAGs are effective while others are not and we believe that characteristic depends on bond breakage behavior due to secondary electrons. Active PAGs produce very sensitive self-immolative PPA photoresists and our original idea of placing a PAG on each repeat to minimize stochastic variability becomes impractical due to the high speed of the resist. Instead, we obtain our best PPA performance using a single PAG per chain.

In the peptoids, we take the idea that good stochastics can be achieved through identical molecules without needing to make each repeat unit in a polymer identical. In the case of peptoids, sequence, function location, overall size and solubility contrast are all important and can be achieved by use of multiple monomers. We will also in future incorporate non-ionic, EUV active PAGs to enable control of PAG location and incorporation into each molecule. Both avenues (PPA and peptoid) have not been fully explored and given the progress to date, offer real potential to continue to improve on resolution, sensitivity and EUV resist performance.

Acknowledgements

We are grateful to Intel Corp for support of Dr. F. Käfer through its CINEMA program on photoresist design. We thank Dr. Jingyuan Deng for his work on poly(phthalaldehyde)s supported through SRC. We also acknowledge Center for High Precision Patterning Science (CHiPPS) (DE-AC02-05-CH11231) for support of Chenyun Yuan and Cameron Adams. The authors thank the Intel Corporation for financial support of the CINEMA program. We would also like to thank the Paul-Scherrer Institute, Switzerland especially Michaela Vockenhuber for the EUVL experiments. This work was performed in part at the Cornell NanoScale Facility, an NNCI member supported by NSF Grant NNCI-2025233. Furthermore, this work made use of the Cornell Center for Materials Research Shared Facilities which are supported through the NSF MRSEC program (DMR-1719875).

References

1. A. Lio, *Proc. of SPIE,* **97760V-14** (2016) 9776.
2. H. Xu, K. Sakai, K. Kasahara, V. Kosma, K. Yang, H. C. Herbol, J. Odent, P. Clancy, E. P. Giannelis, C. K. Ober, *Chem. Mater*., **30** (2018) 4124.
3. J. Deng, S. Bailey, S. Jiang, C. K. Ober, *JACS,* 144(42) (2022) 19508
4. M. E. Barry, P. A. Gokturk, A. J. DeStefano, W. v. Zoelen, A. K. Leonardi, C. K. Ober, E. J. Crumlin, R. A. Segalman, *ACS Appl. Mater. Interfaces* 14(5) (2022) 7340.
5. T. Ueno*, J. Photopolym. Sci. Technol.* 26(1) (2013) 3.
6. C. Aso; S. Tagami, *Journal of Polymer Science Part B: Polymer Letters.* 5 (3) (1967) 217
7. J. Deng, S. Bailey, S. Jiang, C. K. Ober, *Chem. Mater.* **34(13) (**2022) 6170
8. RJ Simon, RS Kania, RN Zuckermann, VD Huebner, DA Jewell, S Banville, S Ng, L Wang, S Rosenberg, CK Marlow, *Proc. NAS.* **89**(20) (1992) 9367.
9. Florian Kaefer, Zoey Meng, Rachel Segalman and Christopher K. Ober, *J. Photopolym. Sci. Tech*., **35(1)** (2022) 29.
10. J Deng, S Bailey, R Ai, A Delmonico, G Denbeaux, S Jiang, C. K. Ober**,** A*CS Macro Lett.* **11** (2022) 1049
11. J. A. Kaitz; C.E. Diesendruck; J.S. Moore, *J. Am. Chem. Soc.* 135(34) (2013) 12755.
12. T. Kozawa and S. Tagawa, *Jpn. J. Appl. Phys.,* **49** (2010) 030001.
13. P. D. Ashby, D. L. Olynick, D. F. Ogletree and P. P. Naulleau, *Advanced Materials*, **27** (2015)

5813-5819.
14. M. Neisser, H. Levinson, *Proc. SPIE,* **11323, XI** (2020).
15. J. Deng, PhD Thesis, Cornell University, 2022.
16. N. Gangloff, J. Ulbricht, T. Lorson, H. Schlaad, R. Luxenhofer, *Chem. Rev.,* **116** (2016) 1753.
17. A. M. Rosales, R. A. Segalman, R. N. Zuckermann, *Soft Matter* 9, (2013) 8400.
18. S. D. Ganesh, N. Saha, O. Zandraa, R. N. Zuckermann, P. Sáha, *Polymer Bulletin*, 74, (2017) 3455
19. J. Seo, B.-C. Lee, R. N. Zuckermann, *Comprehensive Biomaterials*, 2, (2011) 53.
20. F. Kaefer; C. K. Ober; Z. Meng; R. Segalman; J. Read de Alaniz, *Proc. SPIE 12498*, Advances in Patterning Materials and Processes XL, 1249817; doi: 10.1117/12.2658413

Instructions to Authors

Journal of Photopolymer Science and Technology is devoted to the publication of articles on the scientific progress and the technical development of photopolymers.

1. General Paper, Communication, Technical Paper, and Review are published.
2. All contributions should be written in English.
3. All the articles must contain an abstract and 3~6 keywords. The abstract should be a single paragraph (50–250 words) that summarizes the content of the article.
4. Communication is short submission of 4~6 pages which contain new results. The contents of Communication may be republished with more details.
5. Manuscripts should be prepared with following the Manual for Manuscript Writing.
6. The day on which the manuscript arrives at the editorial office shall be the received date.
7. The authors bear full responsibility for the content of their articles.
8. All the papers submitted are reviewed by the referee system of the Journal. The editorial board requests to revise the manuscript when the reviewer's comments have good reason. The revised manuscript should be submitted before the deadline proposed by the editorial board.
9. To support a part of the cost of publication of journal pages, the author's institution is requested to purchase reprints.
10. The authors of manuscripts for the Journal should follow the document. Submit the manuscripts to Editorial Manager.

The Editorial Office
Haruyuki Okamura
Journal of Photopolymer Science and Technology
Department of Applied Chemistry, Osaka Prefecture University, 1-1 Gakuen-cho, Naka-ku, Sakai, Osaka 599-8531, Japan
E-mail: okamura@chem.osakafu-u.ac.jp

11. The electronic file may be used for the electric publication of the Journal and for the direct printing process of publication. Note: In all cases the Editorial Office reserves the right to decide whether to use a manuscript from authors' files or not.

Manual for Manuscript Writing

All the papers submitted are reproduced as they are. For this reason, manuscript should be prepared according to the items given below.

Size of sheet

White A4 sheets, 210 mm × 297 mm in size, should be used for submissions, and the manuscript be clearly prepared. The total pages of manuscript are recommended to be even.

Format

Manuscript should be started from the title, author's name, affiliation, address including e-mail address, abstract, and text. The manuscript should be prepared by using a word software with the font "Times New Roman" for Windows series or "Times" for Macintosh series. The font-size and the line spacing should be set 11 point and 13 point, respectively except title (18 point and 18 point), abstract, keywords, figure and table captions (10 point and 12 point). Use the bold face for author's name and keywords, and the italic for affiliation and address including e-mail address (See Table 1). The first letter of each important word in the title should be capitalized. Math and Equations should be written using either the Microsoft Equation Editor or the MathType commercial add-on for MS Word for all math objects in your paper. Number of equations should be placed consecutively after the equation with numbers in parentheses with the margin, as in (1). Be sure that the symbols in your equation are defined before or immediately after the equation. The example of equation (1) is shown as follows:

$$R_{\mathrm{p}} = \frac{\mathrm{d}[M]}{\mathrm{d}t} = k_{\mathrm{p}}[M]\left(f\phi I_{\mathrm{abs}}\right)^{0.5} k_t^{-0.5} \qquad (1)$$

The word processing software recommended is MS Word which is used for the preparation of the example of manuscript. The layout of the paper is shown in Figs. 1-3. The right and left columns end in the same line.

For the separation of sections in the manuscript, use the following system,

3. Result

3.1. .....

3.1.1. .....
3.1.1.1. ....

All the figures and tables with captions should be pasted directly on the sheets of manuscript at the appropriate place in the text where they are cited. Do not collect them at the end of your paper.

Table 1. Font sizes, styles and line spacing.

Type size/line spacing (pts)	Regular	Bold	Italic
10/12	Abstract, figure captions, table text, figure text	Keywords	
11/13	Main text, secondary and tertiary section headings	Author's name, a primary section heading	Address and affiliation
18/18	Title of the paper		

Electronic submission

The editorial office strongly recommends the electronic submission via https://www.editorialmanager.com/photopolymer/default.aspx for fast publication.

The submission of files of main text (.doc or .docx), Journal Check List, and Copyright Transfer Agreement are mandatory. The files of main text (.pdf), Reprint Order Form, and supplementary information are optional. If you have any trouble in electronic submission, the contents of the Web site "http://www.editorialmanager.jp/faqen" will help you before the contact to the editorial office. Especially, the author should note that electronic submission should be completed after "[Approve Submission]" action.

Conclusion

Conclusion is one of the most important parts of a paper. Please give careful consideration to this section.

References and footnotes

References and footnotes are to be indicated by Arabic numbers in brackets, [ ]. They should be arranged in sequences and summarized at the last part of the text. All of the authors of the references should be written. The use of "et al." is not allowed because of the requirement for electronic publication. More than 20 references should be cited in a paper. Examples of references are written below.

1. T. Omote, "Polyimides", M. Ghosh, and K. L. Miital, Eds., Dekker, New York, 1996, p.121.
2. S. Hayase, K. Takano, Y. Mikogami, and Y. Nakano, *J. Electrochem. Soc.,* **138** (1979) 3625.
3. T. Omote, K. Koseki, and T. Yamaoka, *Macromolecules*, **23** (1990) 4788.
4. T. Omote, S. Hayashi, K. Ishii, K. Naito, and T. Yamaoka, *Adv. Technol.,* **4** (1993) 277.
5. D. N. Khanna and W. H. Mueller, *Polym. Eng. Sci.*, **29** (1989) 954.
6. H. Ahne, R. Rubner, and E. Kuhn, EP0023626, to Siemens, 1980.
7. R. Rubner, *Adv. Mater*, **2** (1990) 452.
8. T. Yamaoka, N. Nakajima, K. Koseki, and Y. Maruyama, *J. Polym. Sci. Polym. Chem.*, **28** (1990) 2517.
9. H. Ahne, E. Kuhn, and R. Ruber. U.S. patent No. 4,395,482 (1985).
10. M. Ueda, K. Seki, and Y. Imai, *Macromolecules*, **15** (1982) 17.

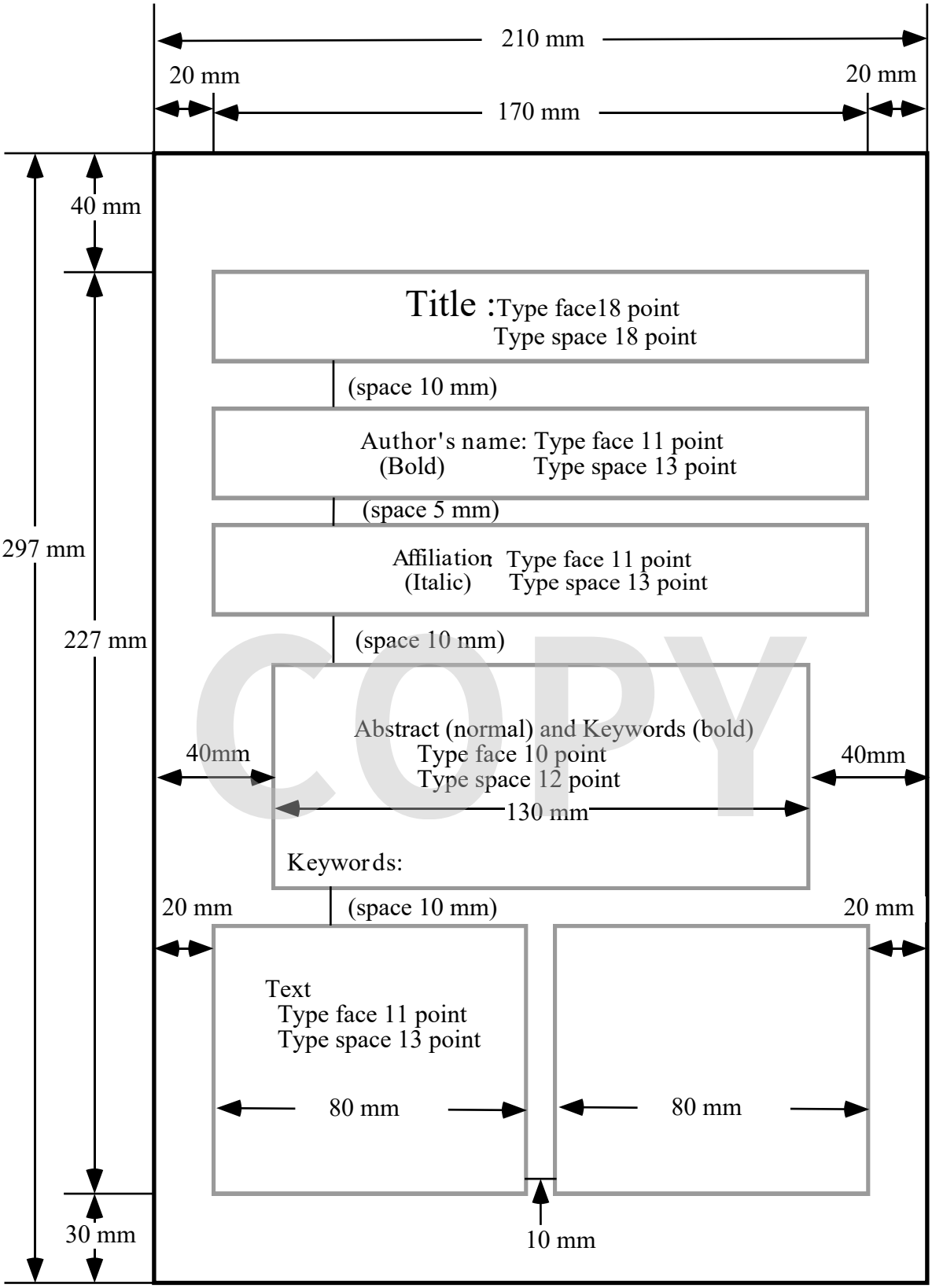

Fig. 1. The First Sheet of Manuscript. Type within the dotted block using "Times New Roman" font .

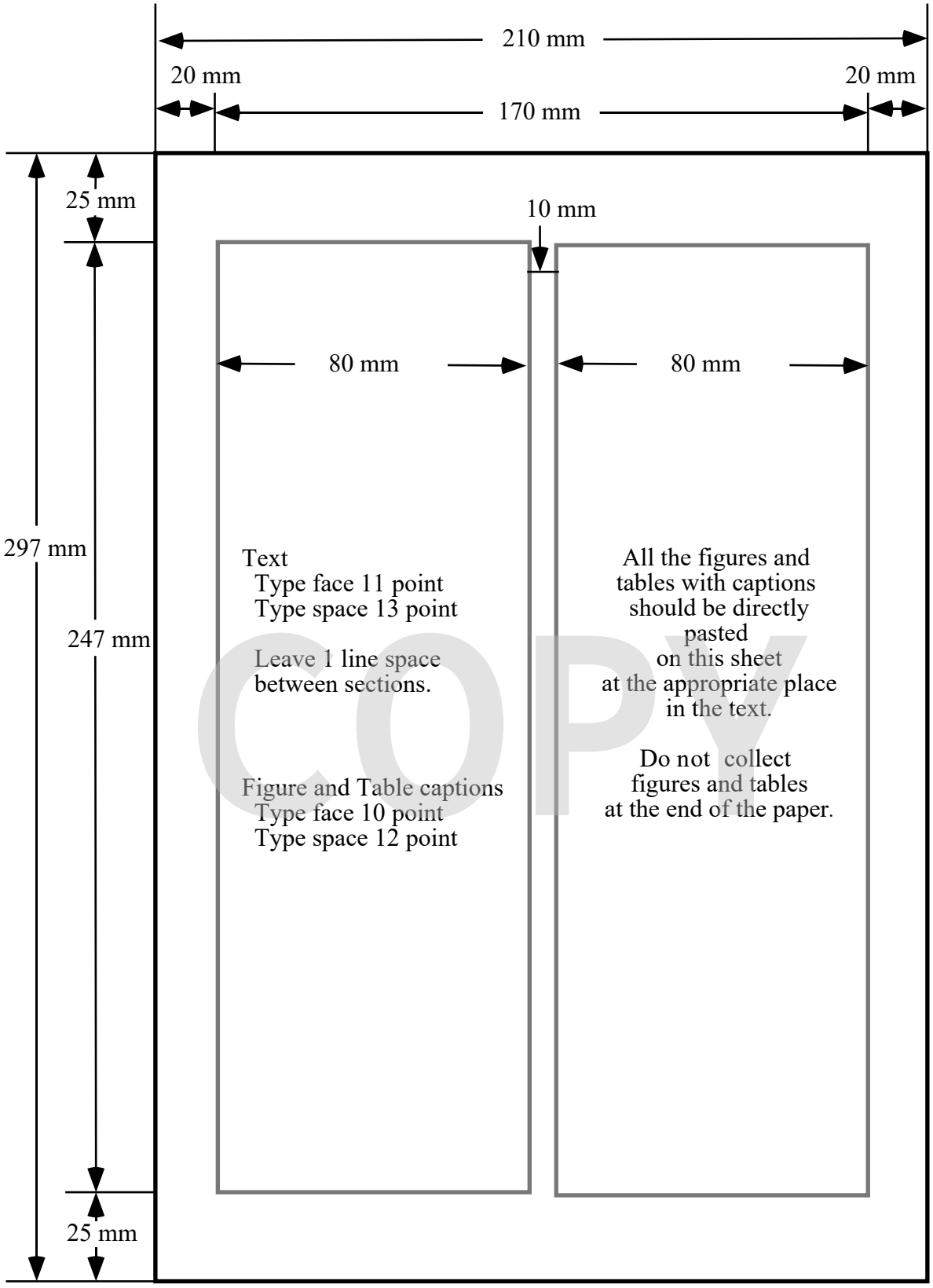

Fig. 2. Following Sheets of Manuscript

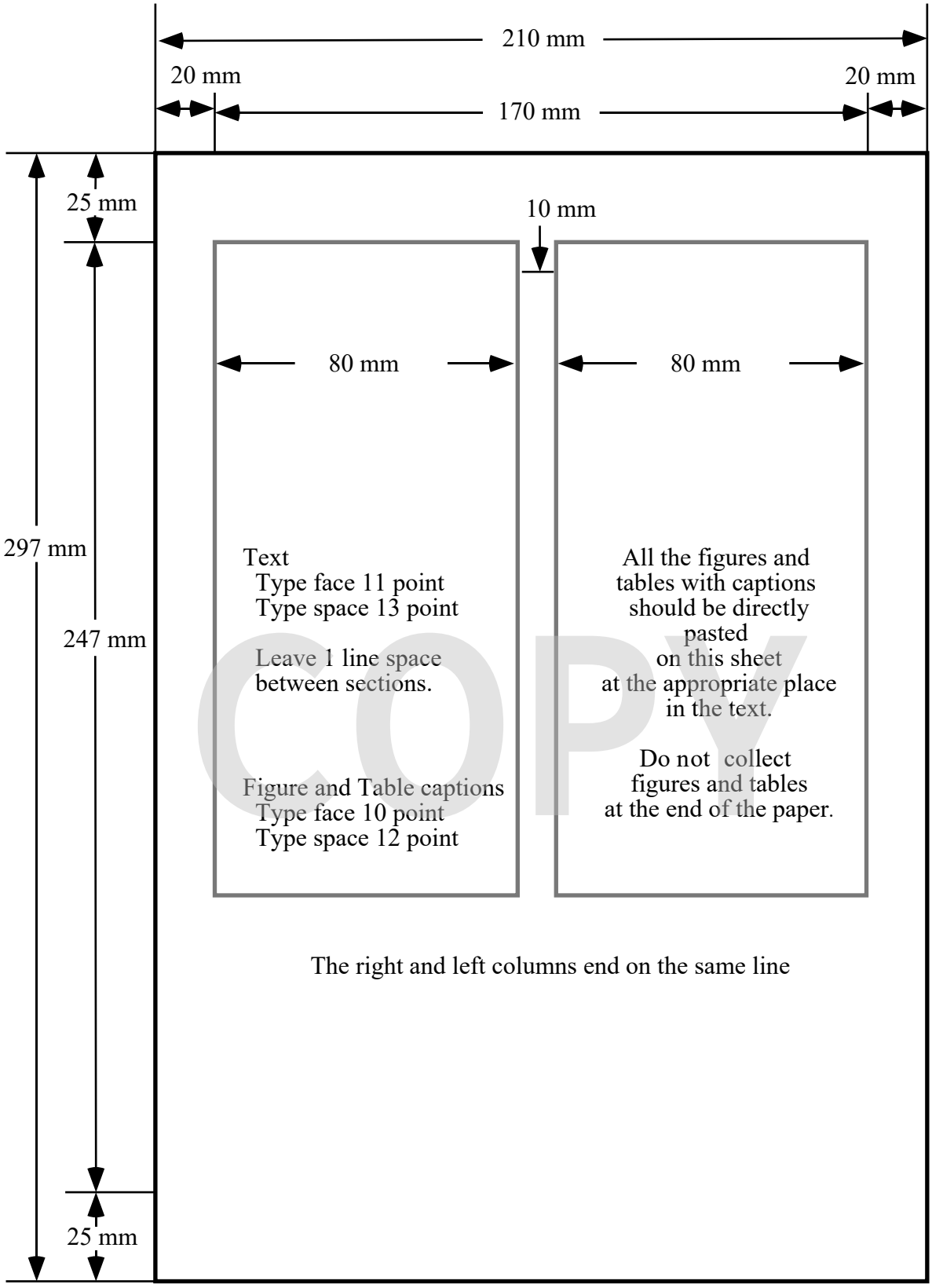

Fig. 3. Last page partly occupied

Example

Photoresists for Screen Printing Plates with High Resolution and Sensitivity Using Thiol-ene Reaction

Haruyuki Okamura[1*], Keiko Muramatsu[2], Hideyuki Nakajiri[2], Masamitsu Shirai[1], and Akikazu Matsumoto[1]

[1] Department of Applied Chemistry, Graduate School of Engineering, Osaka Prefecture University, 1-1 Gakuen-cho, Naka-ku, Sakai, Osaka 599-8531, Japan
[2] Research and Development Center, Nakanuma Art Screen Co., Ltd., 23 Uzumasa Yasui Okuhata-cho, Ukyo-ku, Kyoto 616-8082, Japan
**okamura@chem.osakafu-u.ac.jp*

Photoresists for high resolution screen printing plates was devised using thiol-ene reaction. New resist formulation contains a base polymer which contains acid-labile tetrahydropyranyl-protected carboxylic acid, hydroxyl and methacrylic functions. As crosslinkers, multifunctional acrylates and multifunctional thiols were employed. Photoacid generators were used for pattern formation. A 6-μm feature size of resist on a SUS screen plate was obtained on irradiation at 365 nm and followed by development. Post-exposure curing using 254 nm light with photoradical generators improved the mechanical characteristics of the resist patterns. Addition of a multifunctional thiol compound was effective to improve flexibility of the cured resist and resist sensitivity.
Keywords: Screen printing plate, Photoresist, Thiol-ene reaction, High resolution, High sensitivity

1. Introduction

Screen printing is a promising method to fabricate small feature size patterning of circuits for the production of electronic devises in terms of not only economical but also environmental issues compared to conventional lithographic methods. In this point of view, we have developed the photoresists for screen printing plates with high resolution [1-5]. The fabrication process of the screen plates is depicted in Fig. 1. The photoresist patterns contained a base polymer, a crosslinker, a photoacid generator (PAG) [6], and a photoradical generator (PRG) [7].

In this work, high-resolution screen printing plates were devised based on the findings previously reported [1-5]. New resist formulation contains a base polymer, which consists of acid-labile tetrahydropyranyl-protected carboxylic acid, hydroxyl, and methacrylic functions. As crosslinkers, multifunctional acrylates and thiols were employed. PAGs were used for pattern formation. Curing reactions of the acrylates are strongly inhibited in the presence of oxygen. The

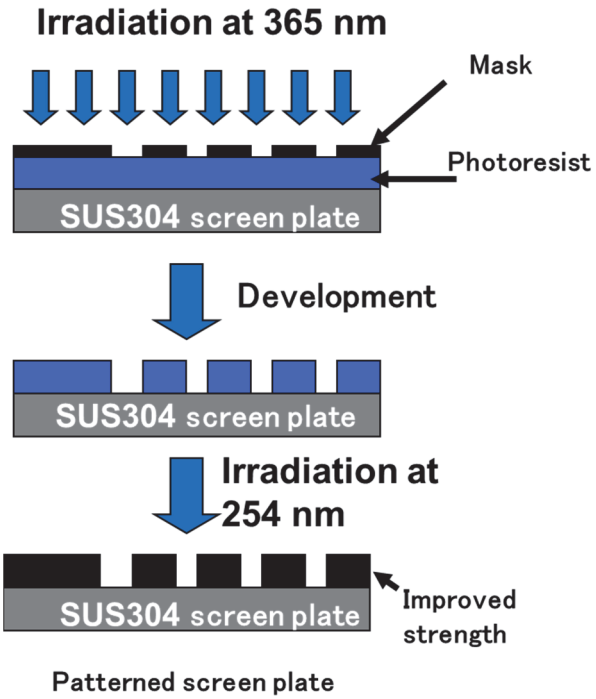

Fig. 1. Schematic illustration for the fabrication of screen plates.

oxygen inhibition was effectively suppressed by the use of thiol-ene photocuring system due to regeneration of thiyl radical in the presence of oxygen [8-10] (Scheme 1). Thus, application of thiol-ene system may afford high resist sensitivity and durability. Effect of the structures of thiol compounds on flexibility of the cured resist and resist sensitivity was also investigated.

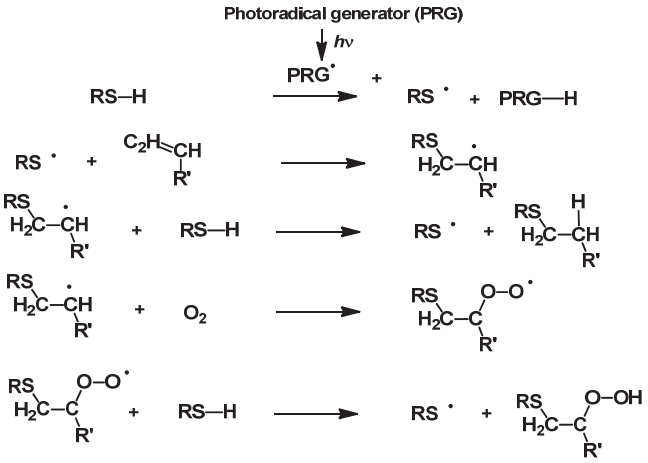

Scheme 1. Mechanism of thiol-ene reaction.

2. Experimental

The PAG diphenyl[4-(phenylthio)phenyl] sulfonium hexafluorophosphate (DPPTPSHFP) (product name: CPI-100P) (49 wt% propylene carbonate solution) was obtained from San-Apro Ltd. *N*-Trifluoromethanesulfonyloxy-7-*tert*-butylthianthrene-2,3-dicarboxylic imide (tBuTHITf) [11,12] (product name: SIN-11) was kindly donated by Sanbo Chemical Ind., Ltd. The PRG phenyl tribromomethyl sulfone (PTBMS) (Nacalai Tesque) was used as received. *O*-Benzoyl diacetone monooxime (BAOBE) [13] was prepared according to the literature. The crosslinkers DPHA (product name: A-DPH), and base polymer (product name: AP-HAR-201) were donated from Shin-Nakamura Chemical Co., Ltd. The difunctional thiol 1,1'-[(1-methylethylidene)-bis(4,1-phenylene-oxy-2,1-ethanediyl)] bis(3-mercaptobutylate) (BPMB) and the tetrafunctional thiol pentaerythritol tetrakis(3-mercaptobutylate) (PEMB) were obtained from Showa Denko K.K. and used as received. Chemical structures of the compounds are included in Schemes 2 and 3.

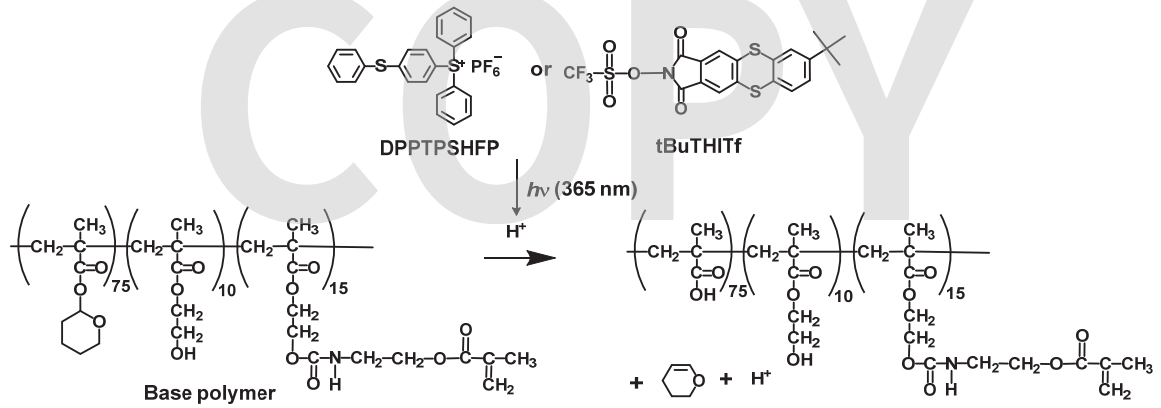

Scheme 2. Reaction mechanism of pattern formation on irradiation at 365 nm.

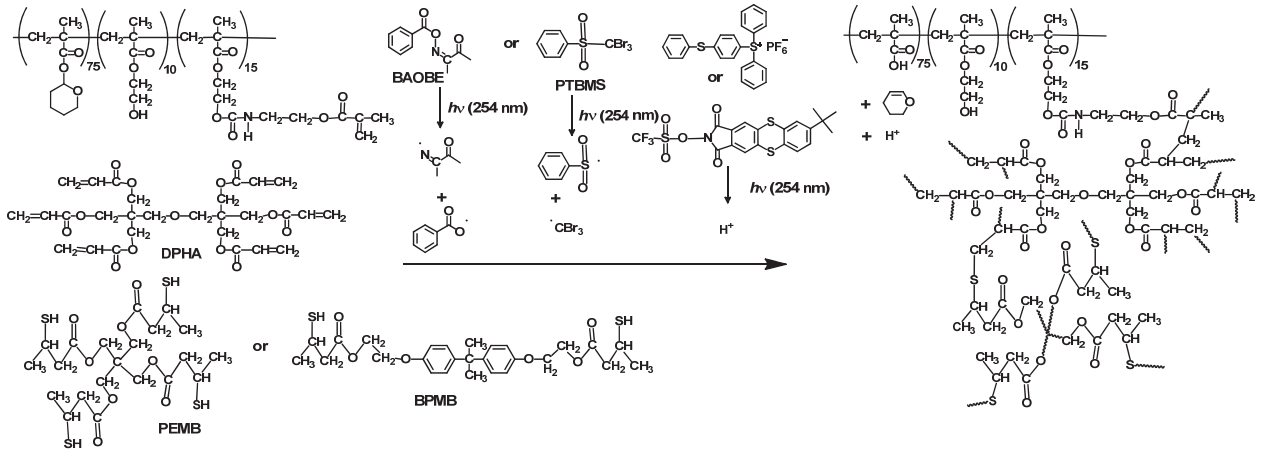

Scheme 3. Reaction mechanism of crosslinking on irradiated at 254 nm.

All sample films were prepared on silicon wafer by spin-casting or on poly(ethylene terephthalate) (PET) film (Cosmoshine A4100, 125 μm, Toyobo Co., Ltd.) by bar-coating from solutions of toluene containing the base polymer, the crosslinker, and a PAG and a photoradical generator. The sample films were dried on a hot plate at 90 ºC for 1 min. The thickness of films was about 0.5 μm. Irradiation was performed in air at 254 nm using a low-pressure mercury lamp (Ushio ULO-6DQ, 6 W) without a filter, at 365 nm using a Xenon lamp (Asahi Spectra MAX-301, 300 W) with a band-path filter for 365 nm, and at 230-420 nm using the Xenon lamp with a mirror which passes the light below 420 nm. The intensity of the light was measured with an Orc Light Measure UV-M02 and Ushio USR-45VA. Insoluble fraction was determined by comparing the film thickness before and after dipping into 2.38 wt% tetramethylammonium hydroxide (TMAH) solution or toluene for 10 min. Thickness of films was measured by interferometry (Nanometrics Nanospec M3000). The measurement of pencil hardness goes from the lowest to the highest pencil in order to determine the maximum hardness for scratching the surface of the film on silicon wafer (Method: JIS K 5600-5-4). The hardness of the film was determined relative to a standard set of pencil leads. The surface hardness is determined by scratching the leads across the coating at a controlled angle of 45°. The pencil hardness was measured using a pencil hardness tester (Imoto Machinery Co., Ltd.) with UNI pencil series supplied by Mitsubishi Pencil (Japan). Flexibility was evaluated in a cylindrical mandrel test according to JIS K5600-5-1. This test is performed using equipment in which the film coated on a PET film is attached and bent over a 5-mm-diameter glass rod. Flexibility is evaluated observing the presence or absence of cracks or defects in the film.

UV-vis spectra were taken on a Shimadzu UV-2400 PC. The patterns of the resists were observed using a Keyence digital microscope VHX-200. Screen printing was carried out using a screen-printing machine (LZ-1232, Newlong Seimitsu Kogyo Co., Ltd).

3. Results and discussion

3.1. Strategy

We selected the protected poly(methacrylic acid) by cyclic acetal units with methacryl side chains as a base polymer. The polymer widely used as a positive type photoresist using photoinduced-acid catalyzed deprotection of the cyclic acetal units [14] as shown in Scheme 2. Durability of the resist was improved by radical crosslinking reaction between the methacrylic group in the side chain of the base polymer and the crosslinkers with the thiol as shown in Scheme 3. Addition of thiol compounds affords the high efficiency of the crosslinking reaction.

Selection of PAG and PRG of the resists was very important in addition to the choice of light sources. We selected 365 nm-light which is emitted from a medium-pressure mercury lamp and 254 nm-light from a low-pressure mercury lamp. It is required that PRG did not affect the pattern formation by the decomposition of the PAGs on irradiation at 365 nm. Thus, the absorbance of the PRG at 365 nm must be much lower than that of PAGs on the resist formulations. Figure 2 shows the UV-vis spectra of the PAGs (DPPTPSHFP and tBuTHITf) and the PRGs (BAOBE and PTBMS) in acetonitrile. As shown in Fig. 2, the absorbance of the tBuTHITf was larger than that of DPPTPSHFP at 365 nm. The absorbance of BAOBE was larger than that of PTBMS.

On irradiation at 254 nm, the PRGs and PAGs absorb the light to form radicals [6,13,15] and acids [7,11,16-21], respectively. The produced acid promotes the deprotection reaction of tetrahydropyranyl-protected units to form 3,4-dihydro-2*H*-pyran, which affects not only the crosslinking reactions including thiol-ene reaction but also the mechanical properties of the resist.

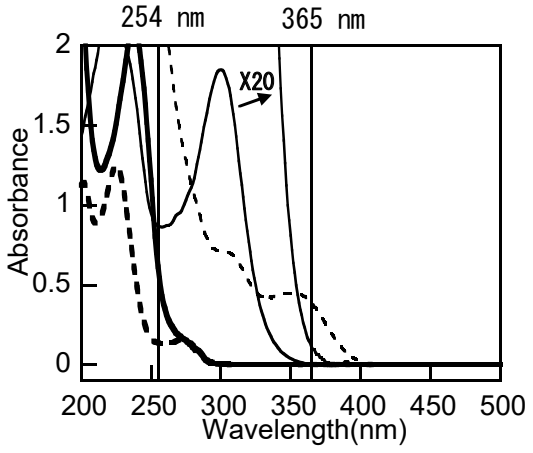

Fig. 2. UV-vis spectra of DPPTPSHFP (solid line), tBuTHITf (broken line), BAOBE (bold line), and PTBMS (bold and dotted line) in acetonitrile (1.0×10^{-4} M). For comparison, UV-vis spectrum of DPPTPSHFP (2.0×10^{-3} M) is also shown.

Table 1. Effect of formulation on sensitivity and mechanical property of the resist.

Composition (weight ratio)								Irradiation wavelength (nm)	Sensitivity (mJ/cm^2)			
Base polymer	DPHA	PEMB	BPMB	DPPTPSHFP	tBuTHITf	PTBMS	BAOBE		Dissolution in alkali[a]	Solvent resistance[b]	Flexibility[c]	Hardness[d]
100	14			4		1.2		365	1400	-[e]	-[e]	-[e]
100	14			4		1.2		254	-[e]	1200	-[e]	-[e]
100	14	7		4		1.2		365	700	-[e]	-[e]	-[e]
100	14	7		4		1.2		254	-[e]	800	-[e]	-[e]
100	14	10		4		1.2		365	400	-[e]	-[e]	-[e]
100	14	10		4		1.2		254	-[e]	400	-[e]	-[e]
100	14	14		4		1.2		365	400	-[e]	-[e]	-[e]
100	14	14		4		1.2		254	-[e]	400	-[e]	-[e]
100	14			4			1.2	365	1400	-[e]	-[e]	-[e]
100	14			4			1.2	254	-[e]	200	50	-[e]
100	14	14		4			1.2	365	400	-[e]	-[e]	-[e]
100	14	14		4			1.2	254	-[e]	< 50	< 25	-[e]
100	10	10		2			1.2	365	1400	-[e]	-[e]	-[e]
100	10	10		2			1.2	254	-[e]	< 10	< 15	100
100	10	10		2			1.2	230-420[f]	-[e]	400	2000	84000
100	10		10	2			1.2	365	1400	-[e]	-[e]	-[e]
100	10		10	2			1.2	230-420[f]	-[e]	28000	2000	2800[g]
100	7	14		2			1.2	365	1000	-[e]	-[e]	-[e]
100	7	14		2			1.2	254	-[e]	< 10	100	700
100	7	14			2		1.2	365	< 100	-[e]	-[e]	-[e]
100	7	14			2		1.2	254	-[e]	< 10	100	700

[a] Minimum irradiation dose for 95 wt% dissolution in 2.38 wt% TMAH for 10 min. [b] Minimum irradiation dose for 95 wt% insolubilization in toluene for 10 min. [c] Maximum irradiation dose to pass cylindrical mandrel test with 5 mm diameter. [d] Minimum irradiation dose to obtain 4H pencil hardness. [e] Not measured. [f] Light source: Xenon lamp. [g] 2H.

Thus, the balance of the generation of radicals and acids is important to improve the resist performance.

3.2. Formulation

To improve the performance of the resist, optimization of the resist formulation was required. The effect of PAGs, PRGs and thiols on resist performance was investigated. Especially, role of thiol compounds against the resist performance was mainly discussed.

We summarized the effect of formulation on sensitivity and mechanical property of the resist in Table 1. In this work, the methacryl monomer DPHA having six functionalities was employed. It is known that the crosslinker having high functionalities is effective to crosslink and enhance the hardness of the resists.

The effect of formulation on sensitivity on irradiation at 365 nm was investigated. The best sensitivity was obtained using tBuTHITf as a PAG, which is due to the strong absorption at 365 nm as shown in Fig. 2. In addition of the thiol compound PEMB increase the sensitivity because PEMB acts as a dissolution promotor and PEMB increases the flexibility of the resist, which enhances the deprotection reaction of the base polymer. Addition of the PRGs PTBMS and BAOBE did not affect the resist sensitivity, which indicates that the PRGs do not absorb 365 nm-light. Thus, thiol-ene reaction does not occur on irradiation at 365 nm.

The effect of formulation on solvent resistance, flexibility, and hardness of the crosslinked resist on irradiation at 254 nm was investigated. Solvent resistance of the crosslinked resist increased with irradiation dose for all formulations. Addition of PEMB drastically increased the solvent resistance. BAOBE was more effective than PTBMS due to larger absorption at 254 nm. When the formulation of the resist was [base polymer]/[DPHA]/[PEMB]/[DPPTPSHFP]/[BAOBE] = 100/7/14/2/1.2 by weight, the highest sensitivity (< 10 mJ/cm^2) for the solvent resistance was observed among the all formulations.

Using BAOBE as a PRG, flexibility of the crosslinked resist was investigated. Crosslinked resist loses its flexibility with irradiation dose due to high crosslinking density. Flexibility is very important for printing. The flexibility was enhanced by the addition of PEMB which incorporate the flexible units in the crosslinked resist with high solvent resistance. The high

flexibility was also appeared by the pencil hardness of the crosslinked resist. Structures of PAGs did not affect the mechanical properties.

The effect of the structure of the thiols on the sensitivity and the mechanical properties of the resist were investigated using PEMB and BPMB. The formulation of the resist was fixed to [base polymer]/[DPHA]/[thiol]/[DPPTPSHFP]/[BAOBE] = 100/10/10/2/1.2 by weight. On irradiation at 365 nm, the resist sensitivity using PEMB was similar with that using BPEM, which is due to no interference on the photoinduced-acid catalyzed deprotection reaction as shown in Scheme 2. On irradiation at 254 nm, the effect of the structures of the thiols was not appeared due to the high sensitivity of the thiol-ene system. Thus, a xenon lamp which emits continuous spectra between 230-420 nm was used. The resist containing PEBM showed higher performance than that of BPMB on the solvent resistance and hardness. The resist containing PEMB showed the same flexibility as that of BPMB. Thus, we conclude that the tetrafunctional thiol PEMB is better than BPMB having two functionalities.

3.3. Evaluation of screen plate

The effect of thiols on resist performance was investigated by the fabrication of screen plates on stainless steel screens. Three kinds of resist formulations were investigated. Table 2 shows the resist formulations and the sensitivity of the resist on irradiation at 365 nm for the formation of line and space pattern as shown in Fig. 3. The sensitivity was strongly affected by the content of DPHA and DPPTPSHFP. Addition of PEMB in the resist formulation did not affect the sensitivity of the resist. The optical microscope images of top side and bottom side of screen plates in Fig. 3 revealed that line and space patterns with the resolution of 11.5 and 8.5 μm was clearly observed. Some defects were appeared in only the screen plate containing PEMB. The results indicate that PEMB gives negative effect on resist resolution due to some side reaction. Optimization of the formulation of the resist may circumvent the problem.

We have successfully fabricated the screen plates with 6-μm resolution as shown in Fig. 4. Durability of the screen plates was also investigated using the finest screen plates with 6-μm line and space widths. Figure 4 shows the optical microscope images of the screen plate with (a) and without ((b), (c)) PEMB before and after printing 100 sheets.

Before printing, 6-μm line and space patterns were clearly obtained for the both resists. After printing 100 sheets, the damages of the resist without PEMB pattern were clearly observed as shown in Fig 4 (c). On the other hand, no damage was observed for the screen plate without PEMB. Thus, the addition of PEMB enhances the toughness of the resist on the screen plates. The result is consistent to the observation of enhanced flexibility and hardness of the crosslinked resists in addition of PEMB.

Table 2. Resist formulation and sensitivity the resist for screen plate.

Composition (weight ratio)					Sensitivity (mJ/cm^2)
Base polymer	DPHA	PEMB	DPPTPSHFP	BAOBE	
100	33		5	1.0	2810
100	10		2	1.2	7190
100	10	10	2	1.2	8440

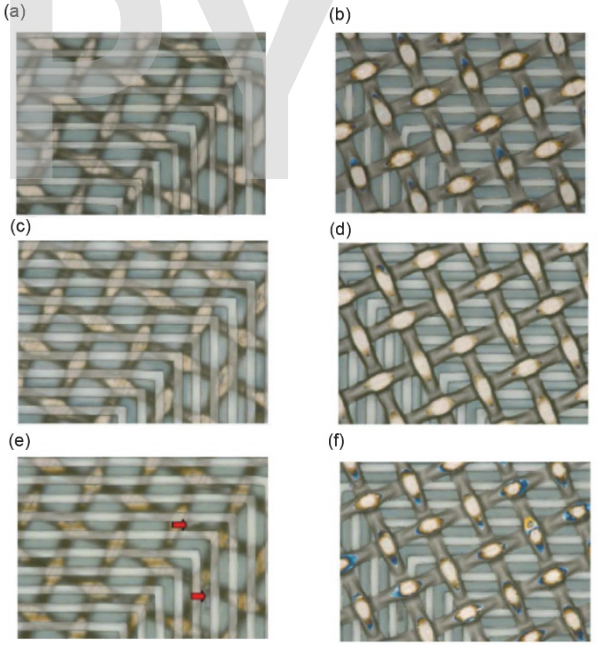

Fig. 3. Optical microscope images of top side ((a), (c), (e)) and bottom side ((b), (d), (f)) of screen plates.
L/S width: 11.5/8.5 (μm/μm).
Formulation: (a), (b); [base polymer]/[DPHA]/ [DPPTPSHFP]/[BAOBE] = 100/33/5/1 by weight.
(c), (d); [base polymer]/[DPHA]/[DPPTPSHFP]/ [BAOBE] = 100/10/2/1.2 by weight.
(e), (f); [base polymer]/[DPHA]/[PEMB]/ [DPPTPSHFP]/[BAOBE] = 100/10/10/2/1.2 by weight.
Arrows in (e) represent the positions of defects.

(a)

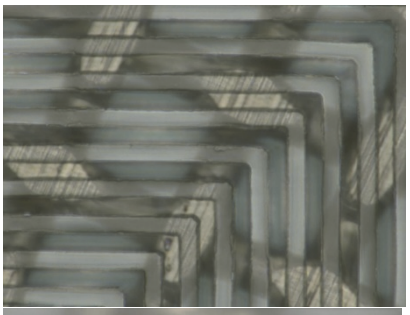

(b)

(c)

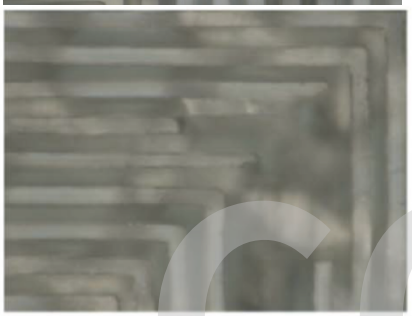

Fig. 4. Optical microscope images of screen plate before ((a), (b)) and after (c) printing 100 sheets.
L/S width: 6/6 (μm/μm).
Formulation: (a) [base polymer]/[DPHA]/[PEMB]/[DPPTPSHFP]/[BAOBE] = 100/10/10/2/1.2 by weight.
(b), (c); [base polymer]/[DPHA]/[DPPTPSHFP]/[BAOBE] = 100/10/2/1.2 by weight.

4. Conclusion

A 6-μm feature size of resist on a SUS screen plate was obtained on irradiation at 365 nm and followed by development with aqueous alkaline solution. Highest sensitivity was accomplished using tBuTHITf as a PAG. Post-exposure curing using 254 nm light with the PRG improved the mechanical characteristics of the resist patterns. BAOBE was more sensitive than PTBMS as the PRG. Resist durability was enhanced by the addition of thiols. PEMB having 4 functionalities was effective to enhance the resist durability.

Acknowledgement

This work was partly supported by a Grant-in-Aid for projects to support the advancement of strategic core technologies in contingency reserve of fiscal 2010, from MITI, Japan.

References

1. H. Okamura, M. Kayanoki, K. Takada, H. Nakajiri, K. Muramatsu, M. Yamashita, and M. Shirai, *Polym. Adv. Technol.*, **23** (2012) 1151.
2. K. Takada, J. Hamuro, T. Matoba, M. Yamashita, M. Shirai, and H. Okamura, Japan Patent JP 2015-59160A (2015).
3. K. Takada, J. Hamuro, T. Matoba, M. Yamashita, M. Shirai, and H. Okamura, Japan Patent JP2016-172811A (2016).
4. K. Takada, *Mater. Stage*, **15** (2015) 16.
5. L. Wang, J. Pfeifer, C. Balázsi, I. M. Szilágyi, and P. I. Gouma, *Proc. SPIE*, **6769** (2007) 6769E1.
6. J. V. Crivello and E. Reichmanis, *Chem. Mater.*, **26** (2014) 533.
7. B. M. Monroe and G. C. Weed, *Chem. Rev.*, **93** (1993) 435.
8. C. E. Hoyle, T. Y. Lee, and T. Roper, *J. Polym. Sci. Part A: Polym. Chem.*, **42** (2004) 5301.
9. Q. Li, H. Zhou, and C. E. Hoyle, *Polymer*, **50** (2009) 2237.
10. C. E. Hoyle and C. N. Bowman, *Angew. Chem. Int. Ed.*, **49** (2010) 1540.
11. H. Okamura, H. Naito, and M. Shirai, *J. Photopolym. Sci. Technol.*, **21** (2008) 285.
12. M. Shirai, H. Okamura, and M. Takahashi, Japan Patent JP5126873B (2012).
13. S. I. Hong, T. Kurosaki, and M. Okawara, *J. Polym. Sci. Polym. Chem. Ed.*, **12** (1974) 2553.
14. G. N. Taylor, L. E. Stillwagon, F. M. Houlihan, T. M. Wolf, D. Y. Sogah, and W. R. Hertler, *Chem. Mater.*, **3** (1991) 1031.
15. D. L. Fields, Jr. and H. Shechter, *J. Org. Chem.*, **51** (1986) 3369.
16. J. L. Dektar and N. P. Hacker, *J. Am. Chem. Soc.*, **112** (1990) 6004.
17. M. Shirai, *J. Photopolym. Sci. Technol.*, **20** (2007) 615.
18. H. Yamamoto, T. Asakura, Y. Nishimae, A. Matsumoto, J. Tanabe, J.-L. Birbaum, P. Murer, T. Hinterman, and M. Ohwa, *J. Photopolym. Sci. Technol.*, **20** (2007) 637.
19. T. Asakura, H. Yamato, and M. Ohwa, *J. Photopolym. Sci. Technol.*, **13** (2000) 223.
20. M. Shirai and M. Tsunooka, *Prog. Polym. Sci.*, **21** (1996) 1.
21. H. Okamura, "Hikari-kagaku no jiten", Asakura Pub. Co., Tokyo (2014) p. 190 (in Japanese).

TRANSFER OF COPYRIGHT AGREEMENT

Copyright to the article entitled

_____

_____

by

_____

_____

All Authors

Type of Paper (Mark below)

☐ General Paper ☐ Communication ☐ Technical Paper ☐ Review

is hereby transferred to the Society of Photopolymer Science and Technology (SPST), effective if and when the article is accepted for publication in **Journal of Photopolymer Science and Technology**

However, the authors reserve the following rights:

(1) All proprietary rights other than copyright, such as patent rights.

(2) The right to grant or refuse permission to third parties to republish all or part of the article or translations thereof. In the case of whole articles, such third parties must obtain SPST´s written permission as well. However, such permission will not be refused by SPST except at the direction of the authors. SPST may grant rights with respect to journal issues as a whole.

(3) The right to use all or part of this article in future works of their own, such as lectures, lecture notes, press releases, reviews, textbooks, or reprint books.

(4) In the case of a "work made for hire," the right of the employers to make copies of this article for their own use, but not for resale.

To be signed by at least one of the authors (who agrees to inform the others, if any) or, in the case of a "work made for hire", by the employer.

_____

Signature

_____

Name (Print)

_____

Title, if not Author

_____

Institution or Company

_____

Date

The signed statement must be received by the Editorial office before the manuscript can be accepted for publication. Address requests for further information or exceptions to the Editorial Office, c/o Assoc. Prof. Haruyuki OKAMURA, Department of Applied Chemistry, Osaka Prefecture University, 1-1 Gakuen-cho, Naka-ku, Sakai, Osaka 599-8531, Japan. Phone +81-72-254-9291, Fax +81-72-254-9291, e-mail: okamura@chem.osakafu-u.ac.jp

JOURNAL OF PHOTOPOLYMER SCIENCE AND TECHNOLOGY
Volume 36, Number 1, 2023